Strain measurements with GHz and THz radiation

Gilles Diederich

Submitted for the degree of

Doctor of Philosophy

Heriot-Watt University

School of Engineering and Physical Sciences

June 2018

Abstract

With the aim of moving towards quantitative analysis of thermal barrier coating (TBC) lifetime at manufacture, observations of stress-induced birefringence in yttria partially stabilised zirconia (YTZP) as well as air plasma sprayed (APS) yttria stabilised zirconia (YSZ) TBCs are reported with gigahertz (GHz) illumination as well as time-domain spectroscopy (TDS). For the YTZP, values of $1.3\times10^{-1} \pm 2\times10^{-2}$ GPa^{-1} and $1.3\times10^{-1} \pm 1.6\times10^{-2}$ GPa^{-1} were observed with a GHz polariscope in transmission and reflection respectively. TDS yielded values of $9.8\times10^{-2} \pm 4.3\times10^{-2}$ GPa^{-1} and $1.4\times10^{-1} \pm 1.3\times10^{-2}$ GPa^{-1} for the transmission and reflection cases respectively. There is good agreement between the reflection values and the differences in the transmission between the two techniques can be explained by the approach that needed to be taken to the TDS measurements. For the APS coatings, strain-optic coefficients of (-2.4 $\pm$ 0.7) $\times$ $10^{-5}\mu$s^{-1} and (-2.5 $\pm$ 1.0) $\times$ $10^{-5}\mu$s^{-1} for samples with a 1 mm and 2 mm thick mild steel substrates respectively were measured with the GHz system. The TDS measurements lead to 5 times lower coefficients which was explained through plastic deformations and over a year's worth of ageing of the coatings. First measurements of electron beam physical vapour depsoition (EB-PVD) YSZ coatings using TDS lead to the conclusion that the EB-PVD structure was relieving strain throughout the coating and required further understanding of how these coatings reacted to applied stresses to be able to perform measurements which yielded meaningful results.

Finally, a confocal imaging set-up with a GHz source is presented for stress mapping in 2D. The 3rd dimension showed an axial resolution in excess of 30 mm. The lateral resolution was imrpoved to 0.315 $lp\cdot$ mm^{-1}, in other words, elements of 1.58 mm in size could be distinguished. While the imaging capabilities were very reasonable for a 330 GHz input signal, the strain measurements were hampered by unsufficiently controlled samples, though the system was be deemed suitable with either samples with better controlled thicknesses or a higher frequency input signal which would also improve the spatial resolution of the system further.

Acknowledgements

A research thesis is generally not produced in isolation but is a piece of work enabled though input and guidance provided by the people around you. Therefore I would like to acknowledge the support of a number of people that made this thesis possible.

The first person I would like to express my gratitude for is my supervisor, Professor Andrew Moore, as his support and guidance throughout the PhD are what led to the following thesis. I would also like to thank Dr Peter Schemmel for his assistance over the years and the help he provided to get my initial experiments running. Without his work, this thesis would not have been possible. Furthermore, Dr Andrew Waddie deserves my thanks for his constant willingness to discuss results and provide ideas which helped the last sets of experiments to run both smoothly and efficiently.

Further thanks go to the people that have collaborated with me over the course of the PhD, Prof. John Nicholls and Dr Christine Chalk (Cranfield University) for providing us with samples to test, National Physics Laboratory, UK for giving me the opportunity of using their system, and Dr Anselm Deninger and Katja Dutzi (Toptica Photonics, Germany) for enabling the final part of the PhD to go ahead through the loan of their system and their assistance and advice throughout the experiments.

I would also like to acknowledge the people in my office, Ioannis (John) Bitharas, Prveen Bidare, Danny Etieve, Alex Ross and Alex Burton for providing all kinds of help in the form of brainstorming, technical discussions and occasionally much needed distraction from staring at code for hours on end. Additional thanks also go to the workshop staff at Heriot-Watt University, especially Alistair Blyth and Cameron Smith for happily fulfilling all the requests for making and ordering parts and samples.

Finally, I want to thank my parents for the constant support in whatever I decide to do, as well as my wife Samantha for keeping me going with encouragement and moral support throughout all these years.

Contents

Chapter 1

Introduction

Ceramic thermal barrier coatings (TBCs) are routinely used to protect critical components in gas-turbines from extreme environmental conditions such as high temperature and pressure [1, 2, 3]. The continuous drive for increased gas-turbine efficiency and power output is resulting in higher operating temperatures that reduce the lifetime of existing TBCs and require new coating technologies to be developed [1, 2, 3, 4]. Lifetime prediction is a major challenge for TBC manufacturers but there is currently no effective non-destructive evaluation method that can identify and discard coatings with expected shorter lifetime prior to their going into service [3].

A typical TBC system consists of four parts; a super alloy substrate (typically nickel or cobalt based), a bond coat, a thermally grown oxide (TGO) layer and the ceramic top coat. Yttria-stabilized zirconia (YSZ) is the most common ceramic used for the top coat because of its low thermal conductivity and high thermal expansion coefficient. The ceramic top coat is typically deposited either by electron beam physical vapor deposition (EB-PVD) or air plasma spray (APS) [5]. Both methods produce significantly different morphologies, leading to different failure mechanisms [3].

The failure of both EBPVD and APS TBC systems results in spallation of the ceramic top coat, exposure of the unprotected substrate to elevated temperatures and ultimately catastrophic failure of the gas-turbine. Hence, TBCs are considered prime reliant within the gas-turbine, meaning that in addition to enabling increased performance they are critical to safe turbine operation. As a result commercial turbines are only designed to utilize a small percentage of total TBC temperature capacity [2], and in-service TBC lifetimes are severely underestimated in order to maximize the margin of safety.

For APS TBCs, the principal failure mechanism is oxidation of the bond coat at high operating temperatures of the gas turbine, resulting in growth of the TGO layer. This growth causes increased tensile stress along the crests of the undulating bond coat and TGO interface due to the mismatch in the respective thermal expansion coefficients [1, 2, 5, 6]. Ultimately, local cracks and debonds form larger networks and TBC spalling occurs. Understanding TBC failure is ultimately a matter of understanding strains and stresses within the coating system [1, 3, 5, 6, 7].

1.1 Thesis Objectives

Research aiming at the development of quantitative non-destructive testing at the manufacturing stage of thermal barrier coatings is being carried out as part of the Manufacturing with Light funding call from the Engineering and Physical Sciences Research Council in the UK as a collaboration between Heriot-Watt University and Cranfield University. The work presented in this Thesis forms a part of that project. The main objective is therefore the development and application of strain measurement techniques in the terahertz (THz) frequency band. THz radiation was chosen as YSZ has been found to be reasonably transmitting at those long wavelengths [8], allowing for optical non-destructive techniques to be employed provided they are adapted to the device and resolution limitations present in the THz domain.

Since the aim is to perform strain measurements, the potential of photoelasticity within the THz range was chosen as the starting point. A set of linked papers proving the validity of the stress-optic law at THz frequencies [9, 10] for PTFE with the aim of using the material as an optic modulator was published during the project's first year, reinforcing the argument of performing measurements based on photoelasticity, though it hadn't been applied to the ceramics the project was focussed on. The feasibility of applying the stress-optic law to thermal barrier coatings for absolute strain measurements forms the main drive for the presented work, while additionally an option to move from single point strain measurements to 2D images in order to generate full strain maps across an object under test, is explored.

As such, the project as well as this Thesis is divided into a few different individual pieces of work. The first of those is the proof of principle that the stress-optic law ap-

plies to bulk ceramic samples tested in transmission. This is followed by the extension of the feasibility study to YSZ coated onto metal substrates tested in reflection. Both of these pieces of work were led by the research associate on the overarching project, Peter Schemmel, who designed the system set-up and the original analysis approach. This thesis will present refinements to the coating measurements by providing a thorough investigation of the impact of specimen curvature and improving the analysis with a more complete dielectric model for the coated samples. These experiments are followed with the investigation of the viability of using a confocal imaging set-up in the THz domain to produce strain maps.

Finally, the stress-optic law is again applied with a time-domain spectrometer based system to both corroborate and expand upon the measurements performed as part of the first two pieces of work.

1.2 Summary of Chapters

- Chapter 1 consists of an introduction to the thesis, providing the main motivation and objectives of the presented work
- Chapter 2 introduces the working principles of the different systems that were used throughout this work and follows that with a look at what had been done in terms of non-destructive testing of thermal barrier coatings in the THz range, showing the gaps in the literature on the topic.
- Chapter 3 presents the results of stress-optic measurements carried out at 260 – 380 GHz both in transmission and reflection, providing the proof of principle that strain-optic effects can be measured for bulk YSZ samples and APS YSZ coatings.
- Chapter 4 contains the results of the design of a confocal imaging system applied to measuring stresses in PTFE cantilevers.
- Chapter 5 covers the results for strain-optic tests measured with time-domain spectrometry. This includes measurements of the same samples as for Chapter 3 as well as additional measurements on EB-PVD coatings.
- Finally Chapter 6 includes the outcomes of the thesis and presents future steps that should be taken for the project as a result of the presented pieces of work.

Chapter 2

Literature

2.1 GHz radiation generation and detection

2.1.1 Introduction

This section presents the principles for the GHz technologies used as part of this Thesis. The generation of radiation using a Schottky multiplier chain is described, which is followed by a look at pyroelectic detection.

2.1.2 GHz generation with Schottky multiplier chains

Schottky diode based multiplier chains have been used for a long time for Astronomy and space applications, and the development of planar Schottky diodes in the 1980's and 90's was what really made frequencies above 1 THz available [11]. For the ranges up to 400 GHz, conversion efficiencies around 20% are currently possible [12, 13], which makes access to sources with power outputs in the mW readily available. This project made use of a source that was continuously tunable between 260 and 380 GHz with peak power of 1mW at 330 GHz. The generation in this case is based on an RF synthesiser with an output of 9-14 GHz, which is going through 3 successive tripler stages to reach the WR2.8 band of 260 – 380 GHz. The RF input power is at 10 mW, while the output power it at 1 mW, leading to a conversion efficiency of 10%.

Frequency multiplication (in an ideal situation) will increase the phase noise of the signal by $20logN$, where N is the conversion factor, but it doesn't affect either the fractional frequency fluctuations or the deviation in frequency [14]. Figure 2.1 shows the

schematic of a planar Schottky diode. They are widely used due to their simplicity, which allows for a very small active area that leads to very small parasitic capacitances, which are detrimental to performance [15, 16, 17]. A Schottky diode contains matching networks for the input, desired ouput and undesired (idler) frequencies generated within and forms a local oscillator where a number of harmonics of the fundamental frequency are generated. It contains 3 matching networks to allow the optimisiation of the power transfer from the fundamental (input) frequency to the target harmonic. [18] use three main parameters to model the diode performance, the junction capacitance $C_j(v)$, which follows a classical model [19], the non-linear conductance G_j which can be derived from the thermionic emission in Schottky contacts, and finally, the series resistance R_s. R_s needs to be estimated as accurately as possible as it has a negative impact on the frequency multiplication, leading to downward shift in generated frequency. As their model doesn't account for carrier velocity saturation effects, a DC measurement of R_s cannot be used as input in the model as both mechanisms have a very similar impact on the conversion efficiency. The most important parameter of the three is the capacitance C_j, which was determined by the impact of a 15% shift in its value, which causes bandwidth shifts, while the series resistance only affects the efficiency, not the bandwidth.

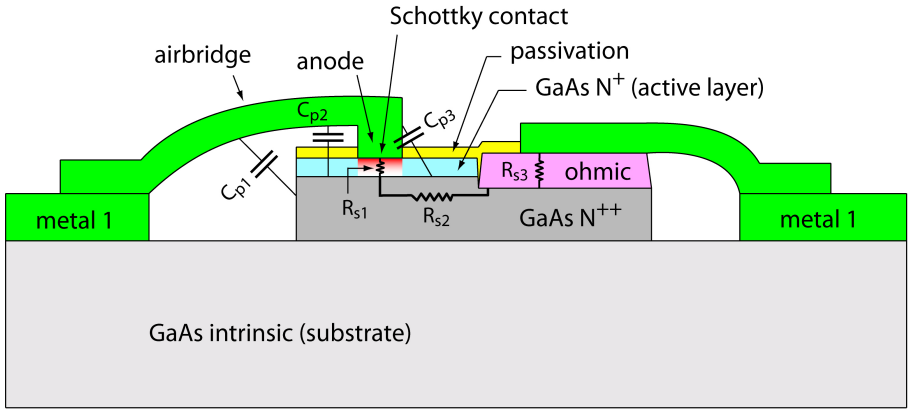

Figure 2.1: Schematic of a planar Schottky diode [18].

2.1.3 Pyroelectric detection

A pyroelectric material will react to a change in temperature with a voltage change [20, 21, 22]. The reason for this is that the material is spontaneously polarised in the dark state, and a change in temperature as light is absorbed leads to a change in the spontaneous polarisation. On one hand, the process is not wavelength dependent, as long as

energy is absorbed, a change in temperature will happen, on the other hand, a change in temperature is required for measurements to be performed. However, while the process itself is not wavelength dependent, the absorption efficiency is wavelength dependent. If a light source with fixed intensity shines onto the detector, it will have a zero output. In order to work with continuous wave sources, an optical chopper has to be used. Figure 8 shows the changes in surface charge and the sensor output as a chopper is opened and closed.

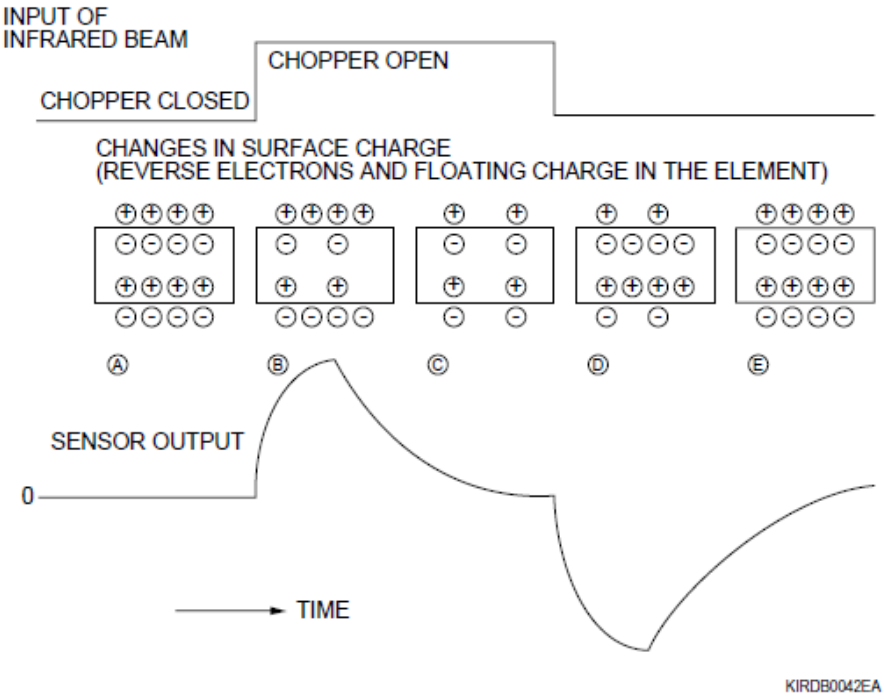

Figure 2.2: Principle of pyroelectric detection [20].

Dependent on the electronics attached to the pyroelectric surface, the surface charge is either extracted as voltage or as current. The commonly used scheme is voltage type detection, as it consists of a simpler circuit and tends to show less noise, while its sensitivity peaks for low chopping frequencies. The current type on the other hand has higher gain and its sensitivity is constant across a wide range of chopping frequencies and is limited by the constant of the amplifier. Thus the frequency limit is flexible up to a point and can be changed by altering the amplifier circuit configuration.

The response of the detector can be divided into 2 clear sections, first is the rise of the voltage until it reaches its maximal value. This value is proportional to the amount of energy within the pulse, and the time it takes to reach the maximum depends on the detector rise time. The second section is an exponential decay of the signal after the

maximum is reached. This part of the detector response is independent of any incoming signal and is defined by the electrical time constant of the detector circuit. Any radiation that hits the detector after its rise time is not affecting the measurement anymore (unless there is a change in intensity again, at which point a new measurement will start).

While the sensitivities of pyroelectric detectors still cannot rival that of microbolometers, they have reached the point where they are similar to that of a Golay cell [21]. However, in contrast to microbolometers, which need to be operated at liquid nitrogen temperatures, both Golay cells and pyroelectric detectors operate at room temperature. One big difference between a Golay cell, which is an acoustic sensor that detects vibrations of a membrane, and a pyroelectric detector is that the pyroelectric one has a linear intensity response until it reaches its noise floor [23].

The rise of new material processing methods has allowed thin lithium tantalate films to be formed, which is a pyroelectric material which shows improvements in sensitivity as the layer is thinned down. Thicknesses of less than 10 μm have been reported by Stenger et al. [24], which show an improvement of over an order of magnitude compared to the state of the art in lithium tantalate detectors at the time.

1D and 2D array detectors with pyroelectric pixels have recently been proposed to increase THz imaging speeds, as commonly single pixel detectors are used, requiring either the optics or the sample to be scanned. Li et al. have recently reported a 30 pixel line array based on lithium tantalite as the pyroelectric material with pixel sizes of 1 mm x 0.4 mm [25]. Spiricon has 2 models of a pyroelectric cameras based on lithium tantalate available, where one has twice as many pixels as the other [26]. The detectors have a sensitivity band within the infrared region and a second band throughout the terahertz frequencies.

2.2 Time Domain Spectroscopy (TDS)

2.2.1 Introduction

THz TDS is a spectroscopic technique which is based on the coherent detection of the electric field of THz pulses through either electro-optical or photoconductive means. Its

development started with the rise of femtosecond lasers in the 1980s [27, 28, 29]. The following sections will give an outline of a typical THz TDS system and explain the generation and detection of the THz radiation as well as the required data analysis to extract material properties from the measured data.

2.2.2 System setup

Figure 2.3 shows the TDS system that is used at the National Physics Laboratory (NPL), which corresponds to a typical setup.

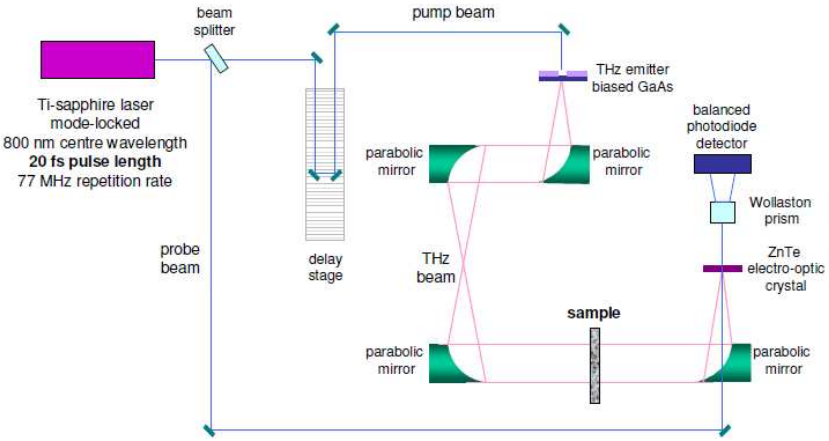

Figure 2.3: TDS setup at the UK National Physics Laboratory [23].

A femtosecond laser is used as source (a Ti:sapphire laser in the system in Figure 2.3) and its output is split into a pump beam, which generates the THz radiation, and a probe beam, which is used to gate the detector. Generation and detection are typically done either using photoconductive antennas or optical rectification within a zinc telluride (ZnTe) crystal. One of the beams is going through a delay stage, which introduces a time offset between the probe and pump beams that is used to resolve the THz pulse in time at the detection stage. Most commercial systems use fiber coupled generation and detection both in order to compact the stystems and to reduce the chances of misalignment due to temperature variations around the system.

2.2.3 THz pulse generation and detection

This section gives an overview of THz generation using photoconductive antennas followed by a quick look at electro-optic generation.

THz generation based on photoconductive antennas has been applied since the first demonstrations of THs TDS back in 1985 [27]. The antennas are generally made from a GaAs semiconductor structure [30, 31]. Excitation of the GaAs by the femtosecond pulses leads to the generation of electrons and holes in the conduction and valence bands respectively, if the incoming photon energy exceeds the GaAs bandgap energy of 1.43 eV at room temperature. By applying a bias across the GaAs, the generated carriers are accelerated, leading to a pulsed photocurrent as the carriers will decay after a time defined by to the free carrier lifetime. This rapid change in current leads to radiation of an electromagnetic signal which, provided the incident laser pulses are sufficiently short, will be covering frequencies up to 5 THz in most systems. The generation is described in space and time by the following equation for an elementary Hertzian dipole antenna [32]:

$$E_{THz}(r,t) = \frac{l_e}{4\pi\varepsilon c^2 r}\frac{\partial i(t)}{\partial t} sin(\theta) \tag{2.1}$$

where r is the distance from the antenna (and is much larger than the wavelength), t is time, l_e is the effective length of the dipole, ε is the dielectric constant of the radiation medium, c is the speed of light, $i(t)$ is the photocurrent induced in the antenna by the laser pulses and θ is the angle from the dipole axis. Equation 2.1 shows that the resulting radiation intensity depends on the effective antenna length l_e and the rate of change of the photocurrent $\frac{\partial i(t)}{\partial t}$ [32, 33, 34].

The effects of changing the pump pulse length, central wavelength of the pulses, dipole length and the bias across the antenna on the generated pulse have been presented by Chang et al. [33]. They show that a shorter central wavelength will increase the generated THz pulses power, while a longer excitation pulse duration has the same effect. However, increasing the pulse duration also decreases the bandwidth of the THz pulse, reducing the amount of high frequency content. Thus for the largest frequency content in the THz signal, a short optical pulse duration is preferable. The increase in power can be seen from Eq. (1), as a shorter wavelength means a higher photon energy. As electron-

hole pairs that are generated by the absorbed photons will receive all the energy of the photons, any energy left over after the band gap has been surpassed will be transferred as kinetic energy, thus increasing the rate of change in the current. If the pulse length is increased, more electron-hole pairs will be generated, leading to larger currents, where each electron still has the same decay rate, which again yields a larger rate of change for the current. Similarly, higher bias voltages increase the power in the THz pulse as the electron acceleration is increased. Finally, increasing the effective antenna length also leads to an increased power in the THz signal. The bandwidth effects of changing the pulse wavelength, the bias across the antenna and the effective antenna length are not discussed in the paper, and all of the results assume that the effect of space-charge screening can be neglected.

Tani et al. [32] compared the performance of antennas based on low-temperature-grown GaAs (LT-GaAs) and semi-insulating GaAs (SI-GaAs), finding no significant differences between the two and concluding that the radiations is mainly generated at the photocurrent rise, while its decay only make a small contribution. They do still conclude that LT-GaAs does have better saturation properties and higher breakdown fields than SI-GaAs, while SI-GaAs shows radiation powers which are similar or larger than those of LT-GaAs antennas. Different antenna structures on the other hand have drastic effects on the THz pulse width, power and spectral content [28, 29, 32, 35, 36, 37], with bow-tie antennas found to have very strong radiation powers but a very limited frequency content with the spectral peak near 0.1 THz and the cut-off typically around 1-1.5 THz. A biased strip-line antenna on the other hand showed very short pulse durations ($\sim$350 fs), which might be limited by the detector's response, and comparatively large frequency spectra with the cut-off at 4 THz. For strip-line antennas, it has also been reported that the pump laser spot size shouldn't be limited to a small region within the gap, but that the most efficient generation can be obtained by having the laser beam just about overlapping the whole gap [38].

Some work has been carried out to design photoconductive antenna arrays [39], and while they showed promise, with the reported design, 77% of the THz radiation was absorbed by the ceramic substrate, leading to very low recorded radiation powers. The conclusion that if the substrate is drilled through, the array would generate 10 times the power of a traditional strip-line antenna was questionable though, as compared the output

of the array to a strip-line if the same electric field was applied across them by the pump beam, however, with a 100 μm strip line, a spot of 100μm is required for efficient illumination, while they illuminate the whole array with the same laser spot, which means they need a spot close to 1.5 mm which provides the same electric field across each antenna as the 100 μm spot for the strip-line. A better approach to one big spot would be using adaptive optics to split the beam into 8 smaller ones.

Recently, TDS has started becoming commercially available due to the development of photoconductive antennas operating with 1.5 μm excitation wavelengths [40, 41, 42, 43, 44, 45]. This meant that instead of Ti:sapphire based systems which take up most of an optical bench at the least, systems designed around components developed for the communications industry could be designed. This alongside the ready availability of Er-doped femtosecond fibre lasers at 1550 nm allowed systems to be compacted with the optical side almost fully fibre-coupled. The photoconductive antennas for these systems shifted to InGaAs based antennas with thye inclusion of dopants such as ErAs Fe and Be to optimise the carrier dynamics within the semi-conductor.

Electro-optic generation uses non-linear effects within crystals, specifically optical rectification, to generate ultrashort THz pulses. The basis of the THz generation is difference-frequency generation within the ultrafast optical pulse facilitated by dispersion within the crystal over the pulse bandwidth. As some frequencies travel faster than others, phase-matching conditions between the constituent frequencies are fulfilled throughout the crystal, generating an output signal based on the difference between the matched frequencies [46]. Commonly used crystals for this application are $LiNiO_3$, ZnTe and GaP, as their non-linear properties allow for THz generation through optical rectification. However in the scope of this review, optical rectification for generation was not investigated in too much depth, as while it was used in one instance, most of the work in TDS was carried out with systems using photoconductive generation.

2.2.4 THz pulse detection

While THz pulses can be detected using bolometric or pyroelectric detection, this approach only yields the average power and loses all the benefits of a TDS system. Rather than average power, in TDS the electric field of the THz pulse is measured directly most

commonly through electro-optic sampling for research systems, while commercial systems are more likely to use photoconductive antennas, as they tend to be more compact.

In the case of photoconductive detection [34], the probe beam is used to gate the antenna, as incoming fs pulses on the semiconductor material will generate electron-hole pairs provided the photon energy is larger than the band gap. Thus electrons that can move across the antenna are generated whenever an optical pulse hits the antenna. These electrons are accelerated across the antenna gap by the electric field of the THz pulse at the point in time where the optical pulse arrives. Thus a photocurrent across the antenna that depends on the electric field of the THz pulse at the moment where the probe pulse arrives can be measured. By introducing a relative delay between the THz beam and the probe beam, the THz pulse's electric field is scanned in time, giving a time-domain trace of the THz pulse.

In electro-optic sampling [47],the phase modulation of the probe pulse by the THz pulse as they both propagate through the crystal is measured. The phase modulation is induced by a refractive index change caused by the incoming THz pulse's electric field. This change in refractive index rotates the polarisation of the probe pulse and is cause by a Kerr-like effect. Since the optical probe pulse is very short compared to the THz signal, the resulting polarisation change in the optical pulse measured for one position of the delay line gives a snapshot of the THz electric field at that particular instant in time. Scanning the delay line allows for the THz pulses' electric field to be measured in the time domain. The phase modulation is measured by monitoring the difference between the s and p components of the optical pulse's polarisation after it travelled through the detector crystal. This is achieved by using a correctly oriented Wollaston prism to split the two components and detecting them with a pair of balanced photodiodes. The difference between the two polarisation components is proportional to the electric field of the THz pulse at the moment where the optical pulse overlaps with it. Thus the time-domain profile of the electric field is scanned in exactly the same way as for photoconductive detection using an optical delay on one of the two beam paths.

2.2.5 TDS data analysis

In order to extract material properties out of a THz TDS measurement, the measurement with the sample under test needs to be compared to a reference measurement without the tested sample in the beam path. The starting position on the delay line for the reference measurements defines the zero position on the time axis. Before moving into the frequency domain by taking the Fourier Transform of the signal, it is advisable to take a set of identical measurements and average them out in the time domain, as it allows for better noise reduction [31, 48].

Following is an approach at data analysis as found in [31, 49]. If the sample is a dielectric with parallel surfaces and the THz radiation is at normal incidence to the surfaces, the THz signal passing through the material can be expressed as

$$E_{sam}(\omega) = \eta \frac{4\tilde{n}_s(\omega)}{[\tilde{n}_s(\omega)+1]^2} \cdot e^{-i\tilde{n}_s(\omega)\frac{\omega d}{c}} \cdot E_0(\omega) \tag{2.2}$$

where η is the transmission factor of free space, $\tilde{n}_s(\omega) = n_s(\omega) - i\kappa_s(\omega)$ is the complex refractive index with $n_s(\omega)$ being the refractive index and $\kappa_s(\omega)$ the extinction coefficient, d is the thickness of the sample and $E_0(\omega)$ is the incident wave. The reference spectrum can be expressed as

$$E_{ref}(\omega) = \eta \cdot e^{-i\frac{\omega d}{c}} \cdot E_0(\omega) \tag{2.3}$$

Both Equations 2.2 and 2.3 assume that there are no reflections. In order to obtain those two spectra from the measured data, the Fourier transform of the time domain signals with and without the sample respectively are taken. The complex transfer function of the sample in the frequency domain can be expressed as

$$\frac{E_{sam}(\omega)}{E_{ref}(\omega)} = H_0(\omega) = \frac{4\tilde{n}_s(\omega)}{[\tilde{n}_s(\omega)+1]^2} \cdot e^{-i\kappa_s(\omega)\frac{\omega d}{c}} \cdot e^{-i[n_s(\omega)-1]\frac{\omega d}{c}} \tag{2.4}$$

Assuming that the extinction coefficient is negligible compared to the refractive index, $\tilde{n}_s(\omega)$ is often approximated to $n_s(\omega)$, giving a simplified transfer function,

$$H(\omega) = \frac{4n_s(\omega)}{[n_s(\omega)+1]^2} \cdot e^{-i\kappa_s(\omega)\frac{\omega d}{c}} \cdot e^{-i[n_s(\omega)-1]\frac{\omega d}{c}} \tag{2.5}$$

By taking the argument and the logarithm of $H(\omega)$, a solution for $n_s(\omega)$ and $\kappa_s(\omega)$ respectively can be deduced as

$$n_s(\omega) = 1 - \frac{c}{\omega d} arg[H(\omega)] \tag{2.6}$$

and

$$\kappa_s(\omega) = \frac{c}{\omega d}\{ln\frac{4n_s(\omega)}{[n_s(\omega)+1]^2} - ln|H(\omega)|\} \tag{2.7}$$

Finally, the absorption coefficient is related to the extinction coefficient as follows

$$\alpha_s(\omega) = 2\frac{\omega\eta_s(\omega)}{c} \tag{2.8}$$

Equations 2.6 - 2.8 allow the refractive index and absorption coefficient of a sample under test to be calculated from the measured time domain signal for a known sample thickness. In practice, Equation 2.6 has an additional term at the end to cater for any offset with respect to the reference measurement that is applied to the starting point of the delay stage, and is written as

$$n_s(\omega) = 1 - \frac{c}{\omega d} arg[H(\omega)] + \frac{2x}{d} \tag{2.9}$$

where x is any offset applied to the delay line between the sample and the reference measurement. It should be noted that the phase calculated from $arg[H(\omega)]$ will need unwrapped as the *arg* function will yield phase values between $-\pi$ and π as shown in Figure 3. The top plot shows the phase of a reference signal measured at the NPL before its phase has been unwrapped, while the bottom plot shows it after unwrapping.

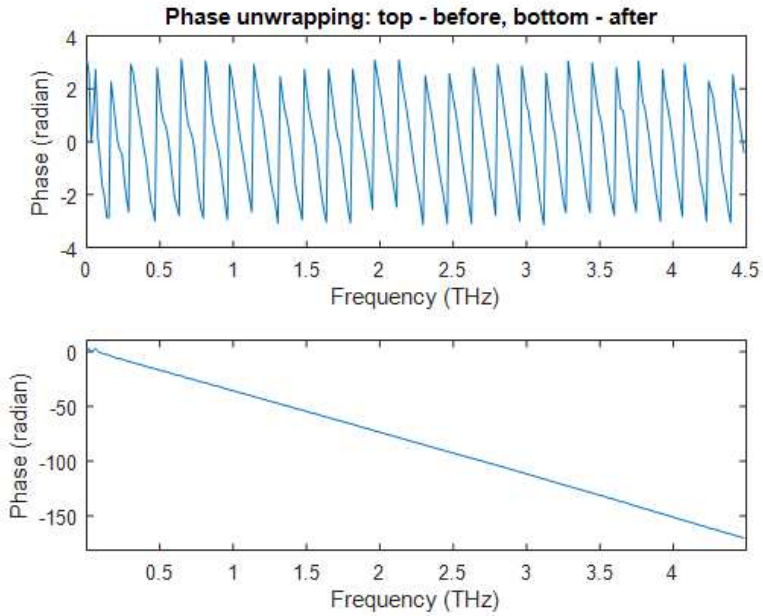

Figure 2.4: Example of phase unwrapping: (top) signal before unwrapping, (bottom) after unwrapping.

Unwrapping should not be started at DC, but rather a little further in the data, as the first $\sim$100 GHz tend to be mostly noise, as the detection is not sensitive at such low frequencies. In order to avoid artefacts cause by that section of noise, it can be skipped in the unwrapping and extrapolated. Figure 2.5 gives an example of the effect of phase extrapolation on the refractive index calculation for PMMA [31].

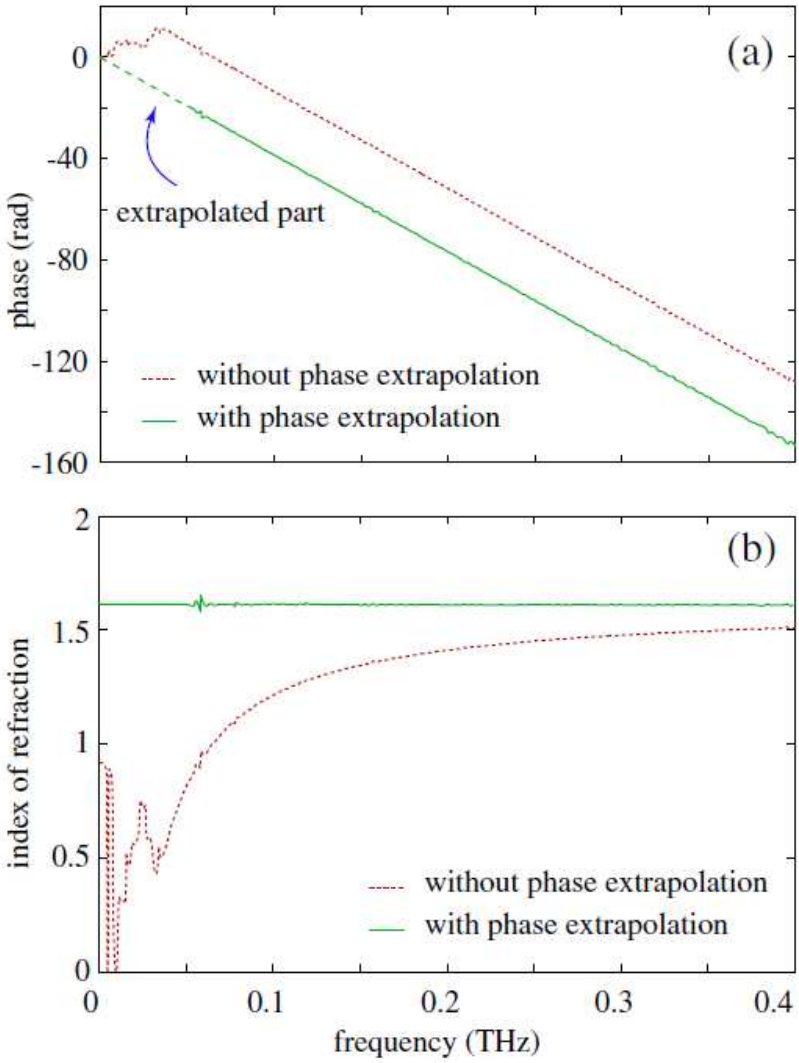

Figure 2.5: (top) Phase unwrapping with and without extrapolation, (bottom) refractive index of PMMA, which is reported to be around 1.6 [31]

In addition, with the complex refractive index, the complex dielectric constant of the tested material can be calculated, as $\tilde{\varepsilon}_s = \tilde{n}_s^2 = (n_s + i\kappa_s)^2$ [8].

The above Equations 2.6 - 2.8 assume that the thickness is known. Algorithms based on a total variance calculation have been proposed to fit for both the complex refractive index and the thickness, minimising the variation between points across the frequency domain, an approach which works for samples lacking sharp features in the chosen frequency range, at which point with a typical sampling frequency of $\sim$17 GHz, the variation between adjacent points is expected to be small [50, 51]. However, as they tend to fit over a range of thicknesses and look for the thickness where the total variation is a minimum, they tend to be computationally intensive approaches, especially for the exper-

iments presented in this Thesis, where the absolute thickness is less crucial as the change in refractive index is of higher interest than the absolute value.

It is important to take a look at the errors affecting THz-TDS measurements, especially after a comparison of the performance of several commercial and research systems around the globe has highlighted that there were rather drastic differences between systems in terms of performance and results [52]. Figure 2.6 schematically shows the different sources of noise one can expect on a TDS measurement [53]. Some, like the Fabry-Perot reflections and the approximations in the transfer function are partially linked. As mentioned above for the derivation of Equations 2.6 - 2.8, it is often assumed that there are no Fabry-Perot reflections, which simplifies the solution for the transfer function a lot. In the paper from which Figure 2.6 was taken from, a majority of common error sources was identified with ways to asses their impact on the final optical constants presented.

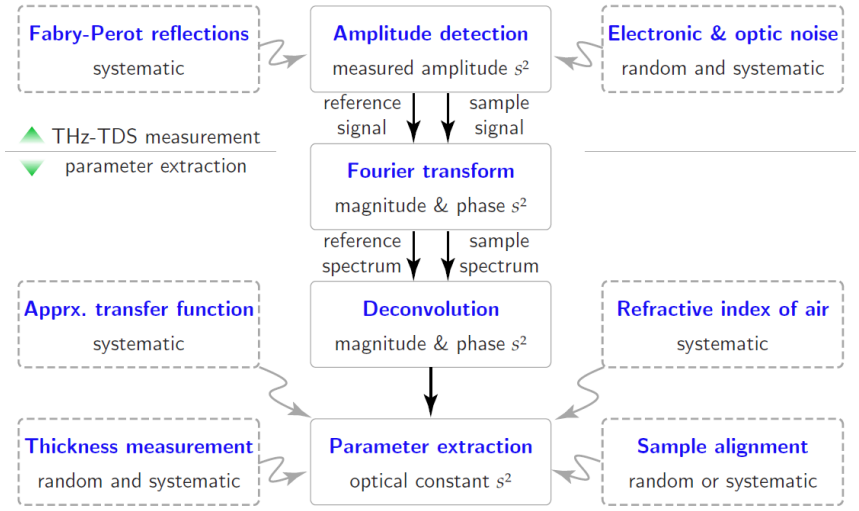

Figure 2.6: Sources of error in THz-TDS measurements. [53]

After having given an introduction into the working of the two types of system used throughout this Thesis, the next Section in the review will focus on non-destructive testing applied to thermal barrier coatings published to date, as that is the end goal of the overarching project.

2.3 NDE on TBCs in GHz/THz

Several non-destructing testing methods have been used to inspect TBC properties. These include, acoustic emission [54, 55, 56], impedance and Raman spectroscopy [57], as well as thermography [58], photoluminescence [59, 60], infrared imaging [5, 60] and x-ray diffraction [61, 62]. Some of these methods are used to determine material properties of the TBC [63], while others study the effect of thermal-gradients on thermal-fatigue [58, 59] or overall coating wear [64]. X-ray diffraction has been used to measure residual and thermal stresses in TBCs, however this technique is limited to measurements over small areas near the top coat surface due to poor x-ray penetration [62].

The unique advantage of THz radiation for NDE of TBCs is that the ceramic has a transmission window at frequencies below 2 THz. This allows for the potential application of optical NDE techniques on the coatings.

This review will therefore focus on the application of THz radiation based testing methods. An important starting point into the topic is a publication by Watanabe et al. [8] which investigates the dielectric properties of plasma-sprayed thermal barrier coatings. After depositing the coatings, they mechanically separate them from the substrate in order to carry out transmission THz TDS measurements on the free standing YSZ samples. They find that the real part of the dielectric constant is highly dependent on the porosity of the material and can be modelled with both the Maxwell-Garnett effective-mixing theory and Giordanos theory (an extended form of the Bruggerman theory), which considers a random distribution of ellipsoidal pores in the coating. Refractive index values they measured range from 4 to 5.2, increasing with decreasing porosity, while a sintered sample of YTZP was found to have an index of 5.7, which is a sample with close to no porosity. The imaginary part of the dielectric constant on the other hand has been found to be mostly independent of the porosity of the material, which means that its absorption properties of all their tested YSZ samples are highly similar, with highest transmission at frequencies below 500 GHz, while the cut-off frequency in their measurements is around 1.5 THz for all samples. While the absorption of a material is dependent on its porosity, which affects how light is scattered throughout it, in the case of YSZ, the change through scattering in the absorption linked to porosity is very small compared to the absolute value of the absorption that its contribution is generally negligible.

Some work has been carried out on thickness measurements for thermal barrier coating [65, 66]. In both cases, they used a set of test samples to measure a refractive index value. This value was then used on a second set of samples to calculate the thicknesses from time of flight calculations, to show that the method gave results which matched with those from microscope measurements. In [65] the same approach was then applied to a coated turbine blade and the calculated thickness matched reasonably well with that from a microscope measurement of the cross section of the tested blade. [66] on the other hand gives a qualitative assessment of some changes between an turbine blade that has been removed from service and a fresh one. Neither paper mentions the fabrication mechanism of their coatings and samples, though from the mention of a columnar structure in the introduction of [66] it could be assumed that their coatings are EB-PVD coatings. However, as production specifics and porosity have a large impact on the refractive index values of coatings, the validity of a standard refractive index value (of 4.8 for one paper and 3.73 for the other) is questionable for widespread use in TBC testing.

Chen et al. [67] present a solution based on measuring the time difference between the Fresnel reflection off the air/coating boundary and the reflection off the coating/metal interface to monitor the health of a coating. Figure 2.7 visualises the approach.

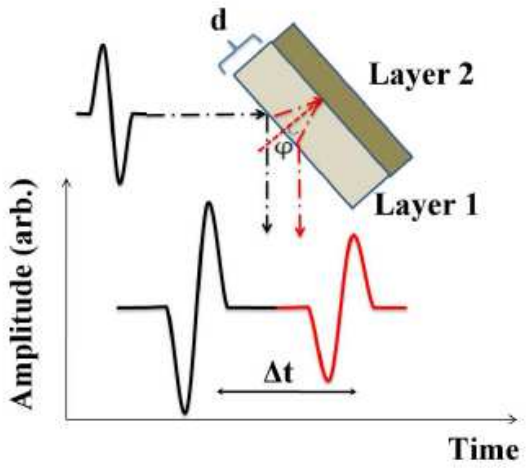

Figure 2.7: THz TDS reflectometry [67].

The sample is subjected to thermal cycling by placing it into a furnace at 1100C for a total of 1350 hours, while it is periodically removed to have measurements performed on it. Scanning electron microscopy is used to look at the coating condition by cutting a small slice off the edge of the sample at every stage. This shows the evolution of the TBC

throughout its lifetime until it starts delaminating after 1350 hours in the furnace.

As time progresses, first a thermally grown oxide layer will form at the coating boundary as oxygen penetrates the coating during expansion and contraction. This oxide layer induces internal stresses which are further increased by thermal mismatches between the substrate and the coating and will lead to the formation of voids, which eventually lead to delamination of the coating. This progressive failure can be seen in Figure 2.8. The voids in Figures 2.8e and 2.8f are larger than should be expected in a regular sample, as the preparation of the cross section for the microscope image to be taken off weakens the interfaces in multi-layered species.

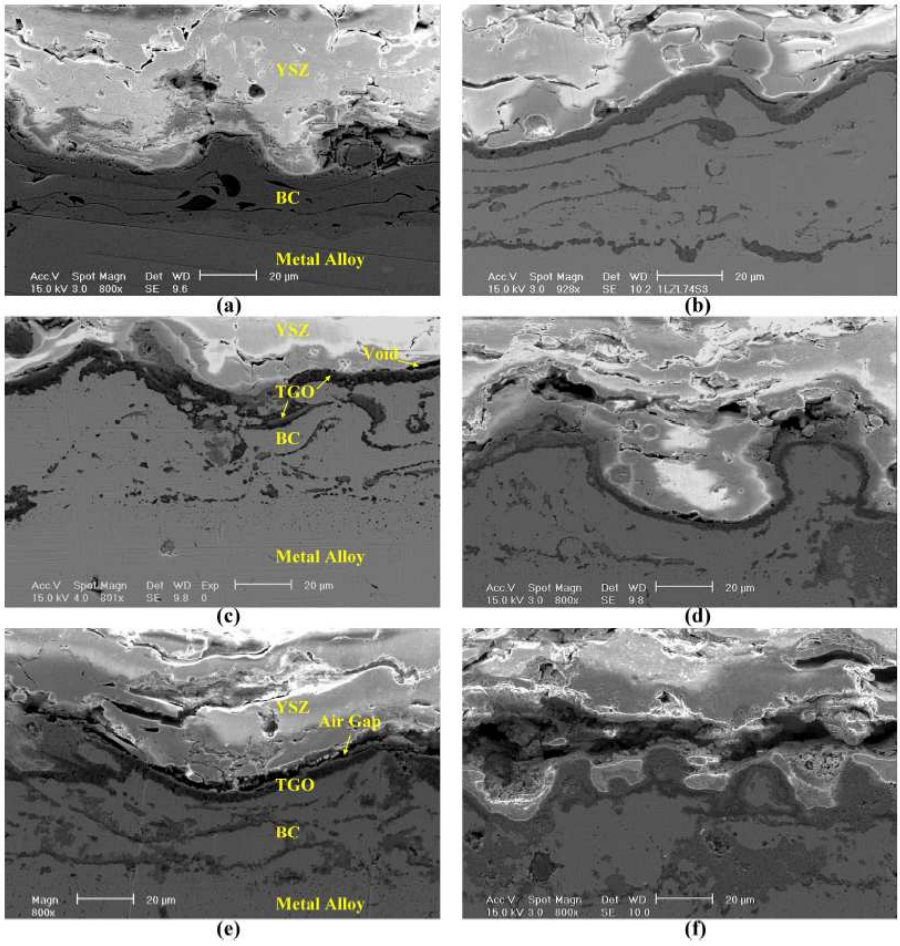

Figure 2.8: Evolution of a TBC through simulated thermal cycling. (a) before thermal cycling, (b) after 100 hours, where the oxide layer (TGO) had formed as the dark grey area at the coating boundary,(c) after 348 hours, showing the first void formations, (d) after 790 hours, (e) after 1000 hours, where the voids start growing larger, forming air gaps at the coating boundary, and (f) after 1350 hours, where delamination takes place (just outside of the image) [67].

One of the main issues of the methods becomes apparent at this point, as they simulate the effect of the different states of the interface on the reflected pulse. As the intermediate layers (oxide layer and voids) are of the order of a few micron in thickness, reflections off them will have a delay of the order of less than a picosecond, while the incident pulse has a width of 3 ps. Thus reflections off the intermediate layers will be indistinguishable from the reflection of the metal substrate. Also, the method relies on comparing the variation to a previous measurement, which would require a lot of data to be kept and cross-referenced for each coated element. Additionally, the element under test will have to be scanned to be tested in entirety, which would lead to a lot of time lost in a lab for testing, something undesirable for commercial products like turbine blades. Furthermore, measures have to be taken that the element positioning in the system is the same for each time it is tested in order for the recorded data to match up with the new measurements. And finally, while testing on aged specimens during the research phase of the work is unavoidable, the best solution for the aeronautics industry would be one where blades are tested at the manufacturing stage and any that will fail early on in their lifetime could be identified and discared before being put into service..

Their experimental values coincide well with the simulations, except that there is slightly larger delay between the reflection off the air/YSZ boundary and the reflection of the metal substrate due to the simulations not considering scattering within coating and the roughness of the interfaces for ease of implementation. However, the changes in pulse shape and the overall trends are clearly followed by the experimental results. Figure 2.9 shows the simulation results for the reflection off the bond coat and visualises the main change in pulse shape that they look at, namely the dampening of the local minimum around 15 ps. This dampening is understood to be caused by increasing air gaps causing enough delay between the reflection of the YSZ/air gap interface and the air gap/oxide layer interface to be separated and affect a different position of the pulse reflected off the metal.

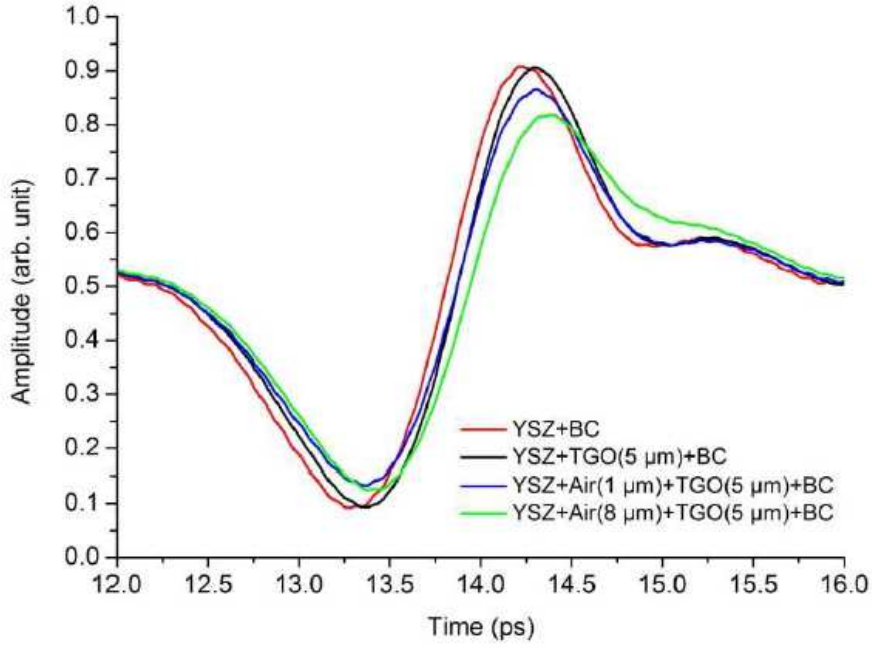

Figure 2.9: Simulation of the reflection of the metal substrate (BC) [67].

They manage to detect defects of a few micron in size with their approach, however as testing routine, the method is bulky due to TDS measurements being rather slow (often of the order of minutes per measurement) and it requires a lot of data to be stored in order to see the change over time. A single measurement cannot identify if there is a defect present or not, unless at least a reference measurement before thermal cycling of the material under test is present, while likely more than just that reference is required, as it would not be clear which stage of its evolution the coating is in.

Something which has been noticed as missing in the literature is strain measurements across the YSZ topcoat in a thermal barrier coating. While strains on the surface of the coating can be measured, the lack of transmission at optical frequencies means that subsurface measurements are severely limited. As doing just this is an important aim of the project that this Thesis is linked to, and as the proposed approach requires the strain-optic responses of the coatings to be investigated, 2 papers by Li et al. [9] and Song et al. [10] need to be briefly discussed as part of this review.

In those papers, the stress-optic law [68] is verified with PTFE in the THz frequency range with a TDS system. The stress-optic law can be expressed as:

$$\Delta n = C\sigma \tag{2.10}$$

where Δn is the change in refractive index, C is the stress-optic coefficient and σ is the applied stress. While they proved the validity of the stress-optic law with and without accounting for the change in thickness with applied load, there was some doubt in terms of the actual value. This is linked to the fact that strain gauges were glued to the PTFE samples, something which the nature of PTFE makes extremely unreliable, as the gauges are likely to slip at loads are applied. Additionally, PTFE is viscoelastic, at which point, in order to keep a constant applied stress, the strain needs to be adapted as the material changes structure to relieve applied stresses. Neither of those effects were accounted for. Finally, the intended application for their results was optical modulation by changing the refractive index of a PTFE modulator with an applied stress, whereas we intend to use the principle for direct stress and strain measurements on YSZ based coatings.

2.4 Conclusions

The concepts of Schottky based frequency multiplication to generate radiation of a few hundred GHz up to $\sim$2 THz have been presented along with the principles of pyroelectric detection, which is used to generate and detect radiation between 260 and 380 GHz throughout this project. There was little emphasis on these technologies beyond their operating principles as the focus of the work carried out is not on designing and optimising them, but rather merely using them as off-the-shelf components in the optical systems presented later on.

The workings of time-domain spectroscopy have been explained, including the different generation and detection methods as well as the principles of the data analysis that surrounds the technique. Additionally, the technique currently represents the standard way of doing measurements in the THz frequency range, though it is not currently very standardised [52]. This was obvious when looking at non-destructive testing applied to yttria sabilised zirconia (YSZ) thermal barrier coatings in the THz region, as all of the sparse amounts work up to date has been performed with TDS. Thickness measurements on coated samples have been carried out albeit only applied to fairly well controlled samples, as the approach was to determine a ”standard” refractive index for the coating and use that for all other measurements, while it has been shown [8] that porosity has a very large impact on the refractive index of a YSZ coating. Some qualitative measurements

on coatings as they were artificially aged in a furnace were also performed, but as there was no clear link between the changes and physical properties of the coating, qualitative analysis was still missing.

On the other hand, the validity if the stress-optic law [68] in the THZ region at least for PTFE was recently proven which paved the way for the majority of the work presented in this Thesis. In order to overcome the lack of quantitative non-destructive testing methods for thermal barrier coatings, the validity of the stress-optic law for YSZ as a bulk sample and as coating on metallic substrates will be investigated in order to assess the feasibility of quantitative analysis of thermal barrier coatings in the THz range. These experiments and their corresponding results will be presented alongside some work on extending the measurement technique into two dimensional imaging.

Chapter 3

GHz Strain Measurements

3.1 Introduction

Throughout this Chapter, measurements of strain optic coefficients for ceramics are presented and discussed. First of all, the properties of both our source, a Virginia Diodes synthesizer and amplifier/multiplier chain generating a vertically polarised continuous-wave signal tunable between 260 and 380 GHz, an our 2 detectors, both pyroelectric detectors manufactured by Genetec-eo, were investigated in order to assess the best way to perform the measurements. This investigation is followed by the presentation of stress-optic measurements on polytetrafluoroethylene (PTFE) and yttria-partially stabilised zirconia (YTZP) in transmission [69]. Finally, the approach was applied in reflection to the YTZP samples as well as yttria stabilised zircona coatings on mild steel substrates [70]. The results of those experiments are followed by a closer look at the potential impact of curvature on the strain optic coefficients, as well as improvements to the data analysis fuelled by an improved understanding of the coatings since the reflection data's publication.

3.2 Experimental System Characterisation

3.2.1 Introduction

In this section, the properties of 2 source-detector pairs are presented. In both cases the source was a VDI AMC with a WD2.8 horn mounted. In section 3.2.2, results with a THz-I-BNC pyroelectric detector manufactured by Genetec-eo are presented, while in section 3.2.3, results with a THz-9D in combination with an M-Link, both by Genetec-eo,

are shown. The THz-I-BNC was analysed as saturation effects were commonly observed, and was then applied to the THz-9D to assess its performance and ensure it was suitable for the task at hand.

The analysis was driven by in house MATLAB®code. In order to be able to work with the detector signal, each pulse was extracted out of the pulse train so that it could be manipulated separately. For this, first the start and end positions of the pulses throughout the train needed to be determined. This was achieved through looking at the slope of the signal, as each time a new pulse starts, there will be a sharp peak in the slope. The slope is illustrated by the green line in 3.1. By cutting the signal at each of those slope maxima, the pulse train was divided into its separate pulses. Additionally, since anything which happens after the maximum of the pulse is independent of the incoming THz signal, the pulses were reduced to the data between the pulse start and the pulse maximum for most analysis purposes. The exception to this was the pulse shape analysis, where the entire pulse, including the decaying part, was used.

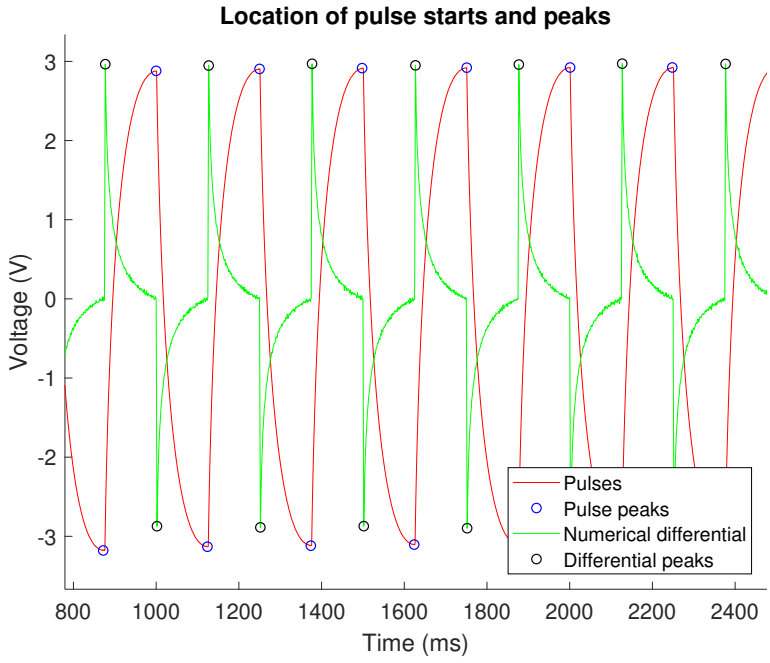

Figure 3.1: Identification of the pulse starting points and peaks.

In order to be able to work with and compare the separated pulses, the negative pulses got multiplied by -1 after which each pulse in the train had an offset applied to ensure their starting point was always at zero.

Two different methods for measuring the pulses have been looked at. The first method, the peak value approach, was a measurement of the voltage difference between the pulse maximum and the pulse start, and measured the pulse power. The second approach was to calculate the area underneath the pulse (from pulse start to pulse maximum), which could lead to better noise performance due to additional averaging, while also requiring slightly more processing overall. Integrating the area under the pulse is a measure of pulse energy.

3.2.2 THz-I-BNC

Introduction

As a pyroelectric detector, the THz-I-BNC, shown in Figure 3.2, needed to be operated with a pulsed source. Our cw source could be operated in pulsed mode by attenuating the driving RF signal using an attenuation voltage without the need for an external chopper. The first characteristic of the system that will be presented at is the stability of the pulse shape (with respect to both time and amplitude). This is followed by a look at the detector rise time and the time it takes for a pulse train to stabilise around the detector's DC level. Finally, the 2 different ways to measure the pulse power are compared by looking at the linearity with amplitude of the calculated powers as well as their fractional noise figures.

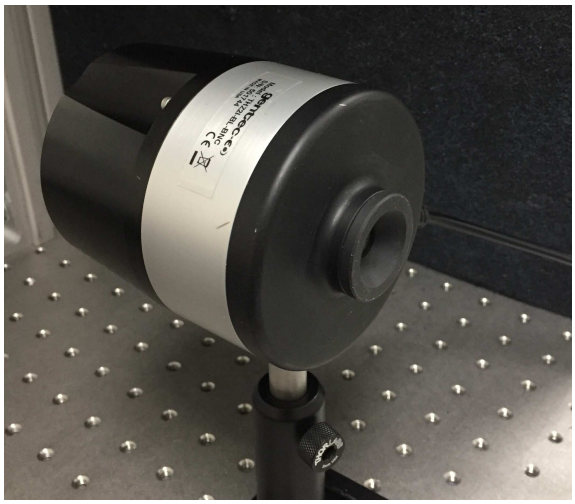

Figure 3.2: Photograph of the THz-I-BNC.

Pulse train stabilisation

While recording pulse trains to analyse and when first looking at them, it became obvious that a stabilisation of the signal around the DC level of the detector was taking place, which can be seen on Figure 3.3 and is better illustrated with Figure 3.4. This effect will influence the pulse shape while it is taking place and might have adverse effects on other parameters of the pulse train that could cascade into the final power measurements.

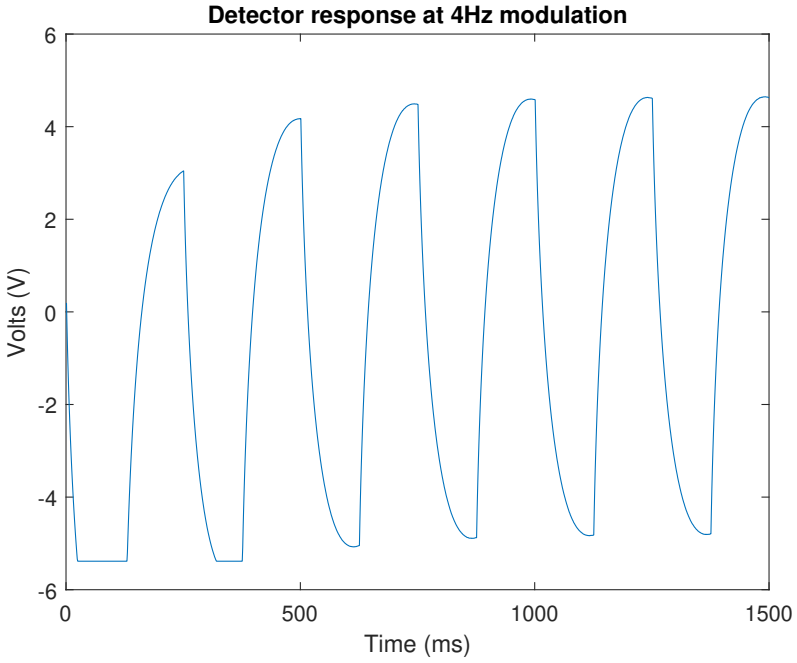

Figure 3.3: Typical signal for the THz-I-BNC at 4 Hz signal modulation frequency.

The pulse train shown in Figure 3.3 illustrates the shift of the pulses that took place over roughly the first second of the measurement. As the source produced a series of square pulses, the pyroelectric detector would show 2 responses per pulse, one at the rising edge and a second one at the falling edge. The very first edge that it detected would start from a DC level of $\sim$0 V and had a measurement range of 5 V available. As the pulses were typically kept to a length similar to that of the detector's rise time, the starting voltage level for any subsequent pulses was going to be close to the maximum (or minimum in case of a falling edge) value reached for the previous pulse, which almost doubled the available voltage range for the measurement. Also, as seen on Figure 3.3, it was quite common for the first few pulses to saturate the detector when working at the source's full power (nominally $\sim$1 mW at 330 GHz). Figure 3.4 illustrates the change in starting voltage for subsequent pulses for the pulse train shown in Figure 3.3. It can be

seen that after 650 ms the change in offset between subsequent pulses became marginal, while after 1 second, the only change was due to the noise background.

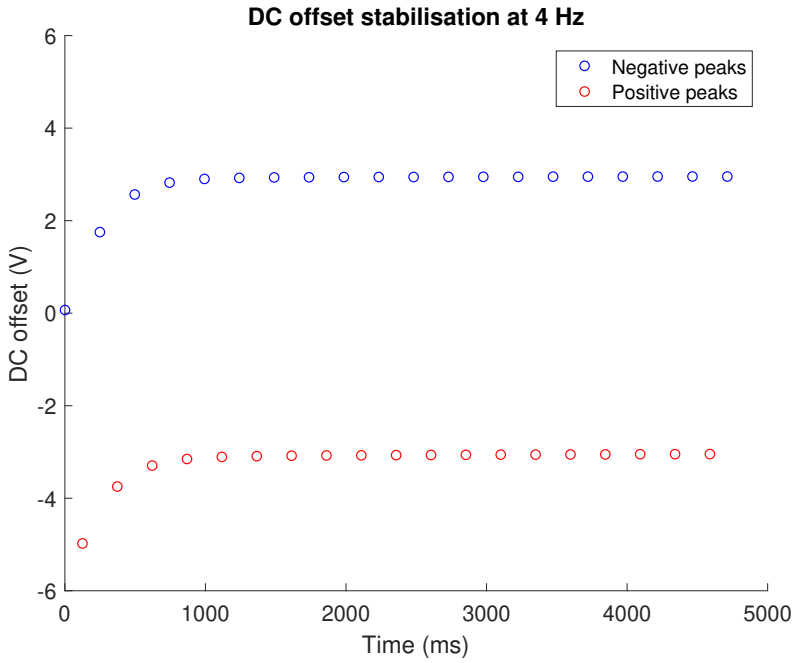

Figure 3.4: DC offset for the starting points of subsequent pulses in a pulse train.

An important conclusion of this was that the pulses before stabilisation would be distorted by the offset change, and thus wouldn't not be reliable for accurate power measurements. This didn't apply to the very first pulse as that one would start at the detector DC level and the distortion only took place once the second edge had reached the detector and the pulse's starting points were stabilising. Thus measurements could either be performed on the first pulse or on any pulse after the stabilisation. However, the fact that the first pulse commonly saturated this detector ruled it out for power measurements.

Pulse shape

In order to assess the stability of the recorded pulse shapes, the average pulse for a measured pulse train was calculated and then used to produce a standard deviation throughout the train. This noise figure directly translated into the stability of the pulse shape.

Additionally, the pulse shape with varying intensity was looked at. There are 2 situations that were considered here. First, only the very first pulse in the train was looked at to see how that one varies with intensity. This was then followed by a look at the pulses

after the train had stabilised, which also allowed the difference between the first pulse and the stabilised pulses to be shown.

Figure 3.5 shows a 3 Hz pulse at varying source amplitudes. It can be seen that the overall shape remains constant throughout the amplitudes, with the main differences being present in the relaxation region of the detector after the rise time has been reached. These differences can be explained by the fact that the relaxation behaves like an exponential decay, thus if the starting voltage on the detector is higher, the slope will be slightly steeper as well. It should also be mentioned that the pulse corresponding to 1 V modulation amplitude at the source was significantly noisier on this graph than the rest as it had been magnified by 14 times. Another notable point is the fact that the 5 V pulse was cut off, in other words, it saturated the detector, leading to issues if high intensities are used, as saturated power measurements are of no use.

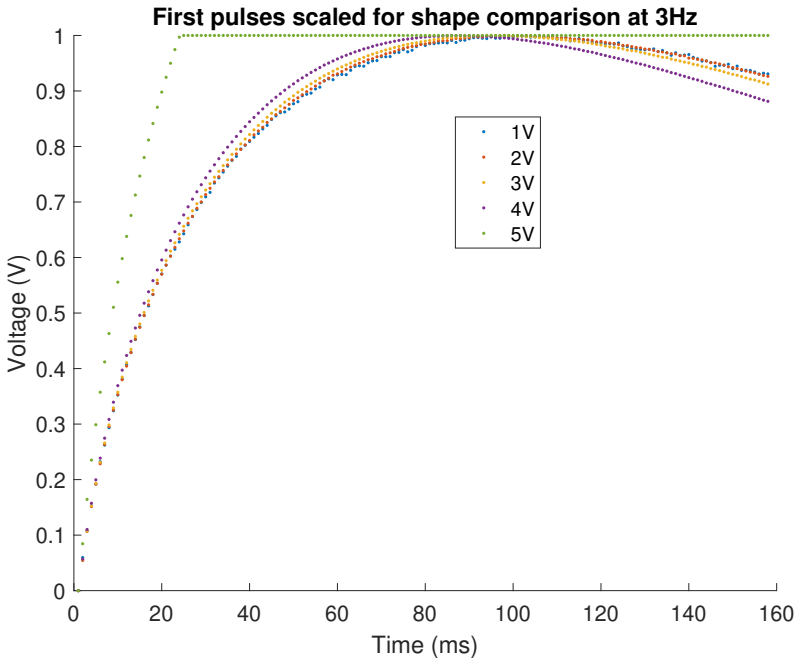

Figure 3.5: First pulses of a pulse train for varying modulation amplitudes normalised for shape comparison.

Figure 3.6 shows the average pulse from a 3 Hz pulse train at different modulation amplitudes scaled for shape comparison. Again, the pulse shape was highly consistent throughout the amplitudes, but this time, the cut off observed on the first pulse was not present anymore, which was caused by the increased measurement range due to the pulse train's stabilisation.

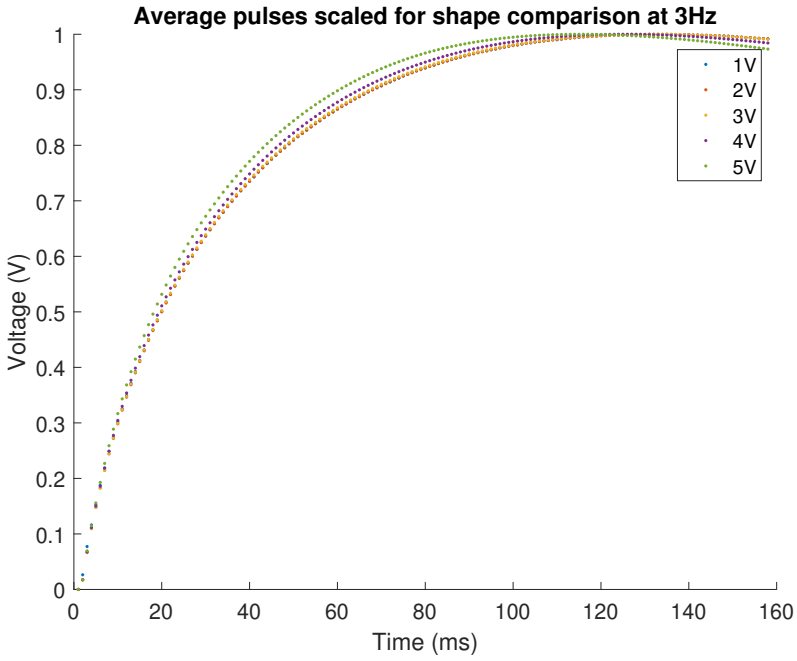

Figure 3.6: Stabilised pulses of a pulse train for varying modulation amplitudes normalised for shape comparison.

The cut off, which can be avoided if the pulse train is allowed to stabilise, is a reason to avoid using the first pulse of the train to make the power measurement. However, if the intensities that reach the detector are sufficiently small, this difference disappears, and either option works well if only considering the pulse shape.

Detector rise time

A pyroelectric detector's rise time is the time it takes for the signal to reach its maximal value. After that maximum is reached, the detector will enter its decay phase where the signal falls off towards the DC level again.

In order to measure the rise time of the detector, the maximum of each pulse was located and the time that passed since the start of the pulse was determined from the relative position of the maximum with respect to the pulse starting position. As the sampling interval was 1 ms, the number of samples from the start of the pulse to its maximum yielded the detector rise time in ms. All the information for this process was already available in the data that was being analysed since single pulses in a pulse train were identified by finding the peak positions and the pulse starting points as illustrated in Figure 3.1. This

process was repeated for various chopping frequencies, which also helped to determine an optimal chopping speed, as ideally each pulse should have a duration that is exactly the same as the detector's rise time.

Tables 3.1 and 3.2 show the measured rise time values for a range of chopping frequencies and source modulation amplitudes (with 0 V being no signal output and 5 V being 100% output). In the case of the first pulse (Table 3.1), having the source operate at full power lead to saturation for all chopping frequencies, while the rise time did not significantly change with frequency from 1 Hz up to 5 Hz. There was however a clear shift in rise time with increasing source power, where the reaction got faster with higher powers. As the change is still fairly small, it could be linked to noise. Figures 3.7a and 3.7b show a 4 Hz pulse for the different modulation amplitudes in Tables 3.1 and 3.2. The top sections of the pulses were getting flatter with reducing amplitude, which meant that the peak location was becoming more and more noise sensitive at the same time.

	1 Hz	**3 Hz**	**4 Hz**	**5 Hz**	**7 Hz**	**10 Hz**	**15 Hz**
1 V	101 ms	109 ms	102 ms	94 ms	68 ms	44 ms	9 ms
2 V	100 ms	98 ms	101 ms	92 ms	68 ms	44 ms	9 ms
3 V	96 ms	95 ms	94 ms	93 ms	68 ms	44 ms	9 ms
4 V	87 ms	86 ms	88 ms	87 ms	68 ms	44 ms	9 ms
5 V	25 ms	25 ms	25 ms	25 ms	25 ms	25 ms	9 ms

Table 3.1: Rise times for the first pulse in pulse trains at a range of Modulation amplitudes and frequencies. All values in the above table have an uncertainty of $\pm$ 3 ms.

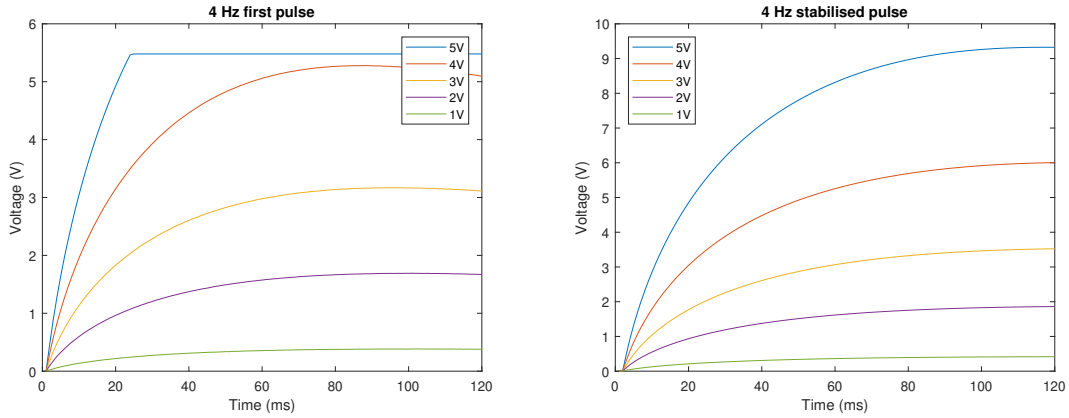

(a) (b)

Figure 3.7: (a) First pulse and (b) stable pulse at 4 Hz for modulation amplitudes from 1 V to 5 V.

	1 Hz	**3 Hz**	**4 Hz**	**5 Hz**	**7 Hz**	**10 Hz**	**15 Hz**
1 V	112 ms	133 ms	120 ms	94 ms	68 ms	44 ms	9 ms
2 V	113 ms	133 ms	120 ms	94 ms	68 ms	44 ms	9 ms
3 V	109 ms	133 ms	120 ms	94 ms	68 ms	44 ms	9 ms
4 V	101 ms	125 ms	120 ms	94 ms	68 ms	44 ms	9 ms
5 V	42 ms	114 ms	117 s	94 ms	68 ms	44 ms	9 ms

Table 3.2: Rise times for the stabilised pulses in pulse trains at a range of Modulation amplitudes and frequencies. All values in the above table have an uncertainty of $\pm$ 3 ms.

Furthermore, there was a distinct difference between the rise time of the detector for the first pulse and a stabilised pulse within the pulse train. This difference was likely caused by the fact that in the stabilised train the detector material was not at its rest state, so the range of change that it could sustain was increased, which also led to longer times needed for it to reach the limits of its range. Additionally the measured voltages were 4.5 V at full power (with respect to the ground which the signal decays to) rather than up to 5.38 V (the saturation point). As the measurements consistently showed that a smaller signal reaching the sensor took slightly longer to settle than larger signals, this additional

delay adds to the increased range of the measurements.

Source amplitude linearity

In order to perform accurate measurements with our system, it was necessary to understand how the measured signal changed as the source amplitude changed. Since no external attenuators were available for measurements, the linearity of the source was measured here with the assumption that the detector's response was linear. The amplitude of the source output was determined by an attenuator that limited the RF signal entering the AMC, thus also limiting the output power. The attenuator was controlled by a voltage between 0 V and 5 V, which for this experiment was changed linearly and the pulse power and energy for each step was calculated. These values were finally plotted against the attenuation voltage (where 5 V corresponds to full power and 0 V corresponds to full attenuation).

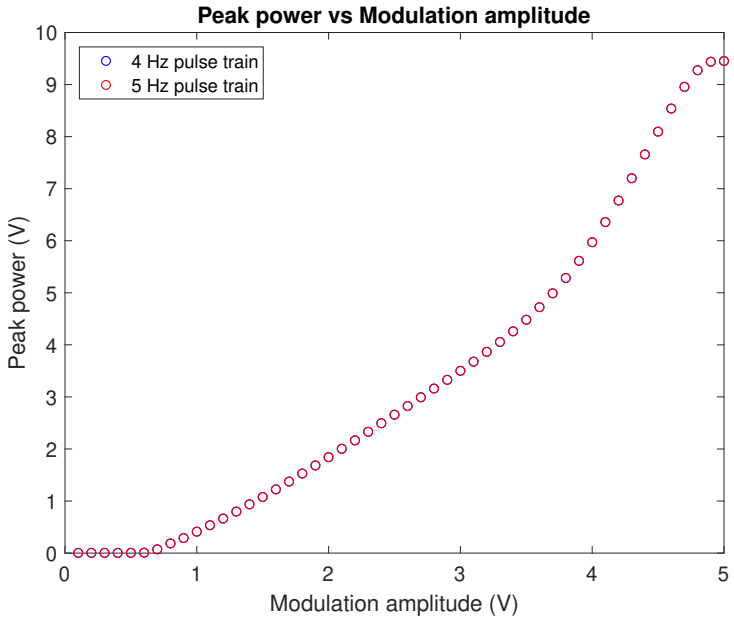

Figure 3.8: Linearity for 5 Hz signal and peak to peak measurement approach.

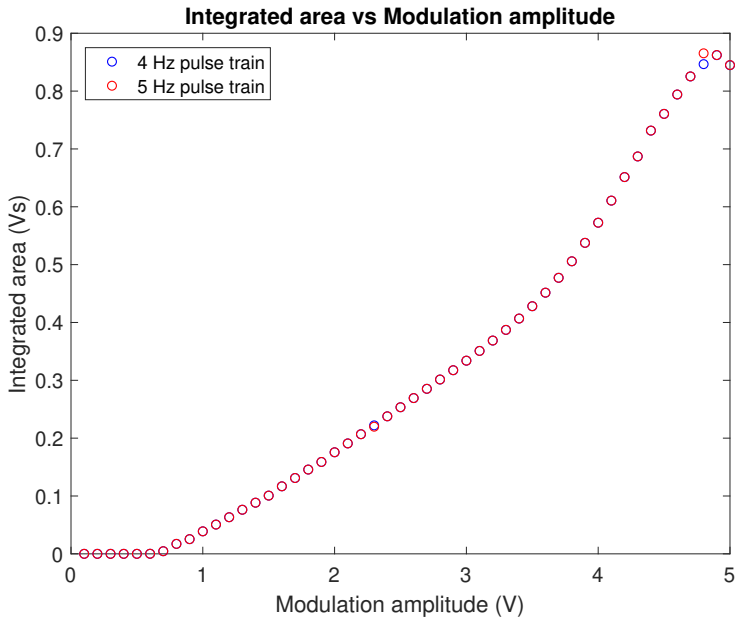

Figure 3.9: Linearity for 5 Hz signal and integrated area measurement approach.

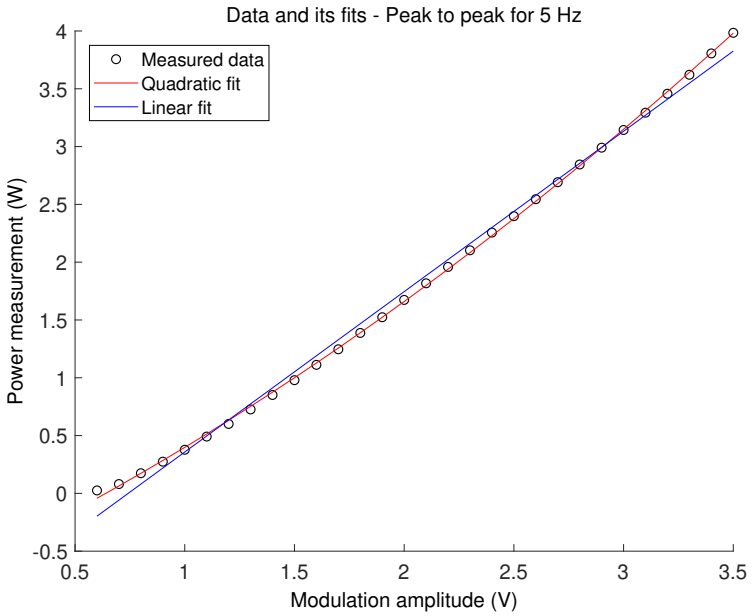

Figure 3.10: Linear and quadratic fit for the central section of Figure 3.8.

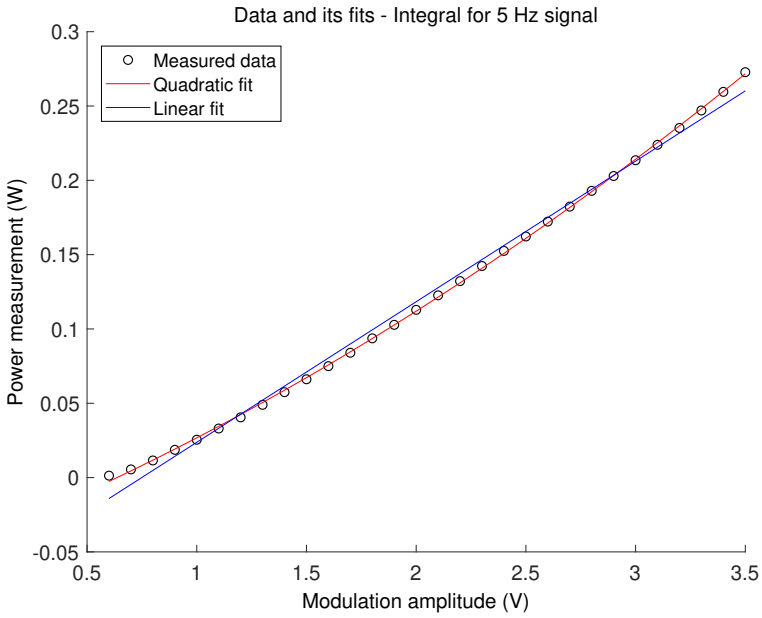

Figure 3.11: Linear and quadratic fit for the central section of Figure 3.9.

In Figures 3.8 and 3.9, an apparent region of linearity could be found between 1 V and 3.5 V, but upon closer inspection of that region, it became clear that a quadratic fit was closer to the real shape, as seen on Figures 3.10 and 3.11. The linearity of the source properties was affected by a number of factors, first amongst which was the linearity of the attenuator's response. However, there was no difference in linearity (or non-linearity) between using the first pulse only and the stabilised pulses, as well as between the 2 measurement methods. The graphs consistently showed the same shapes coming up, with the main difference being at the high intensity end where the first pulse of the train tended to be cut off (as seen in Figure 3.7a for example). Neither of the measurement methods could be deemed better than the other from the linearity considerations. Additionally the source non-linearity was not a big concern for any further experiments as it was always driven at a fixed modulation amplitude and any changes in power were caused by the sample's presence while the source output remained constant.

Measurement noise

Another important consideration was the amount of noise present in the power/energy measurements. The motivation for these measurements was to find the noise floor of the system. In order to assess this, the power was calculated for each pulse in a stabilised

train and compared to the power/energy measured on the average pulse for that train. By comparing this last value to all the separate pulse powers/energies, an estimate of the error in form of a standard deviation could be performed. In order to compare the values achieved with the peak value approach and the integrated area one, the standard deviations were normalised to the peak value and the integrated area of the average pulse respectively. The result of this for a range of frequencies are shown in Figure 3.12.

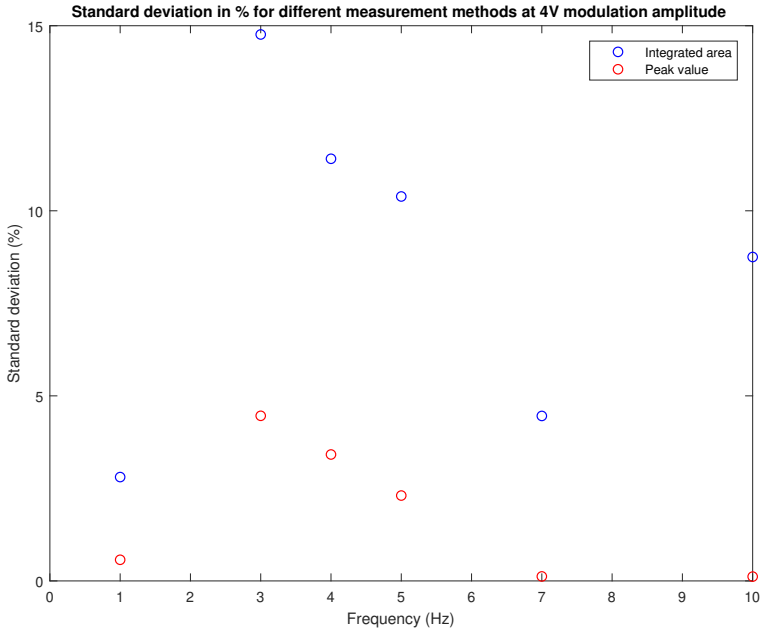

Figure 3.12: Normalised standard deviations for both measurement methods at various modulation frequencies.

The noise in the integrated area was larger than that of the peak to peak measurements across all the chopping frequencies, which indicates that the pulse shape was less constant than its peak value. Furthermore, the noise went down with increasing chopping frequency. The shape of the noise values for the peak to peak measurement can be explained by the different regimes that the pulse is in for different chopping frequencies. 1 Hz tends to saturate the detector, and since the saturation value is constant, there is no noise on the peak value, though the measurement itself is of no use. Between 3 and 5 Hz the pulse length is longer or comparable to the detector rise time, at which point the noise on the plateau and exponential decay impacts the measurement, which is more noticeable here due to the small variation in detector voltage close to the peak. Finally above 5 Hz, the pulse in in the middle of its rise, which is very consistent, and gets cut off at the same point in time each time, leading to very low noise figures again.

3.2.3 THz-9D with M-Link

Introduction

Originally the THz-I-BNC was meant to be used for most of the experiments around the project, however the lack of a specification sheet of when it was purchased lead to uncertainty in terms of the maximal average power that it could measure, since newer specification sheets quote it at 70 μW, while our source output is up to 1 mW. In order to circumvent any potential saturation issues and to avoid potentially damaging the sensor material, it was replaced with a THz-9D, again manufactured by Gentec-eo and operated with their M-LINK universal meter. The maximum average power in this case was at 25 mW, which left ample breathing room. Furthermore, it operated at a chopping frequency of 10 Hz which was imposed by the M-LINK's processing software, however, since that is twice the typical chopping frequency for the THz-I-BNC, it was seen as a bonus since it would double the measurement speed. Throughout this section, the parameters that will be presented are broadly the same as in the previous section, as the same characterisation approach which was developped througout the analysis on the THz-I-BNC was applied to the new detector. One difference was that the chopping frequency wasn't varied as it was imposed by the detector rather than being recommended. Additionally, a comparison between using the digital power measurements from the M-LINK against calculating the power from the analogue output was made.

Figure 3.13 shows a pulse train taken with the THz-9D at 2 V modulation amplitude. It should be noted that there are clear jumps in the signal offset and amplitude which were caused by the detector's inbuilt scaling. If the signal drops below (or rises above) certain thresholds, the detector would switch to a different amplifying stage, a jump that was not visible in the digital power reading, as it corrected for that, but which made analogue analysis harder to carry out, as the power values at which it changes amplifying stages and the specific levels of amplification for each of the different ranges were not available to the user. The auto-range function had been disabled as far as possible for the following experiments.

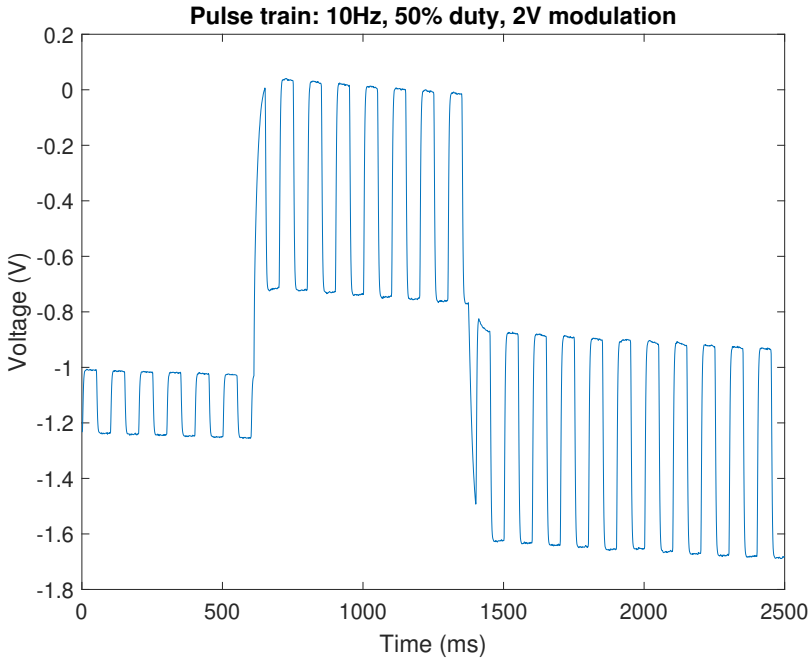

Figure 3.13: Typical analogue signal output for the THz-9D, highlighting the issues with its auto-scaling function for analogue analysis.

Another notable feature on Figure 3.13 is that the rise time of this detector is significantly faster than the previous one's. The detector spends $\frac{4}{5}$ of the time in the decaying state with 10 Hz chopping with the detector rise time being 10 ms, which is about 10 times faster than the THz-I-BNC.

Pulse shape

Following the same approach as in Section 3.2.2, the shape of the first and last pulses in a pulse train measured with the THz-9D was looked at to get an idea of its stability. Figure 3.14 shows the first pulse of a pulse train at 10 Hz modulation for amplitudes between 1 V and 5 V. There were some clear differences in shape between the different amplitudes of pulses, most markedly around 6 ms into the pulse.

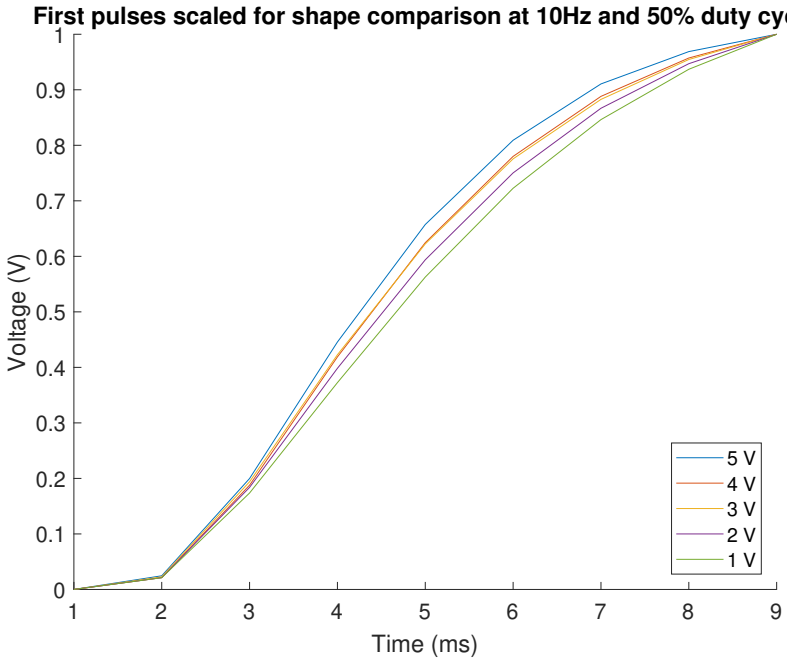

Figure 3.14: First pulses of a pulse train for varying modulation amplitudes normalised for shape comparison.

The stabilisation itself typically took 2 or 3 pulses as can be seen on Figure 3.13, where even after the scale changed the signal levels were stable after at most 3 pulses. Figure 3.15 shows stabilised pulses for different modulation amplitudes normalised for comparison. The differences between the power levels were markedly smaller than they were on the first pulse, meaning that the most accurate power measurement could be made by disregarding the first couple pulses.

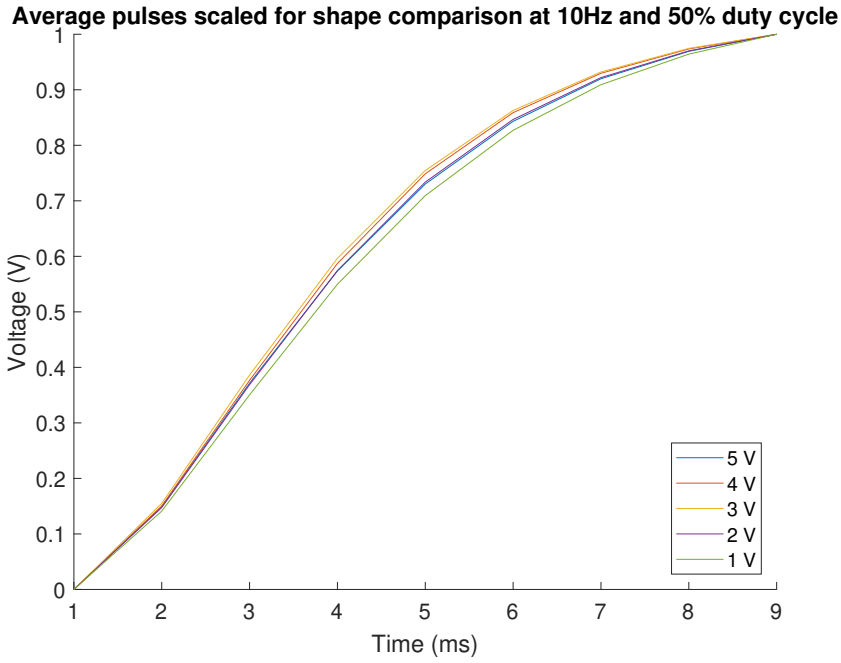

Figure 3.15: Stabilised pulses of a pulse train for varying modulation amplitudes normalised for shape comparison.

Source amplitude linearity

In order to assess the amplitude linearity with this source/detector pair, pulse trains with modulation amplitude values between 0.1 V and 5 V in steps of 0.1 V were recorded. As mentioned before, the auto-range function was disabled as far as possible in the driver software, but it still kicked in for amplitudes below 1.9 V, which shows in Figures 3.16 and 3.17 for both measurement approaches. Through trial and error the difference in gain between the part before 1.9 V and the one after was found to be roughly a factor of 3, however that includes the subjective assumption that the shape of the graph was going to be the same for this detector as for the previously tested one, assuming again that the detector response is linear and all the non-linearities were carried by the source properties. While the two responses generally looked very alike above 1.9 V, it was deemed unwise to simply assume that this applied for the bottom end of the graph as well.

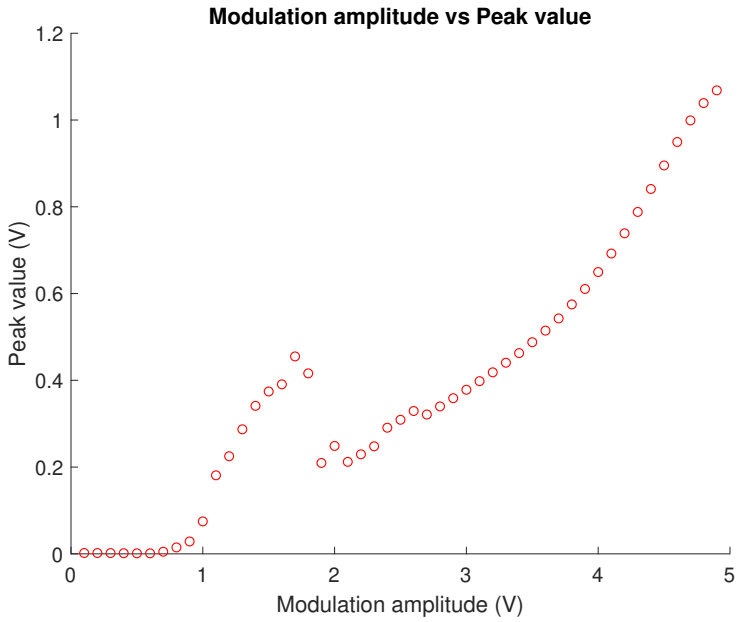

Figure 3.16: Linearity for the peak value approach.

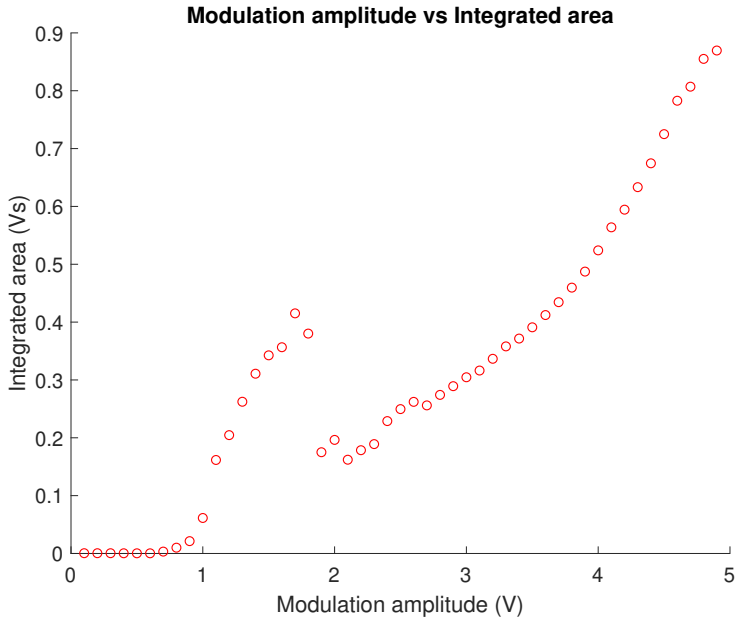

Figure 3.17: Linearity for the peak value approach.

While the analogue power measurements were showing good agreement on the higher power end of the above Figures 3.16 and 3.17 to Figures 3.8 and 3.9, the lower end couldn't be directly compared due to the way the detector firmware was overwriting the user's attempts to fully block the auto-range function. Hence, the digital power measurements were looked at as well to assess the detector response to different source inputs. Figure 3.18 presents the results of those measurements. It is worth pointing out that the

signal was cut off below 1 V, as the digital power measurements have a lower threshold for the power they put out for a given measurement range, which means one had to keep in mind that information would get lost if the power levels dropped very low.

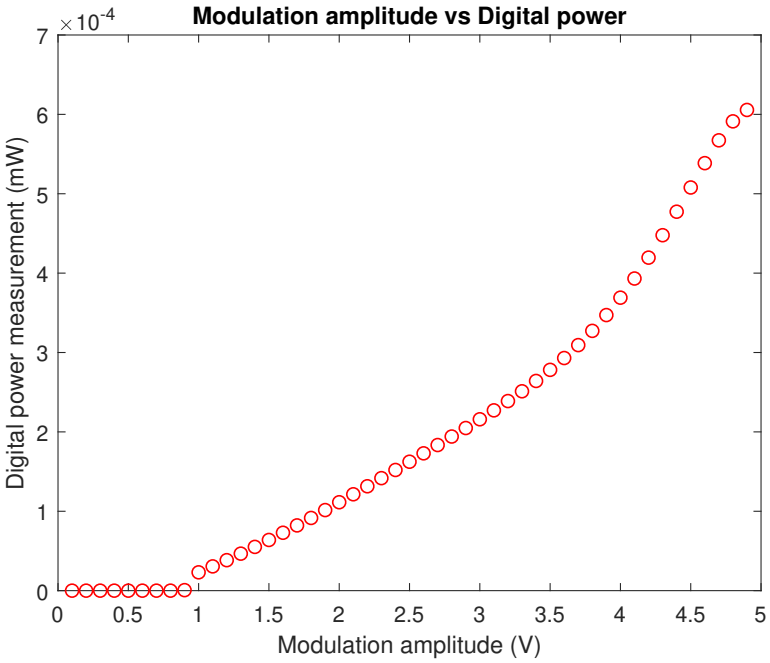

Figure 3.18: Linearity for the digital power measurements.

Finally, Figure 3.19 compares the linearity curve attained with the peak to peak measurements shown in Figure 3.8 to the data for the digital power measurements presented in Figure 3.18. There was very good agreement between the two detectors, where the main differences were at the lower end where the digital measurement thresholded to zero and at the top end where the THz-I-BNC was getting close to saturation, which likely affected the power measurements. The agreement also pointed out that the assumption of linearity was acceptable, as it is highly unlikely that 2 different detectors which are expected to be linear would show the same non-linearities. This was corroborated by the source manufacturer's statement that the the source output was affected by ambient conditions and changed from device to device while generally not being linear.

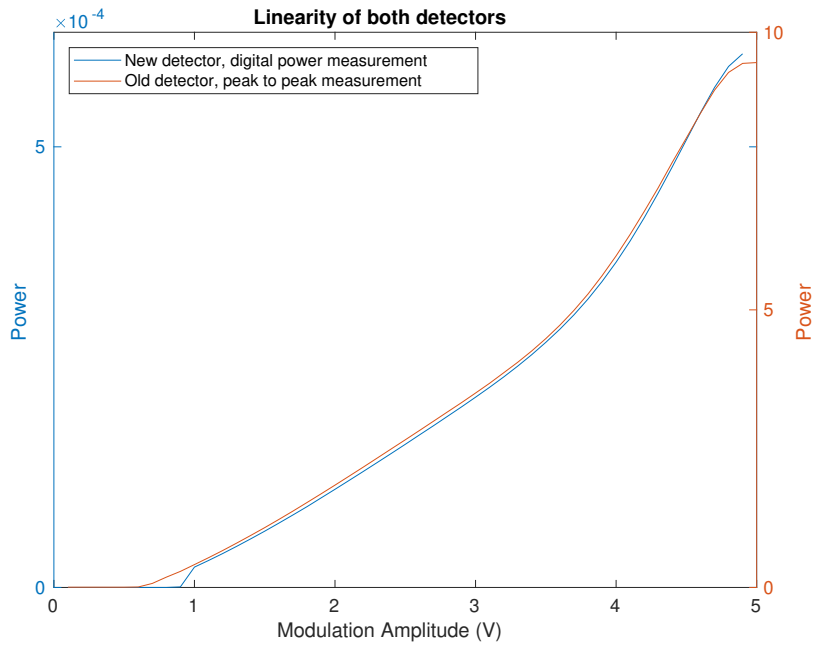

Figure 3.19: Linearity comparison for the two detectors.

Power measurement noise

Again, investigation of the noise floor of the detector provides crucial information as to the reliability of any measured signals. Two kinds of noise were considered at this point. First is the random baseline noise inherent to the detector at the typical ambient conditions in the lab. The second is kind was misreadings caused by vibrations picked up through the floor. Chief cause of vibrations that were picked up was people unlocking their offices along the corridor. While the system was on an optical bench which could float on an air cushion, however the system was also within an anechoic chamber with too much weight for the air cushion to stay inflated any longer than 10-15 minutes.

The random noise was assessed on both the analogue and digital signals, however only the peak to peak method was considered for the analogue signal, as that was the method by which the digital measurements were generated as well. For the analogue measurements, the variation of the peak voltage reached by successive pulses within a pulse train was calculated, while for the digital measurements, the standard deviation of a number of successive measurements was calculated. In order to relate the two noise figures, the source power for the measurements was assumed to be 1 mW, with the error getting expressed in mW as well, using the relation between the measured power voltage/value

as conversion factor.

For a mean analogue measurement of 1.068 V , the corresponding standard deviation for 100 pulses was found to be 0.53 mV . Looking at the digital measurements lead to a mean power value of 605.56 μW with a deviation of 0.57 μW . Converting the two values for comparison as mentioned above lead to a value of 0.49 μW for the analogue case and 0.94 μW for the digital case. The digital power measurement might take it's peak to peak measurement from consecutive minima to maxima (and vice versa), which would mean that the uncertainty should be expected to be around twice that of the analogue case, where the starting point of the pulse is accurately determined using the gradient of the signal rather than the extrema of the previous pulse.

Another factor that needed to be considered and either corrected or simply removed from the measurements was any external vibrations affecting the detector through the floor. Figure 3.20 shows an example of subsequent power measurements with vibrational interference (someone unlocked a door somewhere along the corridor). There is an obvious power spike when the vibration reached the detector.

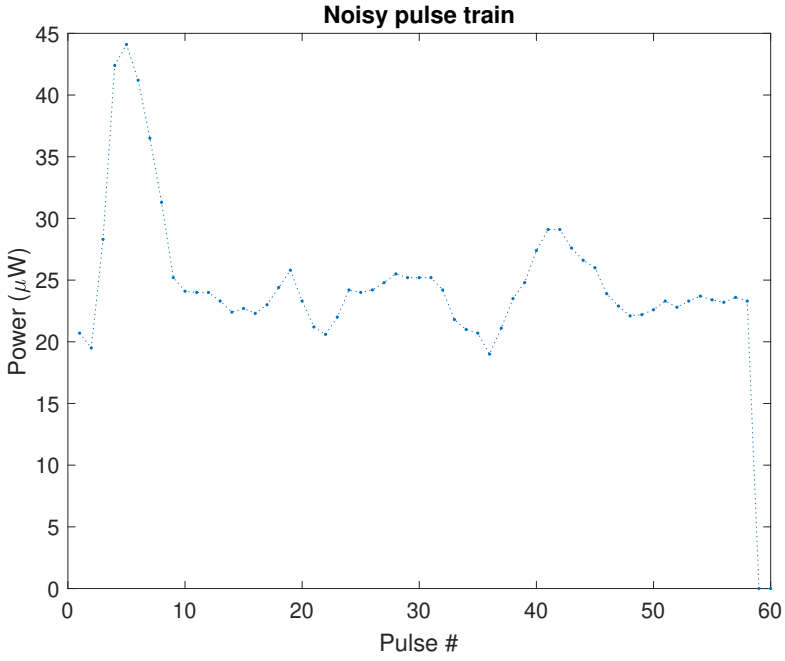

Figure 3.20: Power measurements with vibrational noise present.

Figure 3.21 on the other hand shows a case where no vibrations were present. The measured values were generally very stable unless there was external interference with

the system, however, that external input tended to only last for short period of time.

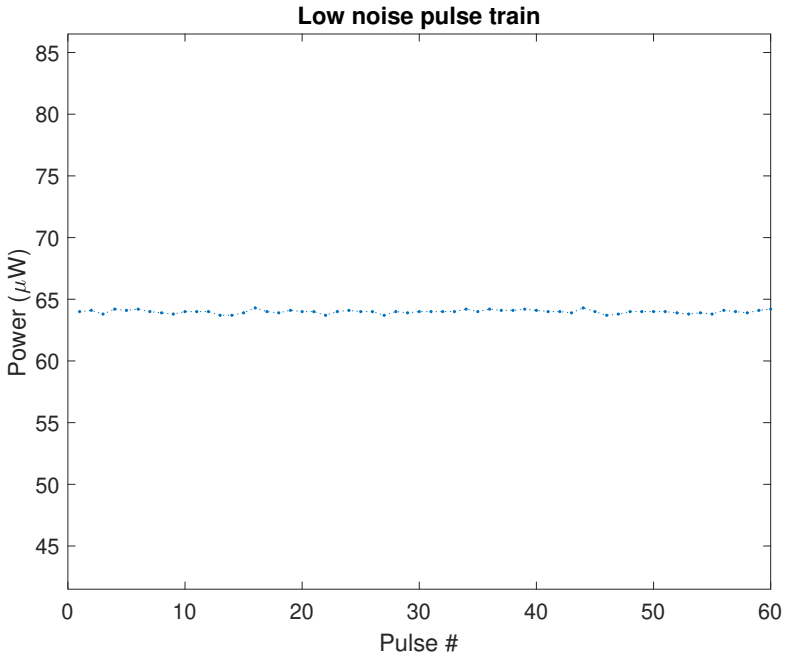

Figure 3.21: Power measurement without vibrational noise.

As all measurements involved taking between 5 and 10 power measurements and then taking an average as the final reading for that point, the most efficient way of dealing with these short bursts of noise was deemed to calculate the standard deviation of the current measurement and simply repeat it in the case that it breached an empirical threshold (found to be 0.3 μW) which would only be breached if external noise had affected the reading. It should be noted that on the vibration isolation experiments the system was set up for confocal imaging, at which point the maximum power that propagated through was of the order of 100 μW. A standard deviation of 0.30 μW for a total power of 100 μW would be equivalent to an error of 1.8 μW for a total power of 600 μW. Thus compared to the figure for the random noise in these measurements (0.94 μW), the chosen threshold value didn't limit what data was taken as valid while removing any big external influences.

Throughout this Section, the performance of 2 different pyroelectric detectors has been presented. Additionally, the best approach to perform the measurement with them was considered.

In the case of the THz-I-BNC, issues with its power measurement range were flagged up, and the energy measrurements were found the be less reliable at the high energy end

on the range and were generally noisier. Additionally, since it was computationally a lot simpler to measure peak to peak values over integrating the pulse area, this was kept as the main method.

Analysis of the THz-9D helped to conclude that the non-linearities in the amplitude response were mostly due to the source properties, and while integrating had noise advantages for the other detector, the very fast rise time of this model meant that there was not enough samples in the pulse for any real averaging benefit to happen by integrating. Additionally, the digital measurements that the system performs are peak to peak measurements, so in order to assess how well those measurements were performing, it was decided to compare likes to likes. The noise figures showed that there was twice as much noise on the digital values than the ones calculated from analogue values, however, in light of the specifics of how the measurements were performed, this was a sensible result. The bottom line of these experiments was that there was no drawback to using the digital power measurements as they were read from the detector over calculating the power manually from analogue traces, especially since the changes in amplifying stages made the analogue traces only semi reliable.

3.3 Stress-optic coefficient measurements in transmission

3.3.1 Introduction

In this Section, the first observation of stress induced birefringence in a ceramic, specifically yttria-partially stabilized zirconia (YTZP), by measuring the direct stress-optic coefficient is reported. Changes in refractive index of ceramic specimens were measured as a function of applied stress, from which the direct stress optic coefficient was determined. A direct stress optic coefficient for polytetrafluoroethylene (PTFE) was also measured in order to investigate the discrepancy between previously published values. The measurements are all made with 260-380 GHz illumination.

3.3.2 Experimental Set-up

Figure 3.22 shows a schematic of the experimental set-up, a plane polariscope comprising a source, polariser, specimen, analyser and detector. The source (S) was a Virginia Diodes synthesizer and amplifier/multiplier chain that generated a continuous-wave signal tunable between 260 and 380 GHz. A diagonal feed horn launched a vertically polarised, diverging electromagnetic wave that was focused onto the sample, with a spot size of approximately 5 mm, using a pair of 50 mm diameter PTFE plano-convex lenses (L). A linear polariser (P) was placed between the sample and focusing lens with its transmission axis parallel to the plane polarised source, i.e. vertical. A second polariser acting as an analyser (A) was placed after the specimen, also with its transmission axis vertical, i.e. bight field polariscope configuration. This configuration was chosen due to the high absorption coefficient of the ceramic. While a dark field setup would be more sensitive to small changes, a large fraction of the fresnel fringes that were being mesured risked being below the system noise floor, while the bright field setup yielded some perfectly workable data. A second pair of PTFE plano-convex lenses coupled the beam to a pyroelectric detector (D) (Gentec-eo THZ-9D). All the measurements were conducted in an anechoic chamber comprising RF absorbing tiles. Additional RF absorbing titles were placed around the aperture of the feed horn and the detector. Both the polariser and analyser were tilted to an incidence angle of 45° with respect to the optical axis, as shown in Figure 3.22, to reduce standing waves between the sample and focusing lenses. System alignment was carried out by placing one optic into the beam path at a time and scanning the beam with the detector to optimise the optic's position, no alignment lasers were used as the PTFE lenses stop them from propagating through the system properly.

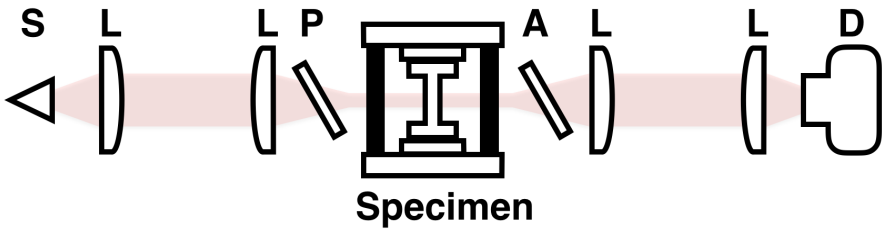

Figure 3.22: Schematic of the experimental arrangement used to measure the stress optic coefficient. Source (S), detector (D), plano-convex lens (L), polarizer (P) and analyser (A).

A Deben 2 kN dual leadscrew tensile testing stage was used to load the samples. Figure 3.23a shows the tensile stage, with a sample, in the polariscope. Load was applied parallel to the polarisation axis of the illumination. Figure 3.23b shows the geometry of the YTZP and PTFE specimens tested.

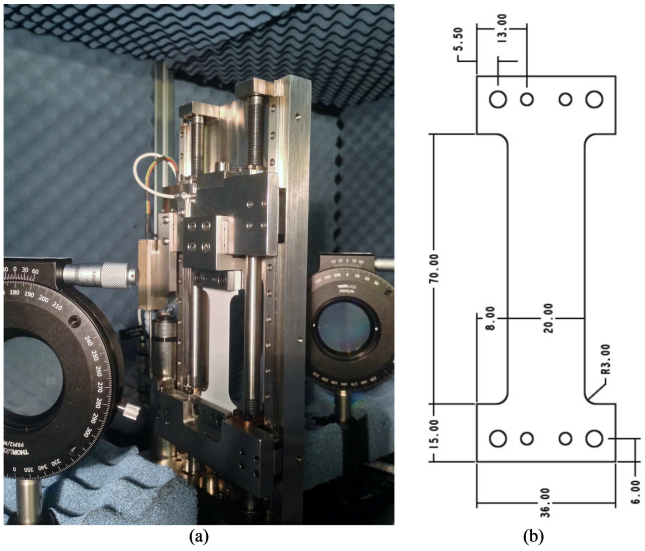

Figure 3.23: Specimen used for tensile tests. (a) Specimen in Deben tensile stage with polariser and analyser visible, tilted with respect to the optical axis to reduce standing wave interference. (b) Specimen dimensions, in millimetres, with inner dowel pin holes 3.1 mm diameter and outer M4 clearance holes 4.2 mm in diameter.

Three YTZP ceramic (Technox® 2000) samples were sintered and fired at 5 mm thickness by CoorsTek. Each specimen was then ground down to a thickness of 656 ± 5 μm in order to obtain sufficient transmission through the polariscope. Calculation of the initial sample thickness is described in the next section. The grinding direction was parallel to the loading axis of the samples, and therefore parallel to the polarisation axis of the illumination. The YTZP had a density of 6.02 g·cm^{-3}, an average crystal size of less than one micron, a Youngs modulus of 210 GPa and Poissons ratio of 0.3, values supplied by the manufacturer.

PTFE samples were laser cut from extruded sheet and had an average thickness of 2.177 ± 0.034 mm. Again, calculation of the initial sample thickness is described in the next section. One set of six samples were cut with the loading axis perpendicular to the direction of extrusion from the bulk PTFE sheet. A second set of six samples were cut with the loading axis parallel to the direction of extrusion from the same PTFE sheet.

The PTFE had a Youngs modulus of 500 MPa and Poissons ratio of 0.46, values supplied by the manufacturer. The Youngs modulus value was confirmed in an independent experiment.

3.3.3 Measurement Procedure

Before loading each sample, the tensile stage load cell was balanced, because clamping samples into the stage inevitably creates a small applied load. Balancing simply involves setting the tensile stage to apply a load of 0 N once the specimen has been clamped in place. In this manner, the absolute load applied to each sample could be measured. For each specimen, fifteen refractive index measurements were taken at constant load settings between 0 and 350 N, with a 25 N spacing. Sample extension was adjusted by the tensile stage in order to maintain a constant load during each refractive index measurement. For YTZP at all loads, and PTFE at lower loads, any change in extension was minimal during the measurement period, as shown in Figure 3.24a. Note that the maximum extension in the figure has been normalized for comparison, and is approximately 30 times smaller for YTZP than for PTFE at the same load. Creep became apparent at higher loads for PTFE samples. The initial and final elongation of the sample was recorded during measurement of the refractive index in order to show the associated uncertainty in the applied stress. An appreciable change in the strain due to creep is associated with the onset of photo-viscoelastic effects, which are not the subject of this thesis.

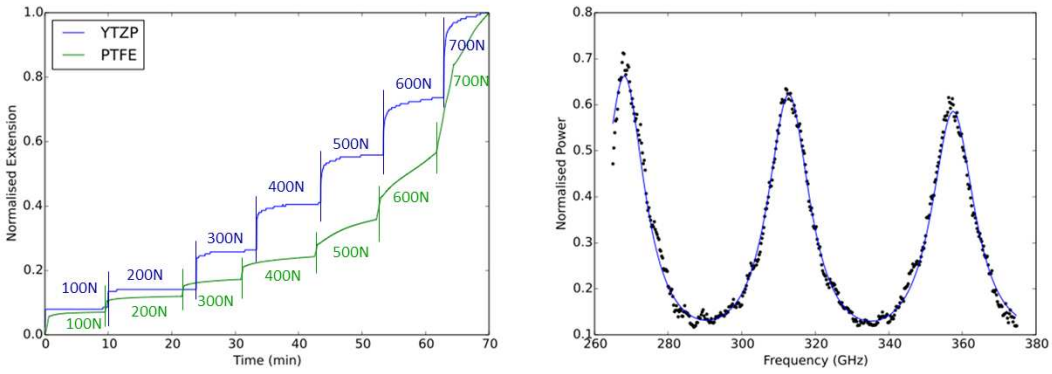

Figure 3.24: Typical measurements. (a) Normalized extension of YTZP and PTFE specimens during application of sequential constant loads. YTZP extension is approximately 30 times smaller than PTFE. (b) Transmission through a YTZP specimen recorded during a scan of the source frequency from 260–380 GHz (points) at 50 N constant load and the subsequent fit of the Fresnel equation (line).

At each constant load applied to a specimen, the frequency of the illumination was scanned between 260 and 380 GHz in steps of 0.25 GHz and the signal transmitted by the specimen was recorded. A frequency scan without the specimen was also recorded so that frequency related variations in source emission and detector response could be normalized. A typical normalized spectrum for YTZP is shown in Figure 3.24b. Increased absorption by the YTZP specimen as the frequency increases is shown by a reduction in peak height.

The complex refractive index was extracted from each normalized frequency spectrum, using a nonlinear least squares fit of the Fresnel equations for a single dielectric slab. If the dielectric is surrounded by air ($n_{air} = 1$), the transmission coefficient is [71, 72],

$$T = \frac{\tau_1 \tau_2 e^{-ikl}}{1 + \rho_1 \rho_2 e^{-ikl}} \tag{3.1}$$

where ρ_1, ρ_2, τ_1 and τ_2 are the Fresnel coefficients,

$$\begin{aligned} \rho_1 &= \frac{1-\tilde{n}}{1+\tilde{n}} \\ \rho_2 &= \frac{\tilde{n}-1}{\tilde{n}+1} \\ \tau_1 &= \rho_1 + 1 \\ \tau_2 &= \rho_2 + 1 \end{aligned} \tag{3.2}$$

where $\tilde{n}$ is the complex material refractive index, k is the propagation wave number and l is the sample thickness. For a dielectric with appreciable absorption, such as YTZP, $\tilde{n}$ and hence T are represented as complex quantities. The real part of $\tilde{n}$ is the refractive index, n, and the imaginary part is $(c\alpha/2\omega)$, where α is the absorption coefficient, c is the speed of light in a vacuum and ω is the angular frequency of the illumination. The power measured by the detector is T multiplied by its complex conjugate, resulting in a real valued function to which the experimentally measured transmitted power was fitted.

Initially, each sample thickness was measured using a digital micrometer with a 1 μm resolution. Using this thickness as an initial estimate, a non-linear least squares fit of the Fresnel equation was performed for each sample for the measured 0 N frequency spectrum, in which the thickness, refractive index and absorption coefficient were allowed to vary. For subsequent measurements at increased constant loads, this initial measured thickness was held constant whilst the refractive index and absorption coefficient were allowed to vary. Figure 3.24b shows an example of the fitted Fresnel equation to the experimentally measured frequency spectrum for YTZP loaded at 50 N. This analysis approach assumed the change in thickness with applied load to be negligible. The analysis was performed a second time, this time allowing for the thinning of the sample cross section with applied load.

3.3.4 Results

In order to obtain a direct stress optic coefficient, the refractive index, n, was plotted as a function of applied stress for each sample at each load. A linear fit was then applied to each data set in order to determine the stress optic coefficient. YTZP and PTFE are described separately in the following two sections. YTZP samples showed a typical absorption coefficient of 2.5 cm^{-1}, while PTFE did not show a measureable value.

YTZP Ceramic

The refractive index measured at each load is plotted against the applied stress for YTZP samples in Figure 3.25a. Stress was calculated by dividing the load by the initial, unloaded cross-sectional area of each specimen, with the initial thickness measured by the zero load

fit (described in the previous section), and the width measured with the micrometer. Three YTZP samples were tested and each sample was measured twice. Figure 3.25a shows excellent repeatability for each sample, but a small offset exists between the respective samples.

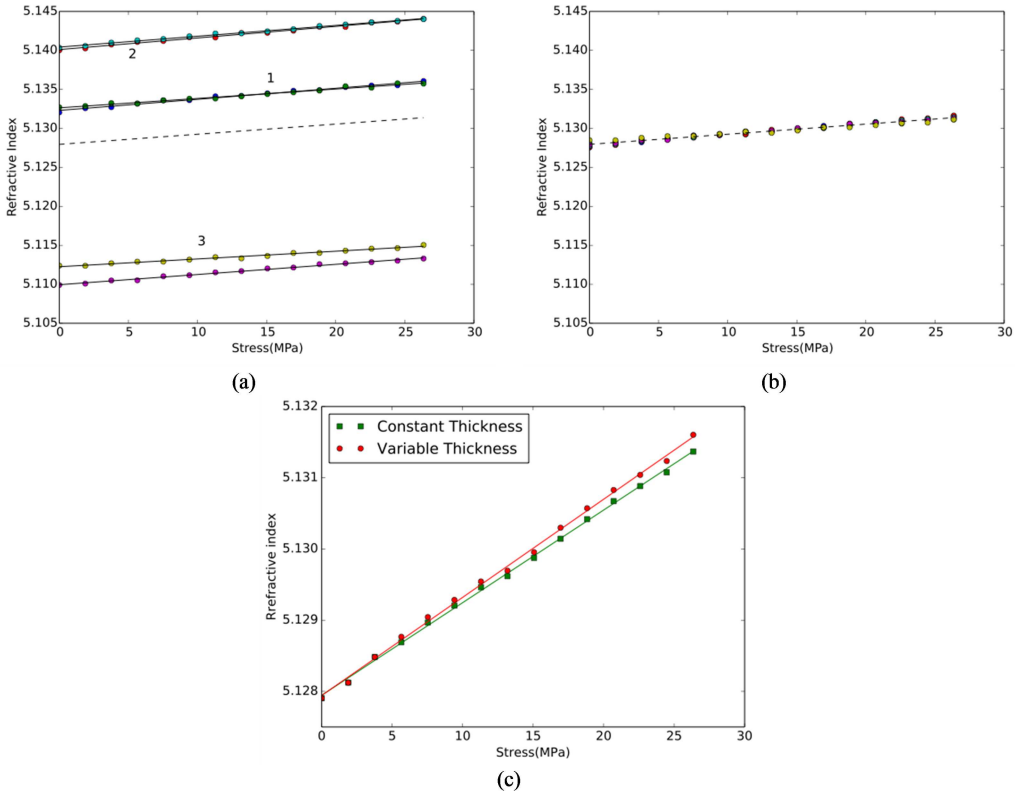

Figure 3.25: Refractive index plotted against applied stress for YTZP. (a) Two repeated measurements for three samples (numbered). (b) Removal of offset in refractive index between samples due to thickness measurement uncertainty. Both (a) and (b) assume constant specimen thickness in the analysis. (c) Comparison between analyses assuming constant or variable specimen thickness.

These small offsets are explained by the uncertainty in the measured thickness of each specimen, rather than by any significant difference in material properties caused by the manufacturing process (including grinding). To demonstrate this, Figure 3.26 shows the results of a simulation in which small changes in the assumed sample thickness modify the refractive index values calculated by the non-linear least squares fit to the Fresnel equations, i.e. a numerical estimate of dn/dl. For the simulation, transmission curves were calculated using Equation 3.1 taking the average refractive index value for the zero stress points in Figure 3.25) (5.128) and thickness values between 0.653-0.664 mm with

a spacing of 0.1 μm. A non-linear least squares fit to the Fresnel equation was then applied to each of the calculated transmission curves to recalculate the refractive index, but using a fixed thickness of 0.653 mm. Figure 3.26 shows the difference between the refractive index recalculated from the fit and the nominal value used in calculating the transmission curves, plotted against the difference between the thickness used to calculate each transmission curve and the fixed thickness used in the fit, from which dn/dl = -0.0078 μm^{-1}. The refractive index offset between the three samples from Figure 3.25a of approximately 0.03 therefore corresponds to a potential difference in thickness of just 3.8 μm, well within the uncertainty of the thickness measurement.

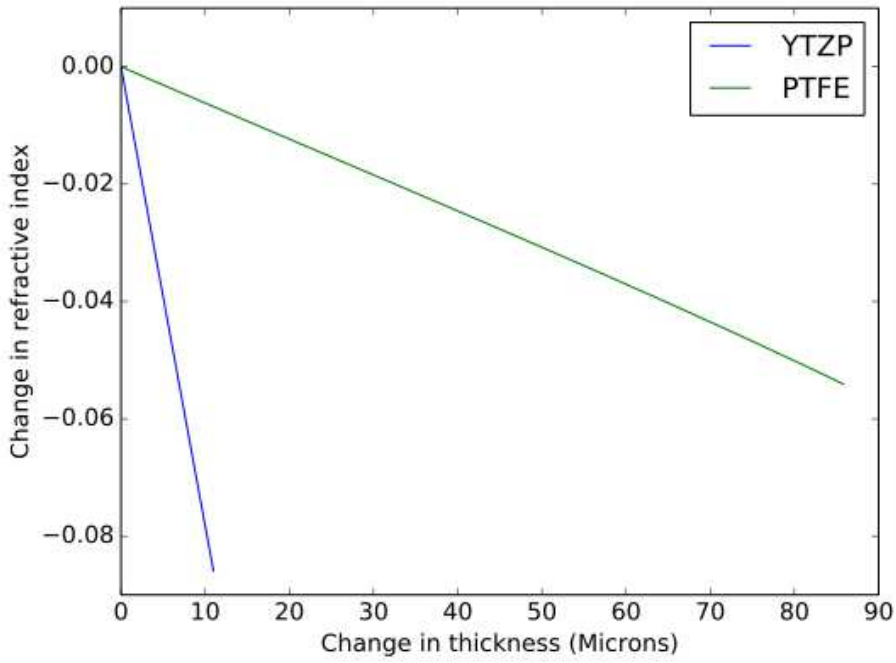

Figure 3.26: Results of a simulation of the change in refractive index as a function of thickness, dn/dl for YTZP and PTFE.

Clearly, small thickness-related offsets in the absolute refractive index are not important when calculating the stress optic coefficient for which the change in refractive index with a *change* in stress is important. Therefore, the refractive index offset between the samples was removed by fitting a cubic function,

$$f(\sigma) = a\sigma_3 + c\sigma_2 + x\sigma + d \tag{3.3}$$

to each data set in Figure 3.25a. A cubic function was chosen because viscoelastic behaviour results in non-linear response of the refractive index to applied stress [73]. While YTZP (Figure 3.25) remained elastic and therefore has a linear refractive index response

to applied stress, PTFE will be shown in the following section to exhibit a viscoelastic behavior (Figure 3.27). Therefore, a cubic function was chosen to use the same processing for both cases. A new function $f_0(\sigma)$ was fitted to the mean refractive index at each stress. The scalar term d for each data set was then varied to minimize the least-squares difference between the fitted curves and $f_0(\sigma)$ while the constants a, b and c were kept fixed. Figure 3.25b shows the normalized refractive index where the variation in the term d for each data set has been subtracted from each point in the data set. This process maintains the functional shape of each sample curve, but removes the refractive index offset due to measurement uncertainty in the specimen thickness.

Finally, Figure 3.25c shows the mean refractive index at each stress measurement point from Figure 3.25b plotted against stress. Assuming a constant sample thickness under loading, i.e. engineering stress, the direct stress optic coefficient calculated from a least-squares linear fit is 0.13 ± 0.02 GPa^{-1}. This line is shown in Figure 3.25c and also by a dashed line in Figure 3.25a and 3.25b.

In practice, the sample cross-section decreases slightly as the load increases, i.e. true stress. At each load, the instantaneous sample thickness and width can be estimated from,

$$\Delta d = \frac{dvP}{AE} \tag{3.4}$$

where d is the initial dimension (thickness or width) at 0 N load, ν is Poissons ratio, E is the tensile modulus, P is the applied load and A is the initial cross-sectional area. Equation 3.4 is valid when a material is in the elastic regime. Tensile tests showed that YTZP was elastic over at least the applied load range (0 to $\sim$27 MPa). In a repeat calculation, the instantaneous sample thickness at each load was also used in the non-linear least squares fit to the Fresnel equation used to calculate the refractive index: the fit was repeated at every load for each specimen and the thickness was also allowed vary, in addition to the refractive index and absorption coefficient. Figure 3.25c shows the mean refractive index calculated at each load allowing for changes in the specimen thickness, which introduces changes both to the value of n via the fit to the Fresnel equation and to the stress via the instantaneous cross-sectional area. The direct stress optic coefficient calculated from a least-squares linear fit is 0.14 ± 0.02 GPa^{-1}. The difference between the variable and constant thickness analyses is small, which is to be expected due to the high tensile modulus of YTZP.

PTFE

Figure 3.27a shows the measured refractive index plotted against applied stress for the PTFE samples that were cut with the long specimen axis perpendicular to the extrusion direction of the bulk sheet. Six independent samples were tested. Unlike YTZP, plastic deformation meant that PTFE samples could not be used for repeated tests. Once again, the results show a vertical offset in the measured refractive index between samples, which can be explained by a combination of small errors in the measured sample thickness and variations in the manufactured sample thickness. To demonstrate this we used the simulation of dn/dl as described in the previous section. Figure 3.26 shows the change in refractive index versus change in thickness from the simulation with PTFE. The average refractive index for the zero stress points in Figure 3.27a (1.4013) and thicknesses between 2.083-2.169 mm with a spacing of 10 μm were used to calculate the transmission curves, and the refractive index was recovered with the non-linear least squares fit using a fixed thickness of 2.083mm. From Fig. 5, dn/dl = -0.63 mm^{-1}. The difference in measured refractive index between the six samples from Figure 3.27a of approximately 0.046 therefore corresponds to a potential difference in thickness of 73.5 μm, which is somewhat larger that the thickness variation seen for YTZP. The PTFE specimens were manufactured from standard extruded sheet, while the YTZP specimens were ground to their final thickness. We typically measured a 21 μm thickness variation across the PTFE specimens, which produced a larger uncertainty in the thickness recovered by the fitting procedure. Despite this offset in absolute refractive index values, Figure 3.27a shows that the shape of each trace is highly repeatable for each specimen, and once again it is the change in refractive index with a change in stress that is important when calculating the stress optic coefficient. PTFE results show strong viscoelastic behavior above $\sim$4.5 MPa, approximately 200 N for the sample dimensions used here. Hence the offset between the measured refractive index due to uncertainty in measured sample thickness was removed by a similar fitting process as described in the previous section, but applied to the data points predominantly linear elastic region below 4 MPa only.

Figure 3.27b shows the normalized refractive index where the constant term in the fit for each data set has been adjusted to minimize the least-squares difference between the fitted curve and $f_0(\sigma)$, while the constants a, b and c were kept fixed. As before, this process maintains the functional shape of each sample curve, but removes the refractive

index offset due to measurement uncertainty in the specimen thickness. Finally, Figure 3.27c shows the mean refractive index at each stress measurement point from Figure 3.27b plotted against stress. Assuming a constant sample thickness under loading the direct stress optics coefficient was calculated to be -1.3 $\pm$ 0.2 GPa^{-1} assuming constant thickness of the specimens in the analysis. This linear fit is shown in Figure 3.27c and also by a dashed lines in Figure 3.27a and 3.27b. Figure 3.27c also shows the direct stress optic coefficient calculated assuming variable thickness in both the fit to the Fresnel equation and instantaneous stress, as described in the previous section. The direct stress optic coefficient for PTFE was only calculated in the elastic regime, and therefore the use of Equation 3.4 for the variable thickness analysis is valid. In this case the direct stress optic coefficient was found to be 4.8 $\pm$ 0.2 GPa^{-1}. Due to the comparatively low tensile modulus of PTFE of 500 MPa, changes in thickness under load are more significant compared to YTZP.

Finally, Figure 3.27d shows results for six specimens cut with their long axis parallel to the extrusion direction of the bulk PTFE sheet. Direct stress optic coefficients of -1.7 $\pm$ 0.2 GPa^{-1} and 4.3 $\pm$ 0.1 GPa^{-1} were obtained for the constant thickness and variable thickness analyses, respectively.

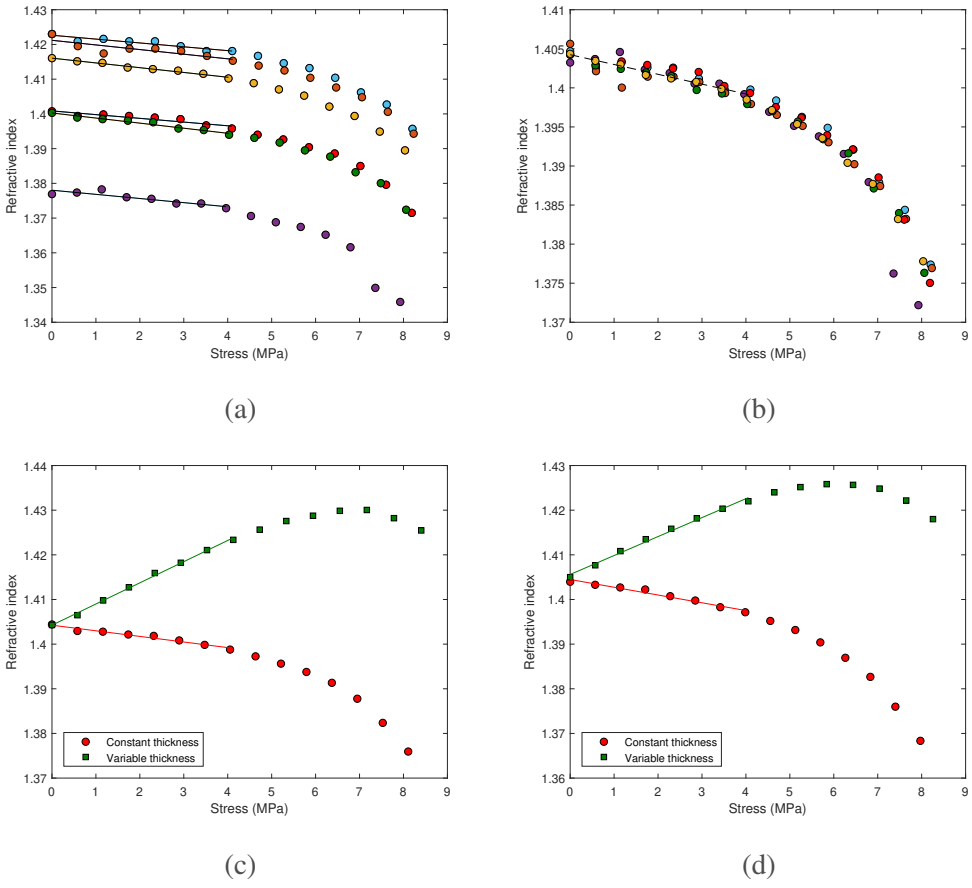

Figure 3.27: Refractive index plotted against applied stress for PTFE. (a) Repeated measurements for six samples (numbered). (b) Removal of offset in refractive index between samples due to thickness measurement uncertainty. Both (a) and (b) assume constant specimen thickness in the analysis. (c) Comparison between analyses assuming constant or variable specimen thickness. Plots (a), (b) and (c) are for specimens cut perpendicular to the bulk PTFE extrusion direction. (d) Comparison between analyses assuming constant or variable specimen thickness for specimens cut parallel to the PTFE extrusion direction.

3.3.5 Discussions

YTZP is the main focus of this Section, due to its use in high value manufacturing applications such as thermal barrier coatings and medical implants. The direct stress optic coefficient was found to be 0.13 ± 0.02 GPa^{-1} in the range 260-380 GHz and was linear for stresses up to 27 MPa. These measurements are the first demonstration of stress induced refractive index change in a ceramic at THz frequencies, and identify the feasibility of quantitative sub-surface stress measurements in structural ceramics and ceramic

coating systems in the future. In addition to two-dimensional stress distributions, depth resolved measurements might be obtained by methods such as confocal imaging or tomography [73, 74, 75].

Our interest in PTFE arose because it was the only material for which a stress optic coefficient at GHz or THz frequencies has been reported, even though the values were found to be erroneous as the strain measurements were performed based on a strain gauge glued to the PTFE samples as mentioned in the literature survey in Section 2.3. The direct stress optic coefficient was found to be linear for stresses up to $\sim$4.5 MPa, although the actual value depended on the direction of cutting the specimens from bulk material. Allowing for changes in the thickness of the PTFE specimens, i.e. true stress, our results indicate that the stress optic coefficient changes drastically once non-linear, viscoelastic deformation has taken place, as it changed sign, going from clearly positive to clearly negative. Additionally, it was clear that the effects of the change in thickness were larger than the stress-optic reaction. It has been suggested that the change in refractive index follows a cubic form for viscoelastic materials [73] and that a strain optic law should be used [76, 77], which could be explored for PTFE in future research. Future work to corroborate the stress optic coefficient PTFE reported herein should incorporate effects due to change in specimen thickness and specify specimen parameters such as extrusion direction. Clearly the manufacturing process of the material also affects the measured value.

3.4 Strain-optic coefficient measurements in reflection

3.4.1 Introduction

In this Section, it is demonstrated that APS thermal barrier coatings also exhibit stress induced birefringence for GHz illumination. The difficulty with using 2.10 for coating systems is that the in-situ Youngs modulus for the TBC must be known in order to calculate the stress from the applied load. As Young's modulus for TBC's is generally not available, the decision was taken to measure strain rather than stress, as on one hand, stress is a result of strain, and on the other hand, Young's modulus doesn't need to be known for strain measurements. For a material that exhibits stress induced birefringence,

the strain optic law relates the change in refractive index to the applied principal strain, ε_1. In a material's elastic regime, this relation is linear and is written as [68, 78, 79, 80, 81],

$$\Delta n_1 = b_1 \Delta \varepsilon_1 \tag{3.5}$$

where b_1 is the direct strain optic coefficient. Hence for the thermal barrier coatings, the strain optic coefficient is reported rather than the stress optic coefficient. If the Youngs modulus of the coating is known, the change in strain can be converted to a change in stress and a stress optic coefficient may be calculated via the stress optic law, 2.10.

The approach taken here is to measure the refractive index of the material at different loads, from which the direct strain optic coefficient is determined. Clearly, a TBC is deposited on a metal substrate that is reflective to GHz illumination which requires measurements to be made in reflection. Therefore reflection measurements were first made from bulk YTZP to confirm that the same stress optic coefficient was obtained as previously obtained in transmission. We then measured the strain optic coefficient of APS thermal barrier coatings. The experimental system to make measurements in reflection is described in Section 3.4.2, while the analysis procedure is lain out in Section 3.4.3. Results are provided in Section 3.4.4. Finally, in Section 3.4.5 we discuss how strain distributions in TBCs could be measured from variations in refractive index after manufacture, potentially leading to an approach for quality control that is not currently available.

3.4.2 Experimental Set-up

A schematic of the reflection polariscope is shown in Figure 3.28a. The source was a synthesizer and amplifier/multiplier chain (Virginia Diodes) that produced a vertically polarized, divergent electromagnetic beam, tunable between 260-400 GHz. A pair of plano-convex lenses (L) was used to focus the beam on to the specimen with a spot diameter of approximately 5 mm. A linear polariser (P) was placed in front of the specimen, oriented so that the vertically polarized component of the incident beam was allowed to pass. A Deben 2 kN dual leadscrew tensile testing rig was used to load the specimens, Figure 3.28b. Specimens were oriented at 45° to the optical axis of the source in order to reflect the incident beam into the detector. A second polariser, used as an analyser (A), was placed after the specimen, again with its polarization axis orientated vertically to produce a bright field polariscope configuration. The specimens were loaded parallel

to the polarisation axis of the illumination. Finally, second pair of plano-convex lenses focused the beam to a pyroelectric detector (D) (Gentec-eo THZ-9D).

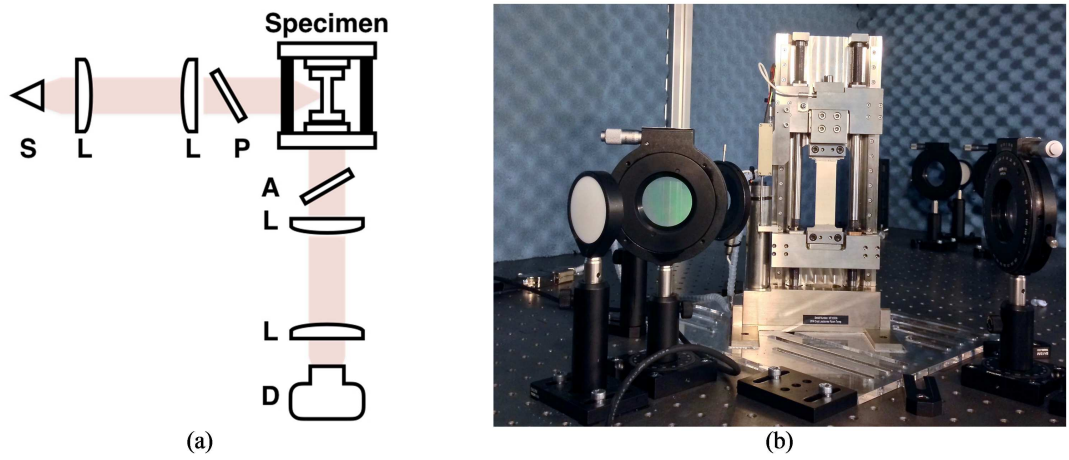

Figure 3.28: (a) Schematic of the reflection polariscope. Source (S), detector (D), plano-convex lens (L), polarizer (P) and analyser (A). (b) Deben tensile stage with dogbone specimen. The polariser (P) and the mount for the analyzer (A) can be seen on the left and right hand sides respectively of the specimen, both tilted with respect to the optical axis to reduce standing wave interference.

All the measurements were conducted in an anechoic chamber comprising of RF absorbing tiles, which can be seen in the background of Figure 3.28(b). RF absorbing tiles were also placed around the feed horn and the detector. To further reduce standing waves between the sample and focusing lenses, both the polariser and analyser were tilted to an incidence angle of 45° with respect to the optical axis, as shown in Figure 3.28(a).

The bulk YTZP ceramic samples were the same as tested previously in transmission [69]. These specimens were sintered and fired into a dogbone shape of 5 mm thickness and then ground to a thickness of 656 $\pm$ 5 μm. The YTZP had a density of 6.02 $\cdot$cm^{-3}, an average crystal size of $<$1 μm, a Youngs modulus of 210 GPa and Poissons ratio of 0.3, values supplied by the manufacturer.

The thermal barrier coatings were manufactured and supplied by Rolls Royce Plc. using the APS manufacturing process. Mild steel substrates of two thicknesses (3 mm and 1 mm) in the same dogbone shape were used. The test region of each dogbone specimen was coated on one side with yttria-stabilized zirconia (YSZ). During coating, the ends of the dogbones were covered so that the coating did not interfere with specimen

mounting. A typical specimen is shown in Figure 3 and another can be seen in the tensile test rig in Figure 3.28(b). The average coating thickness, measured using a micrometer, was 369 $\pm$ 17 μm, which is typical for the APS coating process [1, 5].

Figure 3.29: Dogbone specimen with YSZ thermal barrier coating.

3.4.3 Measruement Procedure

Before loading each sample, the tensile stage load cell was balanced by adjusting the tensile stage such that a load of 0 N was applied once the specimen had been clamped in place. The absolute load applied to each sample was then increased, and the refractive index was measured at the center of each specimen. The tensile stage maintained a constant load during each refractive index measurement.

At each load, the refractive index was measured by tuning the source frequency between 260-380 GHz in 0.25 GHz steps, and measuring the reflected power at each frequency. Variations in the source emission and detector response were normalized by recording the frequency spectrum from a plane aluminium dogbone with no coating, i.e. a mirror, placed in the tensile test rig prior to testing each specimen. Typical normalised spectra in reflection are shown in Figure 3.30 for bulk YTZP and for a YSZ thermal barrier coating. The bulk YTZP specimens were thicker than the TBC and hence more cycles in the intensity variation are seen.

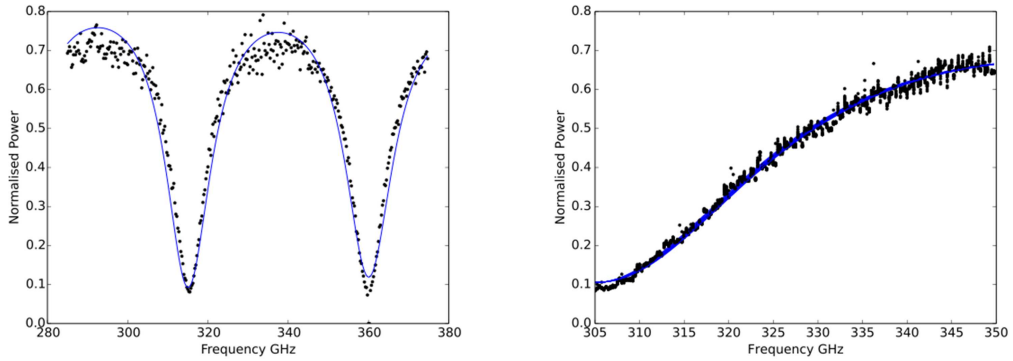

Figure 3.30: Normalised frequency spectrum for (a) bulk YTZP specimen and (b) a YSZ thermal barrier coated specimen loaded at 50 N. The black dots indicate the experimentally measured normalised power and the blue line is the fit of the Fresnel equation appropriate for each case.

The shape of these spectra are described by the Fresnel equations for non-normal incidence of a single slab dielectric [69, 72, 71]. The reflection coefficient for a single slab dielectric, surrounded by air ($n_{air} = 1$), at non-normal incidence is,

$$R = \frac{\rho_1 + \rho_2 e^{-2iL}}{1 + \rho_1 \rho_2 e^{-2iL}} \tag{3.6}$$

where ρ_1, ρ_2 are the Fresnel coefficients and L is the phase thickness. The phase thickness is defined to be,

$$L = \frac{2\pi\tilde{n}(t_0 + t)}{\lambda} \tag{3.7}$$

where t_0 is the actual sample thickness, $\tilde{n}$ is the complex refractive index and,

$$t = t_0 \frac{1 - cos\Theta'}{cos\Theta'} \tag{3.8}$$

is a thickness correction factor that depends on the refraction angle of the beam inside the material. The refraction angle is calculated using Snell's law,

$$\Theta' = sin^{-1}(\frac{n_{air}}{\tilde{n}} sin\Theta) \tag{3.9}$$

The first Fresnel reflection coefficient for a transverse electric (TE) incident beam as used in our experimental arrangement is,

$$\rho_1 = \frac{cos\Theta - \sqrt{(\tilde{n}/n_{air})^2 - sin^2\Theta}}{cos\Theta + \sqrt{(\tilde{n}/n_{air})^2 - sin^2\Theta}} \tag{3.10}$$

The second Fresnel reflection coefficient depends on whether the material is a dielectric slab in air as for the bulk YTZP samples, Figure 3.31(a), or a dielectric coating on a reflective surface as for the YSZ coating samples, Figure 3.31(b). For the single slab dielectric, bulk material,

$$\rho_2 = \frac{cos\Theta' - \sqrt{(n_{air}/\tilde{n})^2 - sin^2\Theta'}}{cos\Theta + \sqrt{(n_{air}/\tilde{n})^2 - sin^2\Theta'}} \tag{3.11}$$

For the dielectric coating applied to a substrate the Fresnel coefficients are adjusted so that,

$$\begin{aligned} \rho_2 = \tau_1 = \rho_1 + 1 \\ \tau_2 = 0 \end{aligned} \tag{3.12}$$

where τ_1 and τ_2 are the Fresnel transmission coefficients.

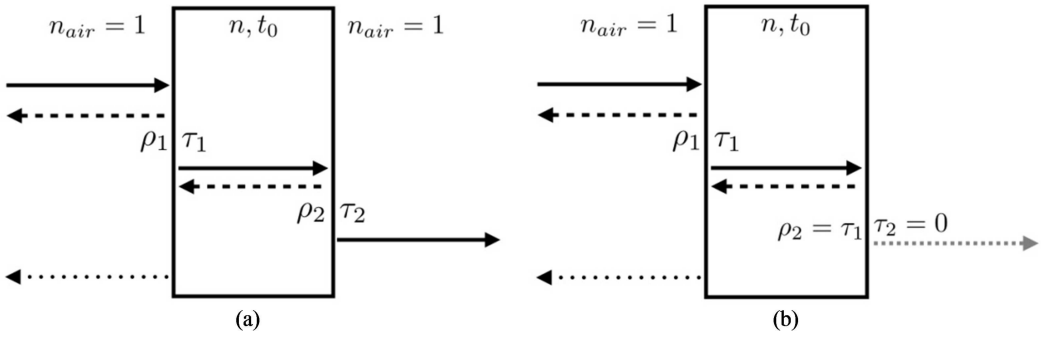

Figure 3.31: (a) Single slab dielectric and standard Fresnel coefficients for bulk material. (b) Single slab dielectric with revised Fresnel coefficients for a coating on a reflective surface.

The refractive index of the material was calculated from each normalized frequency spectrum by conducting a non-linear least squares fit to the measured frequency spectra, Figure 3.30. Both the refractive index $\tilde{n}$ and the reflection coefficient R [Equation 3.6], are complex quantities for a material with appreciable absorption such as ceramic. Hence the power measured by the detector was fitted to R multiplied by its complex conjugate, which results in a real value. The thickness of each specimen was estimated from the measured 0 N frequency spectrum, by performing a non-linear least squares fit to the Fresnel equation and allowing both the refractive index and the thickness to vary, using the thickness measured with the micrometer as an initial estimate. The thickness determined from the fit to the specimen at 0 N was then used in the fits to subsequent spectra obtained at increased loads. In those subsequent fits, only the refractive index was allowed to vary.

3.4.4 Results

Results for the bulk YTZP and APS thermal barrier coatings are described in the following two Sections.

Bulk YTZP Ceramic

Three individual samples were tested, three times each. Each specimen was loaded between 0 and 600 N, in increments of 50 N and the refractive index, $\tilde{n}$, at each load measured as described above. The refractive index as a function of applied stress is shown in Figure 3.32a. Stress was calculated by dividing the applied load by the unloaded cross-sectional area of each specimen.

Excellent repeatability was achieved for each specimen, although there is an offset in the refractive index between each sample. This offset between samples was also observed in our previous transmission experiments. A sensitivity analysis showed it was due to uncertainty in the measured thickness of each specimen rather than differences in the manufactured material such as density, residual stress or grinding [69]. Furthermore, it is the change in refractive index with applied load that is important when calculating the stress optic coefficient. Hence to remove the offset, the mean of all measurements for all specimens at a given stress was calculated, shown by the dashed line in Figure 3.32a. A constant offset was then applied to each data set for each specimen, based on a least-squares minimisation to the mean of all specimens, as described in [69]. In this way, the refractive index offset due to measurement uncertainty in the specimen thickness was removed without affecting the gradient measured for a given experiment, Figure 3.32b. The same data is repeated in Figure 3.32c with an expanded vertical scale. The points show the mean refractive index at each stress value from Figure 3.32b. Assuming a constant sample thickness under loading, i.e. the engineering stress, the direct stress optic coefficient was calculated from a least-squares linear fit, and is shown in Table 3.3.

Figure 3.32c and Table 3.3 also show the stress optic coefficient calculated using the reduction in cross-section under load, i.e. true stress. In this case, both the thickness at each load used in the fit to the Fresnel reflection equation, and the cross-sectional area used in calculating stress from the applied load, were adjusted using Poissons ratio for

the bulk YTZP material. Due to the high Youngs modulus of YTZP, there is only a small difference between the two values.

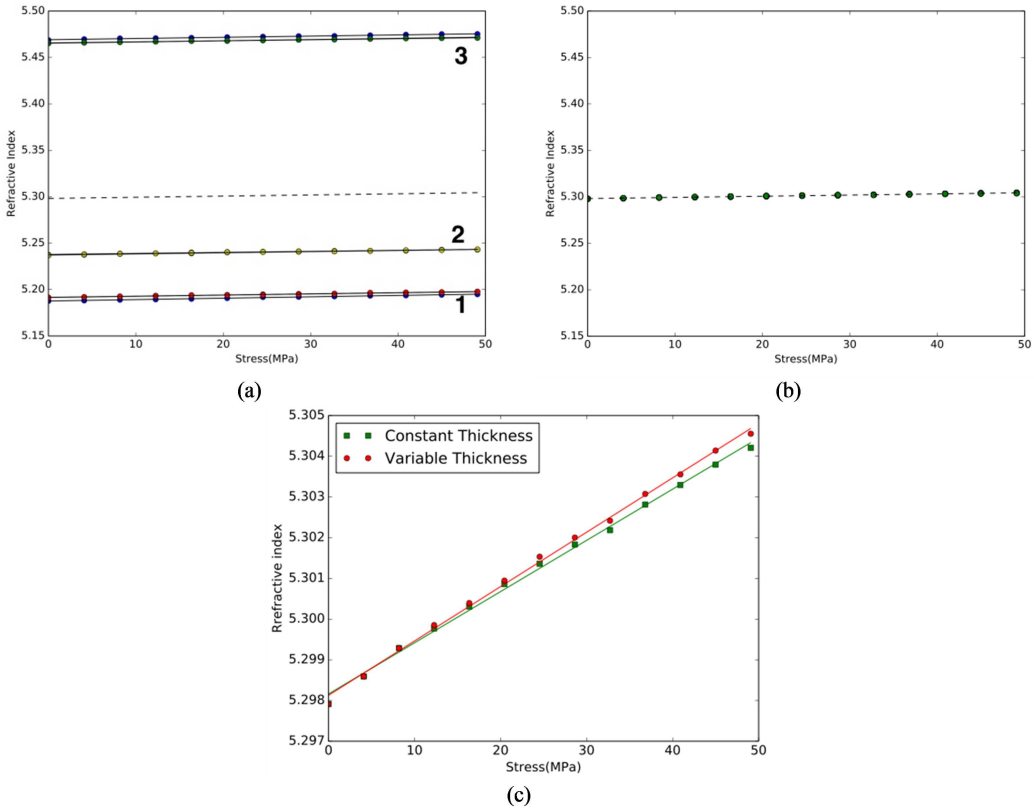

Figure 3.32: (a) Measured refractive index versus applied stress for bulk YTZP (b) Offset corrected refractive index versus applied stress. (c) Stress optic coefficients for bulk YTZP using constant and variable sample thickness in the analysis.

Table 3.3: Comparison of stress optic coefficient values for YTZP.

	Direct stress optic coefficient (GPa^{-1})	
	Constant thickness	Variable thickness
Reflection	0.13 ± 0.01	0.14 ± 0.01
Transmission [69]	0.13 ± 0.02	0.14 ± 0.02

Table 3.3 includes the direct stress optic coefficient previously calculated for YTZP in transmission, also for constant and variable thickness. There is excellent agreement between the two methods. Having validated the reflection polariscope methodology, the measurements were extended to APS coatings.

Two samples of each substrate type were tested three times each. Each sample was loaded between 0 and 1200 N in 100 N steps, while a frequency sweep of the GHz source was recorded at each load increment. Figure 3.33a and 3.33b show the measured refractive index as a function of applied strain obtained by the non-linear least squares fit to Equation 3.6 from the frequency sweep at each load, for the thick and thin substrates. The applied load was similar for both substrates and hence the applied strain range for the thick substrate is smaller, Figure 3.33a. It is worth emphasizing that the coating thickness on each substrate thickness was the same.

The measured refractive index was plotted against strain, rather than stress, because it is not straightforward to calculate stress in the APS coating. Firstly, the load was not applied directly to the coating, but was transferred via strain in the substrate through the bond coat. Secondly, Youngs modulus for a TBC varies significantly from that of bulk zirconia ($\sim$200 GPa) and depends on its chemical composition, the substrate material and the manufacturing process. It is clear that the TBC carries a significantly smaller proportion of the total load than the substrate, because it is thinner and a typical Youngs modulus of a TBC ($\sim$50 GPa) is significantly smaller than that of mild steel (210 GPa). Calculating the strain in the substrate alone, ignoring the small reinforcement from the TBC, results in an overestimate of the strain in the TBC of only $\sim$2% and $\sim$6% for the thick and thin substrates, respectively. Hence the strain in the TBC was assumed to be equal to the strain in the substrate, which was calculated by dividing the applied load by the unloaded cross-sectional area and Youngs modulus of the substrate. This small overestimate of strain results in a lower bound for the calculated strain optic coefficient.

The measured refractive index, as a function of applied strain for the TBCs is shown in Figures 3.33a and 3.33b. Again there is excellent repeatability between experiments on a given specimen but an offset in the refractive index between each sample. This offset between samples was most noticeable for the TBC deposited on the thin substrate, although with only two specimens per substrate thickness, it is not possible to draw a general conclusion from this observation. The dashed lines in Figures 3.33a and 3.33b represent the mean of all measurements for all specimens at a given strain. The constant offset in refractive index was removed by the procedure described in the previous section,

resulting in the scatter plots shown in Figures 3.33c and 3.33d. A linear least-square fit was applied to each sample in Figures 3.33a and 3.33b to obtain the direct strain optic coefficients (dimensionless) of (-0.013 $\pm$ 0.010) $\times$ 10^{-9} and (-0.019 $\pm$ 0.004) $\times$ 10^{-9} for the thick and thin substrates, respectively. The measured strain optic coefficient may be converted to the stress optic coefficient if the Youngs modulus of the TBC is known.

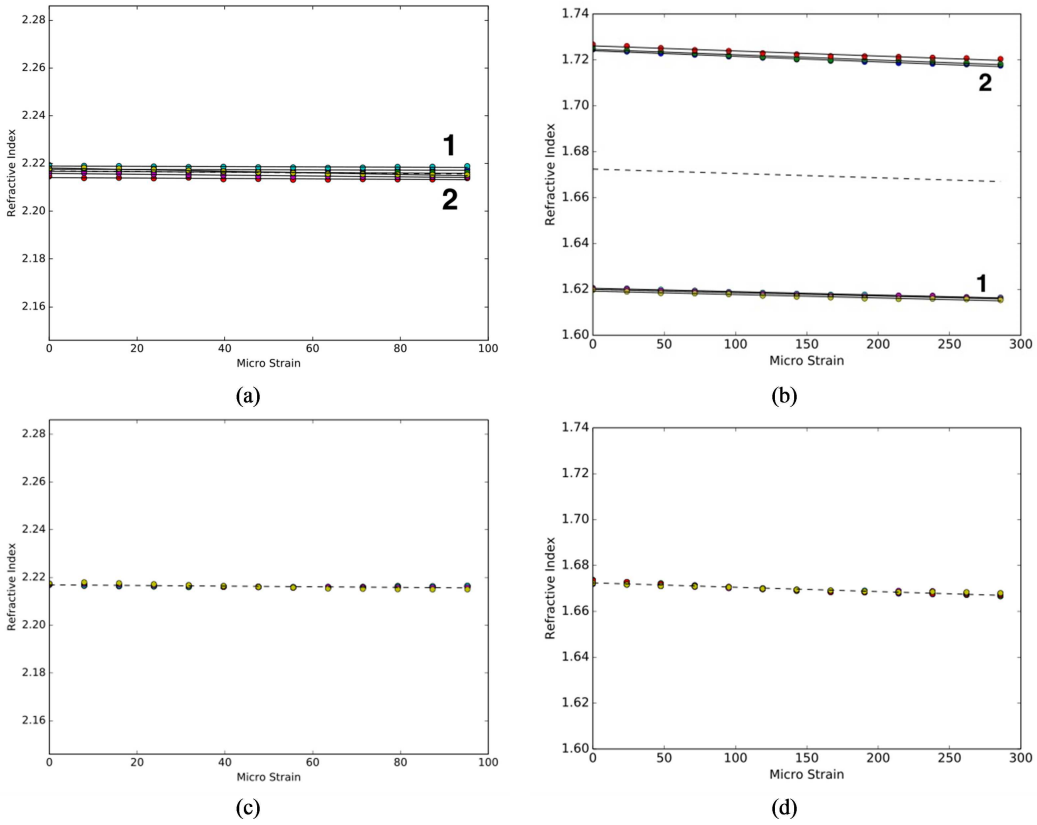

Figure 3.33: Measured refractive index versus applied strain for YSZ TBCs. (a) Thick substrate (2 mm) and (b) thin substrate (1 mm). Offset corrected refractive index versus applied strain for (c) thick and (d) thin substrate specimens. The coating thickness is the same for each specimen. The different substrate thicknesses are treated separately due to the difference in thermal history during and after coating, which affects the coating properties.

In order to visualise more clearly the strain optic coefficient measured for the thick and thin substrates, Figure 3.34 shows the mean refractive index at each applied strain from Figures 3.33c and 3.33d, with an expanded vertical scale. The maximum refractive index at zero strain for both specimen thicknesses has been normalized to unity, in order to remove the offset in the refractive index between the samples with thick and thin substrates. The change in refractive index with applied strain, i.e. the direct strain optic

coefficient calculated above is shown by the straight line in each case, with appropriate scaling to the normalized refractive index. The strain response of the APS coatings on both substrate thicknesses is very similar.

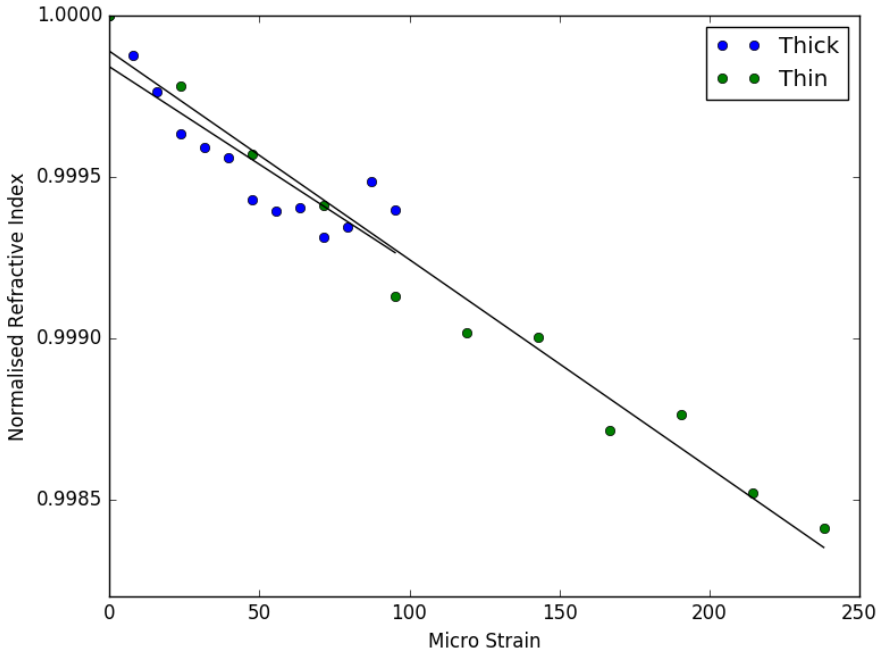

Figure 3.34: A comparison of the stress optic coefficient for APS YSZ measured on thick and thin substrates. The data presented in this figure is the same as in Figures 3.33(c) for the blue points and (d) for the green ones. The data has been normalised in order to allow a direct comparison between the 2 types of smaple.

3.4.5 Discussions

The refractive index measured for the YSZ coatings, Figure 3.34, was subject to more variation than the bulk YTZP, Figure 3.32. The main reason for this is the relatively rough surface of the APS coating and the bond coat interface, of the order of ± 25 μm, compared to the ground surface of the bulk YTZP. Similarly the internal structure of the APS coating is less homogeneous than the bulk YTZP. The associated increase in scatter of the reflected beam in the TBC introduces noise into the measured reflected power and hence the accuracy of the non-linear least squares fit.

As discussed above, the relatively small difference in refractive index between specimens of the same type was attributed to uncertainty in the measured thickness. However, a much more significant difference in refractive index was observed between the YSZ

coatings (of the same nominal thickness) deposited on the thick and thin substrates, Figures 3.33a and 3.33b. The APS coatings were applied to the dogbone substrates at exactly the same time, so the variation in coating thickness between specimens was minimal. It indicates that the refractive index depends on the manufacturing process, in particular the thermal history of coating application and cooling which is different between the thick and thin substrates. However, the strain optic coefficient measured in each case was very similar, as emphasized by Figure 3.34.

Another interesting feature of testing the YSZ coatings was a systematic reduction in the measured refractive index with each loading cycle. Figures 3.33a and 3.33b show three repeated tests for each of the two specimens. Within each grouping of three measurements, the small offset in refractive index decreased from the first to third loading, although the strain optic coefficient remained the same. This apparent systematic change in refractive index with load cycle, and possibly thermal cycles, could be due to a structural change that might be related to ageing but clearly requires further investigation.

The results presented open the way for sub-surface strain measurements in structural ceramics and ceramic coating systems using GHz illumination. We are currently using the techniques described in this paper to investigate how variations in refractive index are related to intrinsic material properties, manufacturing process parameters and ageing effects. We are particularly interested in attempting to quantify the strain distributions in the TBC that lead to failure, for which the direct strain optic coefficient determined in this paper is the starting point. It is possible that strain distributions cannot be quantified by this approach, perhaps because the effect of strain on the refractive index cannot be isolated from local variations in coating thickness and thermal history during the manufacturing process. If that turns out to be the case, we have already begun to observe qualitative variations after manufacture that can be related to time to failure in accelerated ageing trials of TBCs. Ultimately, either a quantitative correlation between the in-situ strain after manufacture and the expected remaining lifetime of the TBC, or an empirically determined birefringence distribution that is characteristic of TBCs that will fail quickest, would enable sub-optimal components to be discarded before they are put into service and address a major challenge to TBC development [3].

Further to the discussion of the results in Section 3.4.4, following is the presentation of an improved fitting approach that was developed after the data was published as well

as an analysis of the effects that residual thermal bending within the samples had on the results.

3.4.6 Improved Data Fitting

While the fitting approach presented in Section 3.4.3 provided fits that looked fairly good for the data, the actual values for the thicknesses and refractive indexes that came out of it were deemed fairly far off the true values. The thicknesses that went into the fits in the end were typically of the order of twice the measured thickness (while the double path due to reflection was taken into account as well), while the refractive indexes of $\sim$2.2 and $\sim$1.7 for the thick and thin samples respectively are unusually low considering that the refractive index of the ceramic itself is of the order of $\sim$5.7, while later measurements on coated samples using time-domain spectroscopy (TDS) have found typical indices of the order of $\sim$3.3. This reduction with respect to the bulk material for an APS coating can be explained by the porosity of the material as well as the micro cracks that tend to form within to release local strain pockets. Those elements will be filled with air with a refractive index of 1, and at THz wavelengths the pores and micro cracks will be averaged with the surrounding medium leading to an effective index between that of the material and air. The same applies to EB-PVD coatings, as micro cracks are present all the same for that coating structure, the porosity is replaced by the inter-columnar space in the structure.

Additionally, even with a dielectric-metal interface, there will be transmission into the metal, although it will be absorbed within the its skin depth. In order to improve the results, the fit was refined to a 3 layer system, with the first layer being air, the second layer the ceramic top coat and the third layer being the metal substrate. Finally, a surface roughness layer for the air-ceramic interface was added to further improve the fit. There was no inclusion of the bond coat layer, and the thermally grown oxide that will form at the bond coat-ceramic interface was assumed to not have started appearing as the samples haven't gone through any ageing cycles. For the new fits ρ_2 was calculated according to Equation 3.11 and τ_2 was calculated from ρ_2 in the same fashion as τ_1 is calculated from ρ_1 in Equation 3.12. In order to calculate the surface roughness, effects on ρ_1 and τ_1, ρ_1 was multiplied by a roughness term as follows,

$$\rho_1 = \rho_1 e^{-\left(\frac{2\pi Z \tilde{n}}{\lambda}\right)^2} \tag{3.13}$$

where Z is the root mean square roughness, ñ is the complex refractive index for the ceramic layer and λ is the wavelength of the incoming radiation.

One big unknown for the new fitting approach was getting a refractive index for the metal. As steel is largely made from iron, the refractive index of iron at the edge of the near infrared, $3.17 + 6.12i$, was taken as a starting value to check the validity of the method. Using time-domain spectroscopy measurements of the samples, a refractive index for the unstressed coatings was determined. This was used to fix down the properties of 2 of the 3 layers and was followed by a fit of the real and imaginary parts of the refractive index of the metal layer. Once an optimal value was found for a given sample, it was fixed and the coating properties were turned back into the unknowns fitted for. Figure 3.35 below shows a comparison between the old fitting (Figure 3.35a) and the new fitting (Figure 3.35b). In both cases, the fits look reasonably good, with the main difference in this case being at the top end, where the new fit does follow the general shape of the data a little better. The coefficient of determination for the two fits was calculated at 0.993 for the old approach and 0.997 for the new one. Both are good fits, with the new one performing marginally better. Most importantly though, the refractive index values and thicknesses out of the new fit are in line with what is expected from the TDS measurements.

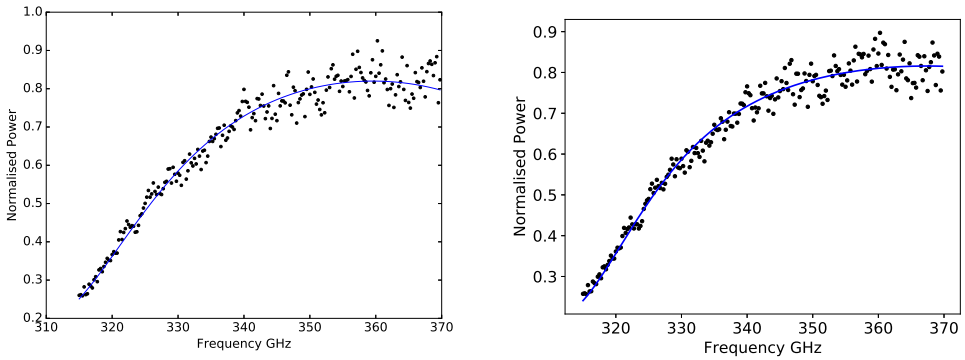

(a) (b)

Figure 3.35: Comparison between (a) the old fitting approach (Section 3.4.3) and (b) the new fitting approach. The coefficients of determination for have been calculated to be 0.993 for (a) and 0.997 for (b).

Given the correlation between the results from the new fits and the expected values, they were deemed as working in a satisfactory manner and the data presented in Section

3.4.4 was refitted to see what impact this would have on the slopes for the different samples. Figure 3.36 contains the results for the refits of the data presented in Figure 3.33. It was notable that (analogously to the data presented in Section 3.4.4) the scatter in the gradients between runs for the thick substrate, as seen in Figure 3.36a, is a lot larger than that for the thin substrates, Figure 3.36b. Taking a closer look at the different refractive index curves, it became clear that there was 2 regimes within the data of the different measurements, with the transition between them at $\sim$80 μs, which is very clearly visible in the averaged curve, Figure 3.36c. The thin samples showed slight changes after a strain value of $\sim$160 μs, which corresponds to the same applied load of 700 N, but the differences before and after are a lot less stark. 3 different fits have been applied to the thick substrates, the first over the whole range on strains, the second goes up to 700 N, while the last fits the data above 700 N. The values for the slopes are (-1.3 $\pm$ 1.2) $\times$ $10^{-5}\mu s^{-1}$, (-2.5 $\pm$ 1.0) $\times$ $10^{-5}\mu s^{-1}$ and (0.9 $\pm$ 1.4) $\times$ $10^{-5}\mu s^{-1}$ respectively. Comparing these values to the one obtained from the linear fit for the thin substrate, (-2.5 $\pm$ 0.7) $\times$ $10^{-5}\mu s^{-1}$, the two sets behave very similarly over the first 700 N of applied load and after that point the noise within the measurements in the thick substrates increases dramatically. This indicates that assuming a single strain-optic coefficient for a coated sample is likely not appropriate, as there are likely different regimes of strain response with each having its own coefficient.

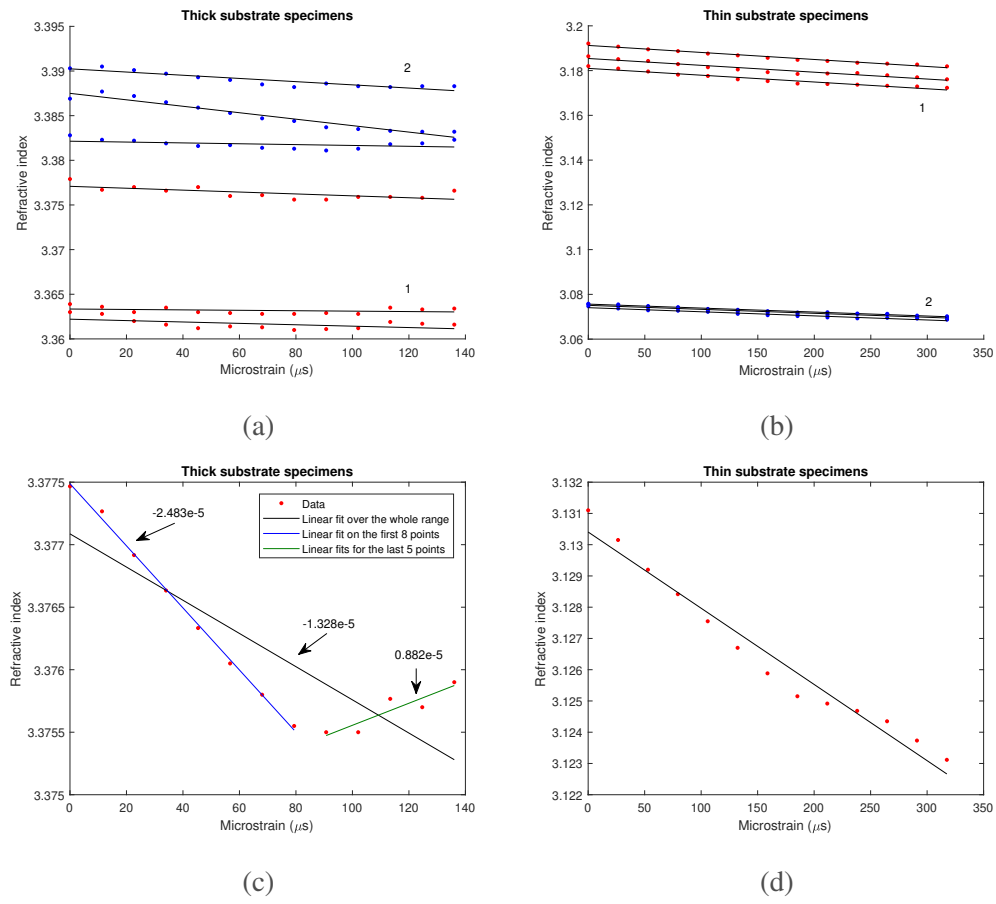

Figure 3.36: Refitted refractive index versus applied strain for YSZ TBCs. (a) Thick substrate (2 mm) and (b) thin substrate (1 mm). Averaged refractive index versus applied strain for (c) thick and (d) thin substrate specimens.

One possible reason for this behaviour was that up to 700 N, the strain was mainly affecting the pores within the coating, opening them up and thus leading to a reduction in average refractive index. After that point, the ceramic itself started being affected by the strain, at which point its own strain-optic properties started taking a clear effect and its thickness would be more affected as well. As no change in thickness was accounted for for the coated systems any notable thickness reductions were going to increase the measured refractive index value. On top of this, the ceramic itself showed a positive strain-optic coefficient of $2.6 \times 10^{-5} \mu s^{-1}$ (converted from the measured stress-optic coefficient using Young's modulus), which means as it is stressed, its refractive index increases. The second section in Figure 3.36c likely shows a combination of those two factors with further opening of the pores and micro cracking within the coating.

The thin substrates were less affected, but also exhibited a lower starting refractive

index, which likely meant that their porosity was higher than that of the thick substrates, which in turn is a potential by-product of the differences in terms of thermal history between the two sets, as the deposition happens at a temperature of typically around 1100 °C, after which a sample on a thinner substrate will cool down faster than one on a thicker one, as the ability to store heat is dependent on both material and volume. The increased porosity for the thin substrate would mean that the point at which the ceramic starts taking on enough of the strain to make a difference was happening at higher loads, hence it wasn't seen within our data, Figure 3.36d.

3.4.7 Curvature Effects

One effect to consider when pulling specimens and measuring stresses and strains is the impact of any curvature present in the samples. Both of the TBC deposition approaches (APS and EB-PVD) are performed at temperatures around 1100 °C. Hence the substrate will get heated up to those temperatures during deposition and the system will be left to cool to room temperature afterwards. This thermal history is likely to leave residual strains which can show in the form of a curvature.

In order to assess the residual curvature of our samples, they were imaged under a confocal microscope to measure their surface profiles on both the back and the front surfaces. The degree of curvature was determined by fitting a circle to the surface profile of the back of the samples, and extracting the radius from the fit. The analysis approach was developed on a test specimen with a clear curvature and then applied to the APS samples presented above as well as a set of EB-PVD samples, which will be discussed further in Section 5.4.5. One of the reasons why the analysis was extended to the EB-PVD samples was that they constitute the majority of the future samples used for the project, and thus it was obviously important to know whether curvature were going to be an issue or not.

The amount of curvature present on the investigated surface was measured using a confocal microscope. Figures 3.37 show the process of fitting for the radius of curvature for the samples. First a cubic fit was applied to the data, Figure 3.37a, and its start and end points were used to correct any tilt in the measurement, leading to Figure 3.37b. After the profile was straightened out, a circle was fitted to it in order to extract the radius of

curvature, which could be used to assess the intrinsic bending strain. Finally the strain released through changing the bend by appropriate values for different applied loads was estimated through calculating the difference in inherent strain for the original data (green circle on Figure 3.37b) and the stressed case (blue circle on Figure 3.37b). The strain differences inferred from those calculations could then be used as correction factors to the strain values used for the strain optic coefficient calculations (e.g. Figure 3.33) if found to be significant.

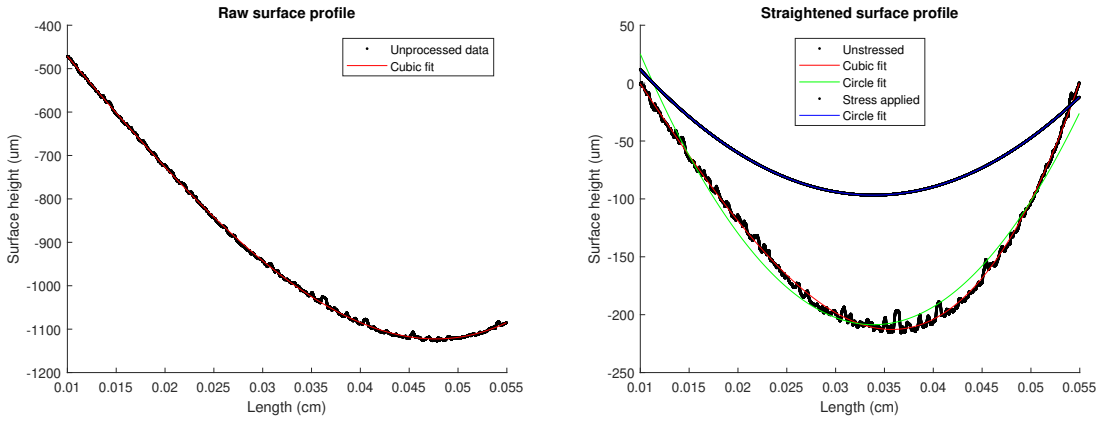

(a) (b)

Figure 3.37: Illustration of the curvature fitting process.

Once a radius of curvature was fitted, the bending strain present within the substrate was estimated. In order to calculate the bending stress, the bending moment of the sample was calculated using [82],

$$M = \frac{E * I}{R_c} \tag{3.14}$$

where M is the bending moment, E is the material's Young's modulus, I is the area moment of inertia, and R_c is the radius of curvature. The bending moment can then be used to calculate the stress, σ, and strain, ε, within the sample according to,

$$\sigma = \frac{M * y}{I} \tag{3.15}$$

and

$$\varepsilon = \frac{\sigma}{E} \tag{3.16}$$

where y is the distance from the neutral stress axis within the sample to the point where the stress is calculated, which in this case was taken as the edge of the sample as the maximum impact of the bending strains was the point of interest. While the above Equations

3.14 and 3.15 are reasonable approximations if the coating's effect was negligible, the typical coating thicknesses were large enough that the system needed to be looked at as a composite system made from 2 materials with different thicknesses and Young's moduli. Therefore after the simple bending correction was implemented, a second, more robust model was added for comparison.

For the complex bending correction, the equations for the bending moment and corresponding stress at the surface were modified as follows:

$$M = \frac{E_c * I_c + E_s * I_s}{R_c} \tag{3.17}$$

$$\sigma = \frac{M * Y_c * E_c}{E_c * I_c + E_s * I_s} \tag{3.18}$$

$$\sigma = \frac{M * Y_s * E_s}{E_c * I_c + E_s * I_s} \tag{3.19}$$

where all symbols are as previously defined. Y_s and Y_c are the distances from the neutral axis to the respective surface. In order to calculate them, the location of the neutral axis needs to be known. This can be calculated using the following 2 relations:

$$\frac{y_c}{y_s} = -\frac{A_s * E_s}{E_c * A_c} \tag{3.20}$$

$$y_c - y_s = \frac{t_c}{2} + \frac{t_s}{2} \tag{3.21}$$

where y_c and y_s are the distances from the coating and substrate centres of mass to the neutral axis, A_s and A_c are the cross sectional areas along the bend axis of the coating and substrate and t_c and t_s are the thicknesses of the coating and substrate respectively. These equations allow the neutral axis to be located and, from there, the distance to each of the surfaces, Y_c and Y_s, to be calculated. In order to get an idea of the released bending strains, the amount of straightening which took place within the sample had to be measured. For this purpose, a DIC system by LaVision was used. DIC is a technique where subsequent images are compared to an initial reference and determining the motion of imaged features from one image to the next by find peaks in the auto-correlation or cross-correlation between subsets of the images [83]. Due to the nature of our samples, it was necessary to add a speckle pattern onto them to generate the features that could be correlated to between the images. They were produced by flicking black acrylic polyurethane primer at

the sample with a toothbrush and an example of the resultant speckle pattern can be seen in Figure 3.38.

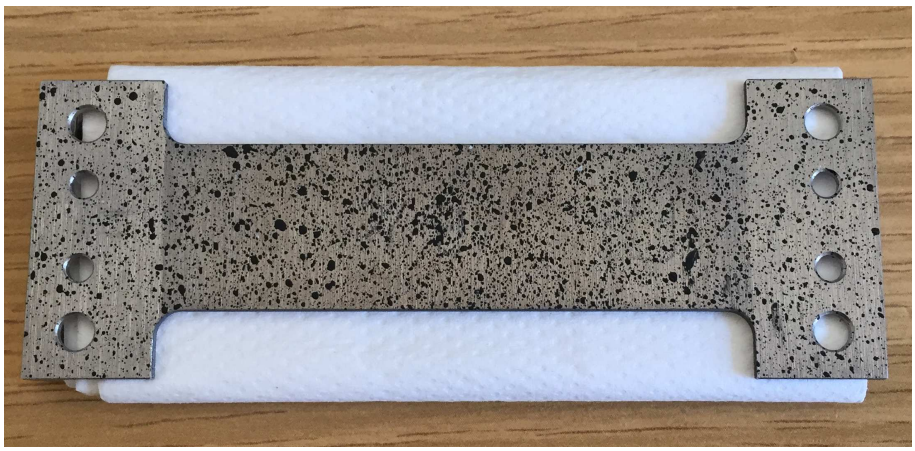

Figure 3.38: Example of the speckle pattern on the back of a sample for the DIC measurements.

Two pieces of information were extracted from the DIC measurements, first was the strain in the direction of the tension and second was the out of plane motion of the sample. The measured strains were used as a standard to compare to the strains obtained from the applied load and substrate cross-sectional area with and without bending corrections added. If the bending corrections improved the match between measured and calculated strains, then the approach with which they were calculated was appropriate. The out of plane motion of the samples was used as a measure of the straightening. The DIC system generated an image of z shifts with values over the visible area of the speckle pattern where the correlation converged. One such image for a sample under substantial load is shown in Figure 3.39 below.

In order to get a single value for the change in curvature, an average line along the tension (y) over a small range of x values was taken. This average had any tilt and offset corrected in the same way as the curvature measurements shown in Figure 3.37. A 3rd order polynomial was fitted to the data, and the line connecting the first and last points was used as tilt and offset correction for the data. Once the data was straightened out in this manner, the extremum of the resultant line was taken as the change in radius of curvature for the sample. Figure 3.40 shows these steps. The change in radius was calculated using that approach for a range of loads, and then interpolated as it was found that in general the change is linear, as one would expect with a linear increase in applied load.

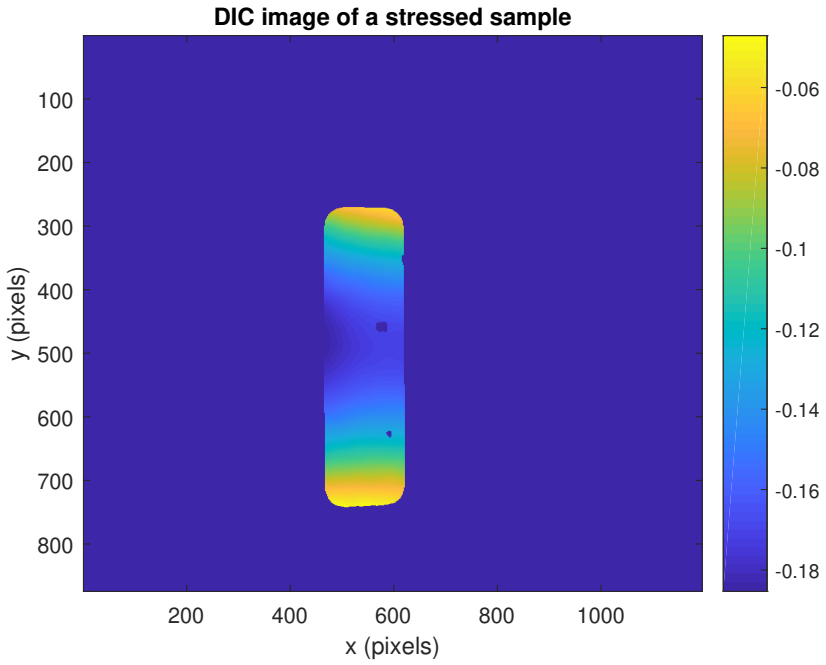

Figure 3.39: z motion map produced by the DIC system. The scale of the colourbar is mm.

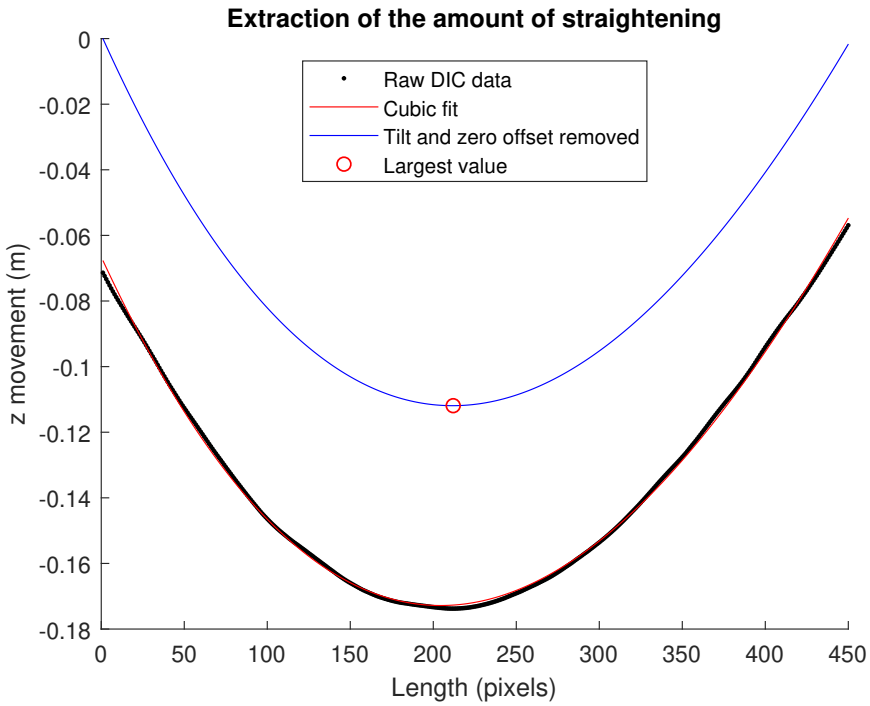

Figure 3.40: Extraction of the change in radius of curvature from the DIC measurements. The raw data (black dots) is fitted with a cubic function (red curve), which is to remove any offset and tilt (blue curve). Finally the extremum of the resultant curve is taken as the amount of change in radius of curvature for the given load.

The change in radius of curvature was then used to calculate bending corrections following both the simple and complex approaches, and the strain curves obtained in that manner were compared to the measured strains. The expectation was that with the corrections, the values should be closer to the measured strains than the calculated ones. Figure 3.41 contains the results for the test specimen. It was clear that both the calculated strains with and without simple bending correction were one as bad as the other, while the composite beam bending correction yielded results which were much closer to the strains that were measured. Thus, if a bending correction was needed, it was generally advised to use the composite beam bending approach.

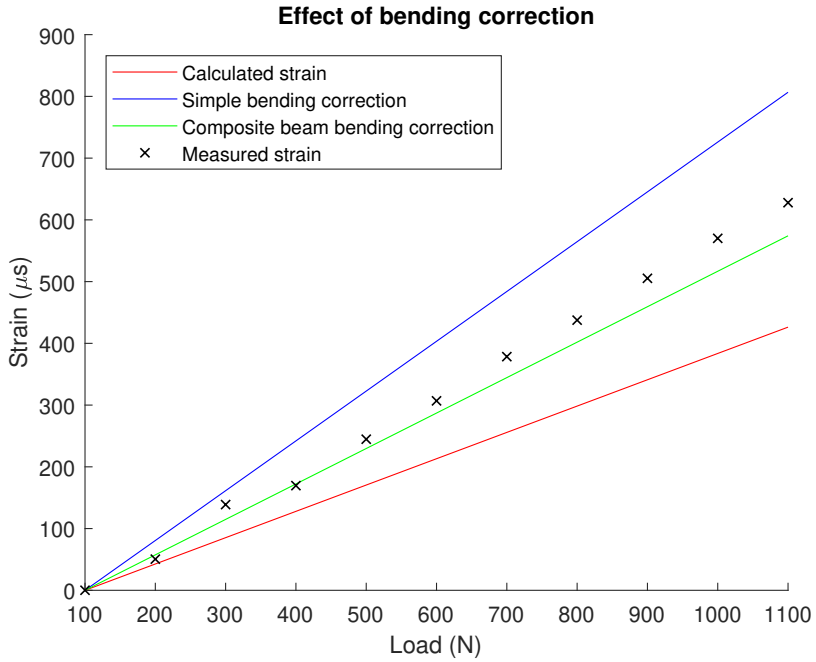

Figure 3.41: Measured strains against calculated strains, where the red curve is the strain calculated by ignoring the coating presence and using substrate thickness and applied load, the blue curve applies a bending correction to those strains still assuming the coating effects negligible, while the green curve adds the effects of the coating into a composite beam bending model.

After the method was shown to work to a reasonable extent, the APS samples on steel substrate used in the measurements presented in this Section. After looking at the inherent curvature, it was found that the maximal bending strain values ranged from 3.66 μs to 30.78 μs for those samples. Compared to the total applied strains ($\sim$150 μs for the thick samples and $\sim$300 μs for the thin ones), these values were fairly small, additionally, the straightening of the samples would happen gradually as the loads increase, which would

lead to a small uncertainty on the strain axis, however, it could safely be neglected as its impact on the slope of the measurements was small compared to the differences between runs and samples.

In summary, the curvature effects were negligible for the samples on a mild steel substrate. The effect of the curvature on the EB-PVD samples was again found to be negligible, however, this time it wasn't due to the small degree of bending in the samples, but rather due to how that coating structure reacted to applied strains. This will be discussed further in Section 5.4.5.

3.5 Conclusions

In this Chapter, the first measurements of the strain-optic response of YTZP ceramics as well as YSZ coatings on metal substrates have been presented. The measurements were performed in the GHz range between 260 and 400 GHz, and followed an investigation of the source's and pyroelectric detector's performance. In transmission, the YTZP ceramic was found to have a stress-optic coefficient of 0.13 ± 0.02 GPa^{-1} while in reflection, the same samples' coefficient was measured as 0.13 ± 0.01 GPa^{-1}. As transmission and reflection results were in close agreement, the technique was applied to YSZ coatings on metal substrates. While results for these samples were published [69], they were found to be flawed, as after further investigation of the coatings inconsistencies between the physical thicknesses of the samples and those fitted during the analysis were noted, which were caused by over simplification of the system in the algorithms. In order to improve on those results, the fitting approach was modified to incorporate a properly modelled metallic back surface at which point the data was analysed again. That time the thicknesses as well as refractive index values agreed with micrometre measurements for the former and time-domain spectroscopy measurements for the latter. The re-fitted data yielded strain-optic coefficients for the coatings of $(-2.5 \pm 1.0) \times 10^{-5} \mu s^{-1}$ and $(-2.4 \pm 0.7) \times 10^{-5} \mu s^{-1}$ for the thick and thin substrates respectively. Finally, some investigation of the effects of residual bending within the samples caused by the coating deposition on the measured coefficients was performed. In this instance, most of the tested samples had sufficiently small degrees of bending that the any correction was not going to have a noticeable impact on the final strain-optic coefficient.

Following the strain-optic measurements, the GHz system was modified to measure stress distributions in 2D, which will be looked at in the next Chapter.

Chapter 4

GHz Confocal Imaging

4.1 Introduction

After finding that the stress-optic effects for PTFE and YTZP were measurable within the GHz spectrum of our source (260 GHz - 380 GHz), a confocal imaging system was set-up in order to assess the imaging capabilities at those frequencies and if a strain image could be generated. In this chapter, the confocal system and an assessment of its spatial resolution are presented, followed by stress imaging tests carried out on PTFE cantilevers. The aim of the experiments was on one hand to assess the limits of the GHz system but on the other hand also to test the feasibility of the confocal imaging approach for stress imaging with the option of it being later applied on a system operating at frequencies between 0.8 and 2.2 THz.

4.2 Confocal System Characterisation

4.2.1 Introduction

The motivation for using a confocal imaging system is an expected improvement in the axial resolution in order to help with 3D and sub-surface imaging [84]. For a confocal system, the limits to the lateral and axial resolutions can be expressed as [84]

$$\Delta_{lateral} = 0.88 \frac{\lambda}{n}(f/\#) \tag{4.1}$$

and

$$\Delta_{axial} = 6 \frac{\lambda}{n}(f/\#)^2 \tag{4.2}$$

where λ is the wavelength, n the refractive index at the tested object and $f/\#$ is the f-number of the f-number of the optical element providing the focus. For the system presented in this section, the lateral resolution limit is 1.58 mm and the axial resolution is at 10.92 mm.

After the system was aligned, a set of measurements with the confocal aperture and one without it were taken and used to compare spot sizes for the axial resolution. The in-plane resolution of the system was assessed using the USAF 1951 resolution target and knife-edge targets.

The following Section 4.2.2 describes the optical set-up used throughout this Chapter. After the system has been laid out, its resolution assessment is presented in Section 4.2.3.

4.2.2 System Set-up

In order to set up a confocal imaging system, the beam path can be sectioned into two arms, the illumination side and the detection side. The increased contrast and resolution are achieved by restricting the overlap between the illumination and detection volumes at the sample position. With optical frequencies, there is typically very little need to condition the illuminating beam, as the beam qualities tend to be sufficient. The detector's volume is restricted by an aperture which cuts off any rays from areas outside of the intended detection volume. In our case, we were working at GHz frequencies, and while our beam quality is quite good (>98% Gaussian output without measurable side lobes), the position of the beam waist is only roughly known and assumed to be 1.7 mm, as quoted by the manufacturer. As for alignment purposes, it was fairly crucial to have an exact location and size for the beam waist of the radiation, the source signal was focused onto an aperture, at which point a new beam waist for the system is defined and used as the input, this time with well known position and size.

Figure 4.1 shows the optical set-up. The system was based around the polariscope used in Section 3.3.2. The source was the same VDI amplifier/multiplier chain fed by an RF synthesiser. The beam is collimated on a first aperture (A_1) using two PTFE lenses (L). This aperture was set to 5 mm diameter in order to have a clean Gaussian input beam while still maintaining reasonable power levels. The beam was then collimated through a

first polariser (P_1) onto an off-axis parabolic mirror with 4" focal length (M). The sample was placed at the mirror's focus, which marks the end of the illumination arm of the system. The beam is then collimated through the analyser (P_2) and focused through the confocal aperture (A_2) which was set to a 3 mm diameter to keep acceptable signal levels. Finally, a last pair of lenses collimated the signal that reached past the aperture onto a pyroelectric detector (D), a THz-9D with M-Link manufactured by Genetec-eo. System alignment was carried out by placing one optic into the beam path at a time and scanning the beam with the detector to optimise the optic's position, no alignment lasers were used as the PTFE lenses stop them from propagating through the system properly.

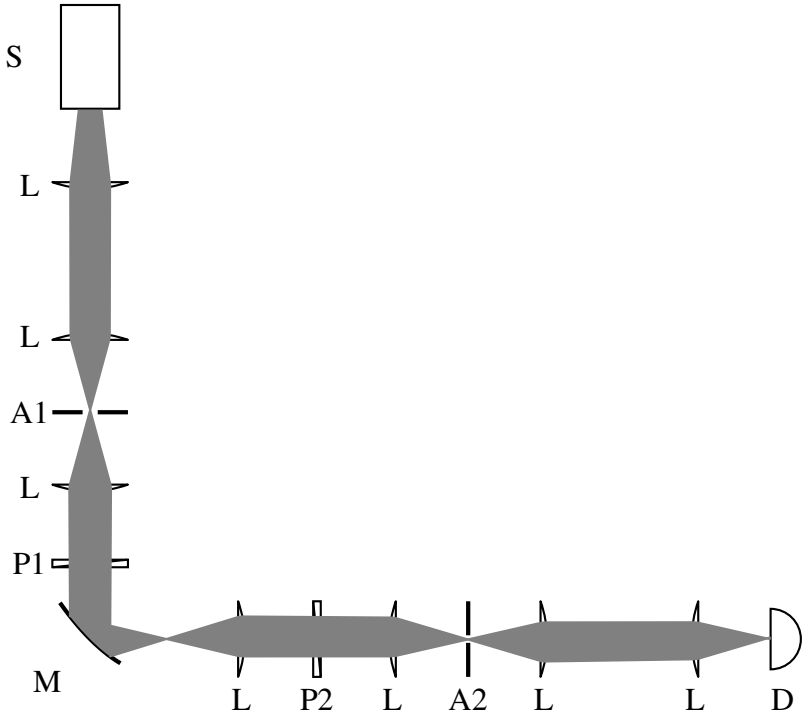

Figure 4.1: Optical arrangement for the confocal imaging system.

4.2.3 System Resolution

Once the system was aligned, a number of measurements were carried out to assess its performance. The first point of interest was the in-plane resolution (i.e. along x and y). This resolution was assessed in a number of ways, first a measurement of a knife-edge was performed, and the width of the edge used as an indicator for the spot size. This was followe by imaging aluminium plates with various widths of slits cut into it and checking

at what point the contrast reached hardly distinguishable values. Finally a USAF 1951 target was imaged and used as an additional indication of the spatial resolution. The second point of interest was how the system's axial resolution changed by introducing the confocal aperture. This was achieved by moving a small aperture through the focus along the beam and measuring the power that reached the detector.

A simple 2 mm thick aluminium plate was used as a knife-edge and scanned across the beam at the focus in both x and y. These scans yielded an average edge function for the two directions which was used to assess the focal spot size, shown in Figure 4.2. It was notable that scanning the plate along x, Figure 4.2a, lead to a shorter edge, $\sim$2 mm, than along y, Figure 4.2b, where an edge of $\sim$3 mm was observed. The beam at the focus is highly circular, which was observed during the beam scans taken while aligning the system, and while deviations towards an oval spot would explain a change in resolution between x and y, a more important factor is that the beam is fully vertically polarised. This means that if the edge is scanned along x, the beam will not show any notable interaction beyond simple absorption with the electron cloud at the edge of the metal while passing the plate as the polarisation oscillates along the edge. There will be a sharp cut off when the beam starts overlapping with the metal where it will all be absorbed. The opposite true with a scan along y, the beam's polarisation will push the electron cloud in and out of the metal, at which point the oscillation induced by the polarisation will push and pull against the metal ions that keep the electron cloud within the metal's boundaries. Thus in case of the x scan, the edge function looks like one of an incoherent image, while the sharp rise in power before the edge for scans along y is typical behaviour of a coherent image. This difference in interaction (and diffraction) means that the start and end points of the edge for the two cases are hard to compare, but it also means that is not unreasonable to assume a very similar resolution in both directions, given that the beam shape is highly circular.

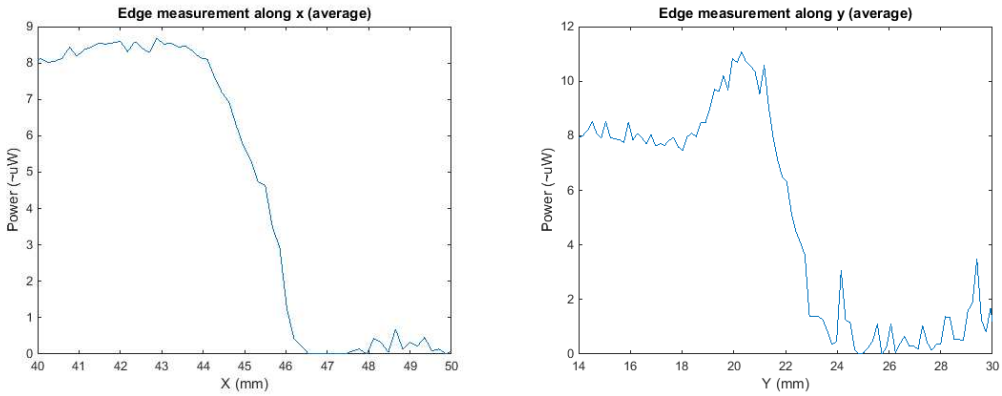

(a) (b)

Figure 4.2: Knife-edge measurements with the confocal system, (a) along x and (b) along y.

The edge measurements give a measurement spot size of the order or 2 mm, which is at a wavelength of 0.91 mm and with an initial beam diameter of ∼5 mm. This was considered a reasonable level of performance, particularly considering that all transmitting optics in the system were off the shelf products optimised for 500 GHz. It should also be noted that the resolution was measured at 330 GHz, which is the peak of the frequency output, and was deemed sufficiently accurate for the useful frequency range of typically 280 GHz to 360 GHz, as the last 20 GHz on either side are at very low power levels, and therefore are generally cut out in the analysis for improved noise performance.

The next test was to see how well sharp contrast could be resolved. This was assessed using a set of aluminium plates with slits cut into them, with Figure 4.3 showing an example of one of them. The slits ranged from 8 mm down to 2 mm.

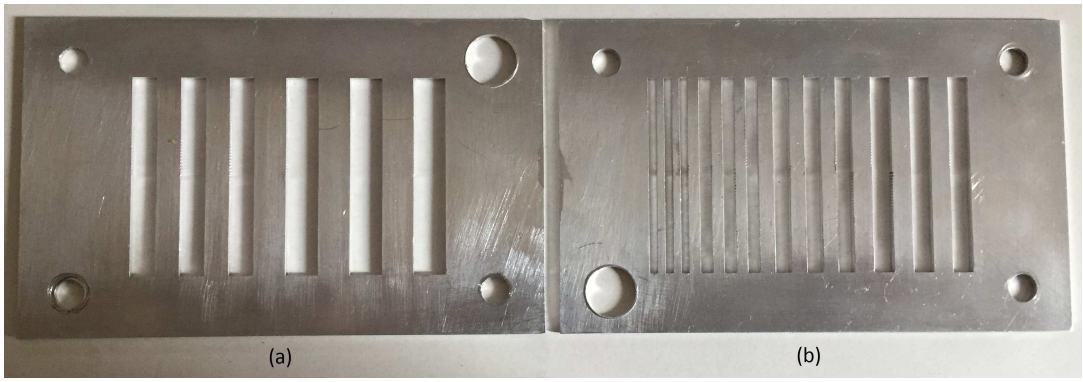

Figure 4.3: Aluminium plate with slits of (a) 8 mm and 6 mm, and (b) 5 mm to 2 mm widths.

An average profile from 10 scans for the targets shown in Figure 4.3 is shown in Figure 4.4 below. Both 8 and 6 mm slits (Figure 4.4a) were very well defined with the power levels reaching the peak signal peak. This still applied for the 5 mm slits on the very right of Figure 4.4b, while from 4 mm onwards, the spot was clearly cut off. At 2 mm, only $\sim 26\%$ of the signal was transmitted. This value related to the Rayleigh limit for contrast resolution, which requires at least 26% of contrast between to adjacent signals for them to be considered as resolved [84] for a traditional imaging system. The confocal aperture, however, helped improve on that limit by reducing the amount of influence that adjacent slits have on the current point measurement as stray light from them was cut out by it, thus leading to a system which could still resolve features of the order of 2 mm, if they were metallic with sufficient transmission on the non-metallic elements.

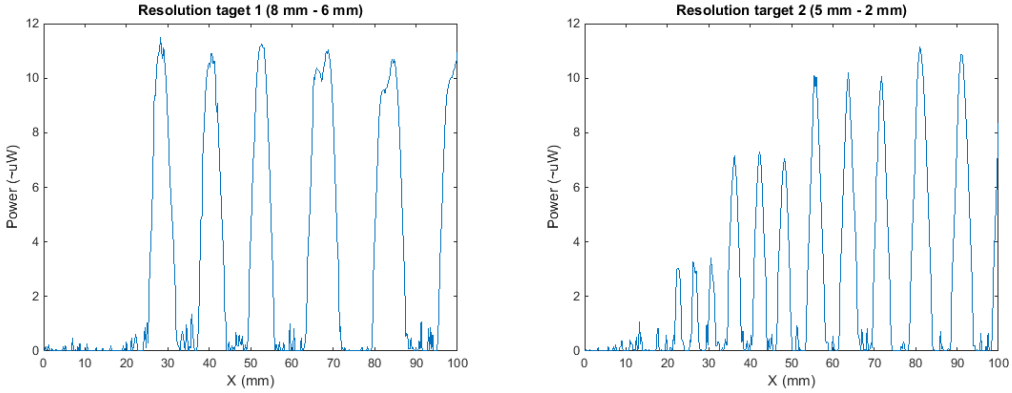

(a) (b)

Figure 4.4: Scan from right to left across the target from (a) Figure 4.3a and (b) Figure 4.3b.

As a final check for the system resolution, a full-field image on a USAF 1951 target manufactured by Edmund Optics was taken, shown in Figure 4.5. These targets have chromium elements on a 1.5 mm thick glass substrate. The target was used by visually assessing which element was the smallest where the lines were distinguishable and using that as the resolution limit. The resolution in line pairs per millimetre for the USAF 1951 target is linked to the element's number and group by

$$Resolution(lp \cdot mm^{-1}) = 2^{\frac{Group+(Element-1)}{6}} \tag{4.3}$$

However, while the resolution can be calculated using the formula, the values are readily available in lookup tables, which are usually shipped with the targets.

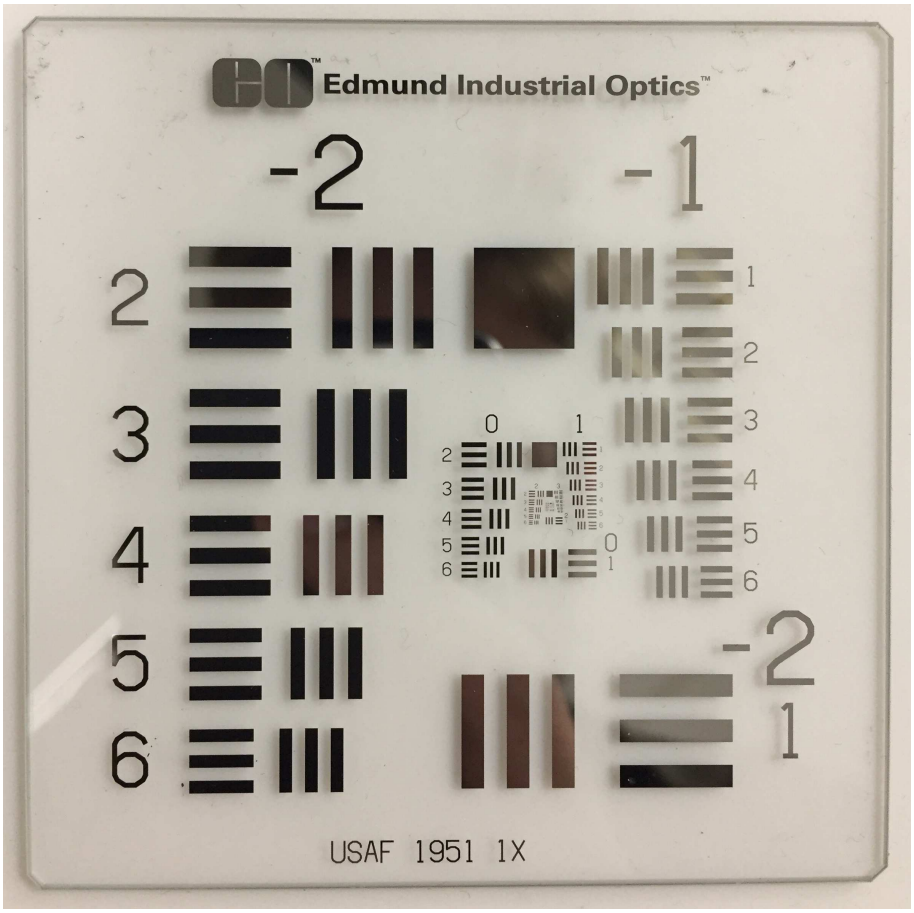

Figure 4.5: Picture of the USAF 1951 target used for resolution assessment.

Figure 4.6 shows the recorded images for the USAF target. Figure 4.6b shows the area of interest, as there was no separation between the lines anymore for the smaller elements. From the lookup table, element 3 (at the top of Figure 4.6b) corresponded to a resolution of 0.315 $lp\cdot$ mm^{-1}, or, in other terms, elements of 1.58 mm size could be distinguished. This has been taken as the resolution limit, and it matches up with the expected lateral resolution limit calculated for the system. It should be noted that the available contrast in the image of the target was only 20% of the full contrast range in the system as the 1.5 mm thick glass substrate was absorbing $\sim$80% of the transmitted power.

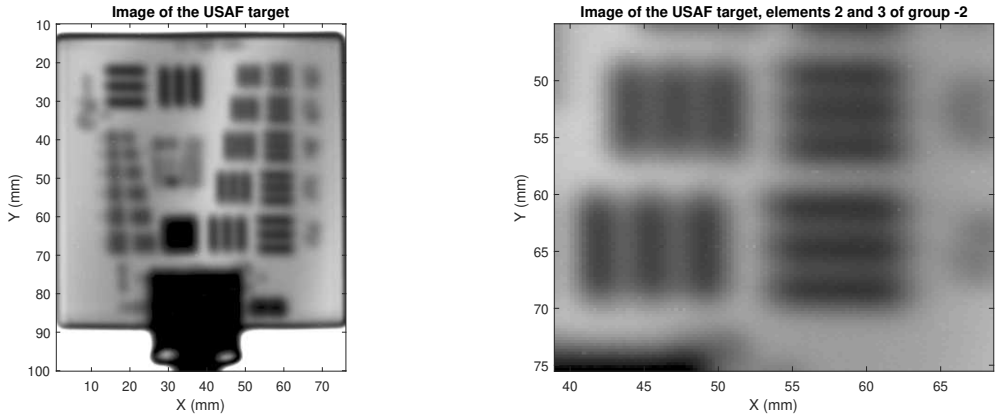

(a) (b)

Figure 4.6: Image of the USAF 1951 target. (a) Full image and (b) zoomed in on the second and third elements of group -2.

Finally, the depth resolution of the system was assessed by scanning a 2 mm wide aperture long the beam through the focus. The full-width half-maximum (FWHM) of the resultant power measurements along z was used to quantify the depth of focus as well as the improvement achieved by adding in the confocal aperture into the system. Figure 4.7 shows the 2 measurements with the FWHM marked and their widths labelled. The improvement in depth resolution was done by taking the difference between the FWHM of both curves and dividing it by the value without aperture. While there was an improvement of 21.9% in the focal depth with the confocal aperture in place, the FWHM was still around 32.5 mm, which doesn't open up the way to do a lot in terms of sub-surface measurements, especially since the coatings that were the end goal of the project are typically around 300 μm. For a fully diffraction limited, the depth resolution would still be of the order of 10 mm, which suggested that if any depth imaging was to be carried out, it had to be done at higher frequencies.

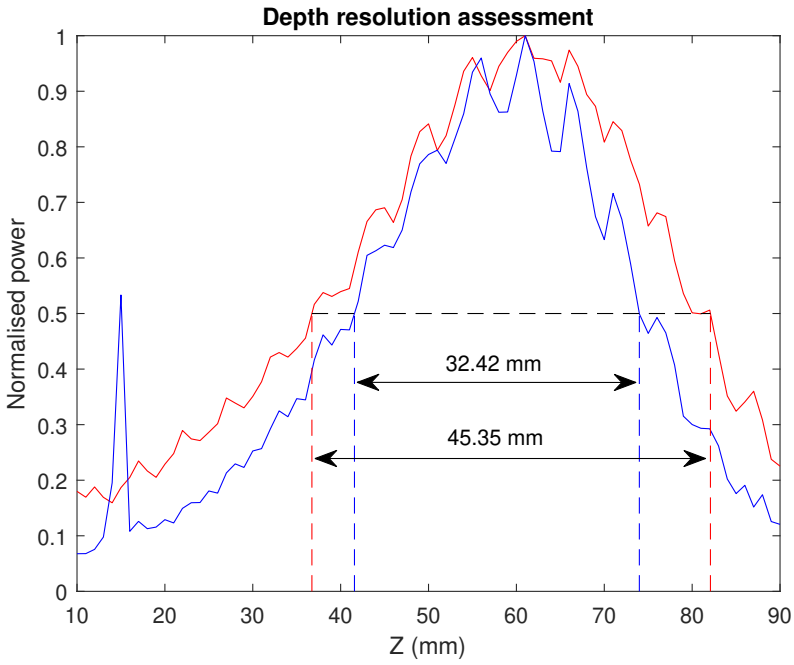

Figure 4.7: Depth resolution assessment. The red curve was taken without the confocal aperture while the blue curve was taken with confocal aperture.

In this section the optical layout of the GHz confocal imaging system has been presented and it's resolution was assessed. The size of the beam at the focus within the confocal volume was estimated to 3 mm, while features down to 1.58 mm could be distinguished in the measurements, which corresponded to the theoretical lateral resolution limit for the system. If the resolution was limited to the Rayleigh criterion, features of $\sim$2 mm were the limit, provided the features were sharp edges from full absorption/reflection to full transmission. While there was a significant increase in depth resolution, it was still not at a level where 3D imaging on the intended samples was feasible at the frequency range of the GHz system.

4.3 Cantilever Imaging

4.3.1 Introduction

After the resolution of the system was assessed (Section 4.2), it was used to attempt 2D stress measurements. The samples used for these experiments were PTFE cantilevers which provided a well known stress distribution that was easy to model as sanity check.

4.3.2 Measurement Procedure

The system was as presented in Section 4.2 and is shown in Figure 4.1. The entire set-up was within an anechoic chamber to absorb any stray reflections and avoid standing waves throughout the room affecting the measurements. The samples were laser cut from 5.5 mm thick PTFE sheets. In order to load them, a mount was designed which could hold them and apply a displacement to the cantilever at 3 different positions, shown in Figure 4.8. The cantilevers are 150 mm long and 30 mm wide, but the load was applied at 80 mm from the base. The base size was chosen as 90 mm by 45 mm to have enough area to clamp down on it with 4 screws, spreading some of the big strain distributions around the screws over the entire area. Additionally, it was chosen to be wider than the clamping plate so that the corners would be visible in the images. In order to produce the images, the mount was attached to an 2 axis translation stage and scanned through the focus.

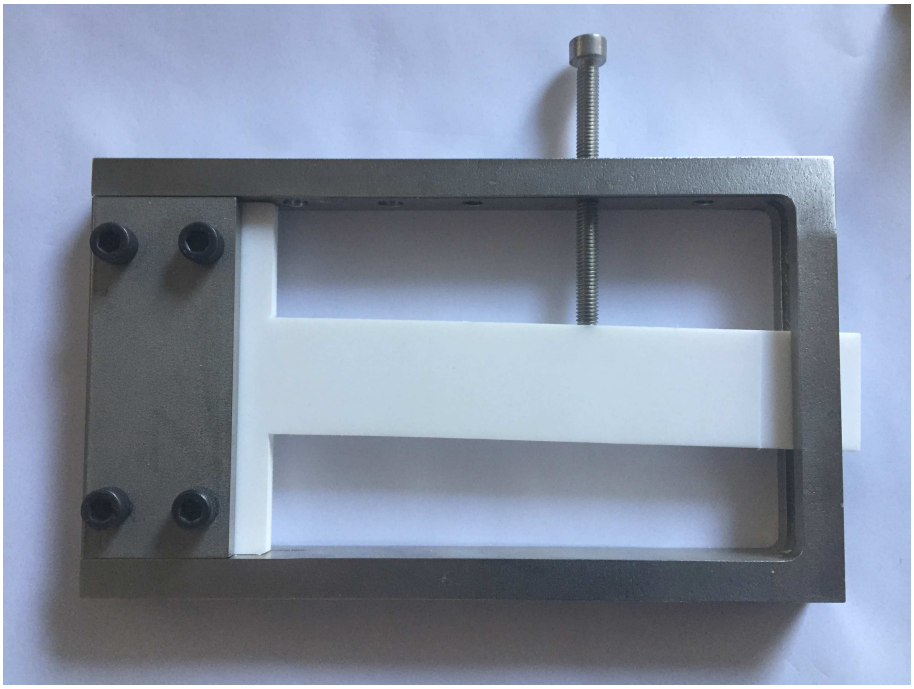

Figure 4.8: PTFE cantilever in its mount.

As part of the design process, a MATLAB®model for the stress distribution within a cantilever was written. In order to assess the feasibility of imaging the stress distributions, they were transferred into phase maps using the stress-optic coefficients presented in Section 3.3.4. The equations used for this models are

$$\sigma = \frac{Fy}{I} \cdot (L - x) \tag{4.4}$$

where σ is the stress at point (x, y) in Pa, F is the applied force in N. L is the length of the cantilever from the base to the point where the load is applied, x is the distance from the base, y is the distance from the neutral axis which runs along the centre of the cantilever, and I is the moment of inertia for the cantilever and can be calculated as follows,

$$I = \frac{db^3}{12} \tag{4.5}$$

with d being the thickness of the cantilever and b the width. The calculated stress values could be used with the stress-optic law to calculate the stress induced phase change by using the previously measured stress-optic coefficient, which in turn can be used to calculate the expected power distribution through the sample. The stress-optic law can be expressed as follows

$$\delta = \frac{2\pi}{\lambda}\, d\, C\, \sigma \tag{4.6}$$

where δ is the stress induced phase change, λ is the radiation wavelength, C is the stress-optic coefficient and all other symbols are as defined above. Finally, the measured power is given by

$$P = P_0\, cos^2(\frac{\delta}{2}) \tag{4.7}$$

with P_0 being the reference power without sample present.

The distributions were generated at high resolution and down-sampled to yield a fringe image with 3 mm pixels. An example of the code's output is shown in Figure 4.9. The stress distributions calculated through these simulations were later also compared to the results obtained from the DIC system, which measures surface strains directly, which can be transferred into stress values with PTFE's Young's modulus.

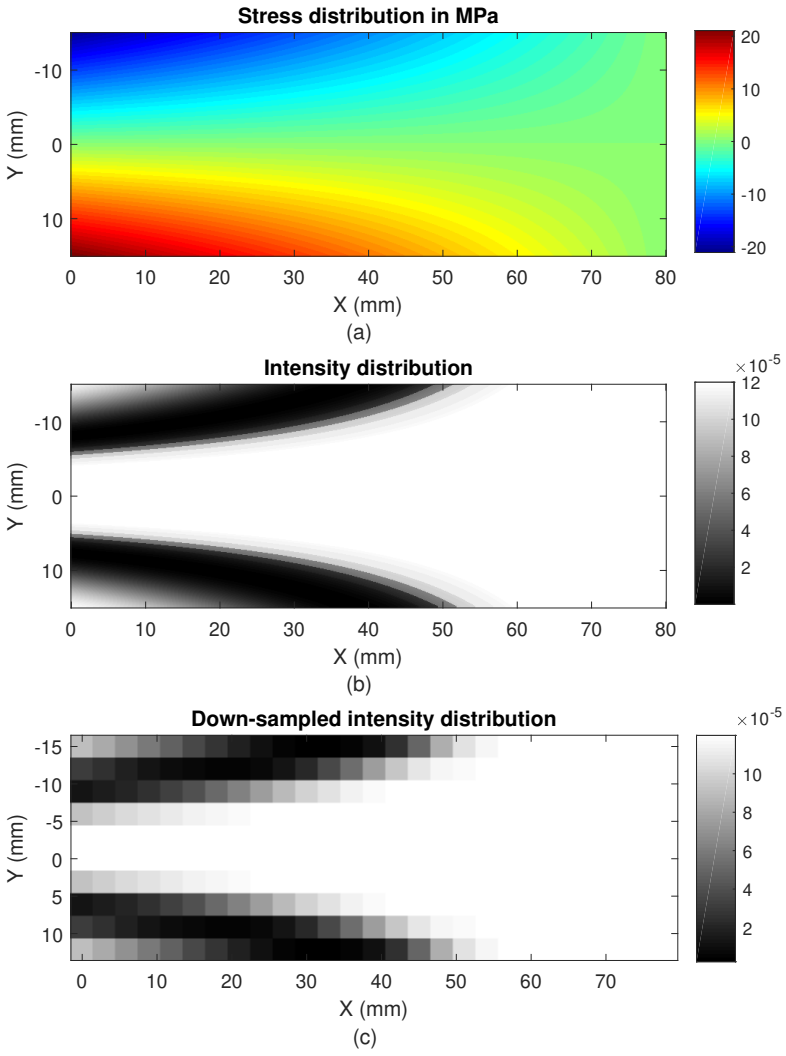

Figure 4.9: Simulation of (a) the stress distribution and (b) the corresponding measured power for a PTFE cantilever. (c) shows the power distribution down-sampled for 3 mm pixel sizes.

At each (x, y) position, the transmitted power was measured for a source frequency scan from 260 GHz to 480 GHz in 0.25 GHz steps. This spectrum was then processed by applying the same Fresnel fits than those used in Section 3.3. Finally, the refractive index distribution was used to calculate a stress map by using the stress-optic coefficient. It is worth noting that the point where PTFE yields, as provided by the manufacturer, is between 8 MPa and 12 MPa. Most tested samples showed yielding behaviour above 8 MPa. This limit was used in the decision on how far to stress the cantilevers, with most having been stressed to the yield stress at the base. The simulations were used to estimate

the amount of displacement required for this by adjusting it while monitoring the stress values at the base and finding where this corresponded to 8 MPa.

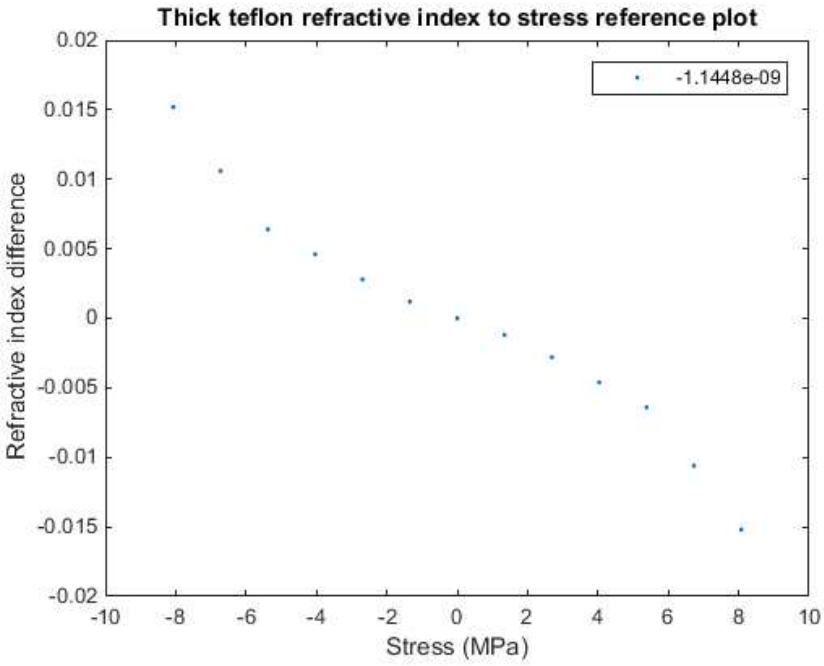

Figure 4.10: Reference stress-optic plot used for the analysis of all the cantilever data. The label is the stress-optic coefficient in Pa^{-1} fitted over the central linear region.

4.3.3 Results

In this Section the main outcomes of the confocal imaging experiments are presented, which will be followed by a discussion of their implications in the following Section 4.3.4.

Once the confocal system was fully aligned and characterised, a high resolution single frequency image of a sample in its mount was taken which was then used as positioning guide for all further measurements. This image is shown in Figure 4.11. The scan range for all later the measurements was limited to the region from 33 mm to 69 mm in x and 23 mm to 47 mm in y with step sizes of 3 mm for both cases. This was done in order to focus on the base of the cantilever where the strain is the highest as well as to reduce the measurement time, as one frequency sweep took 10 minutes to complete.

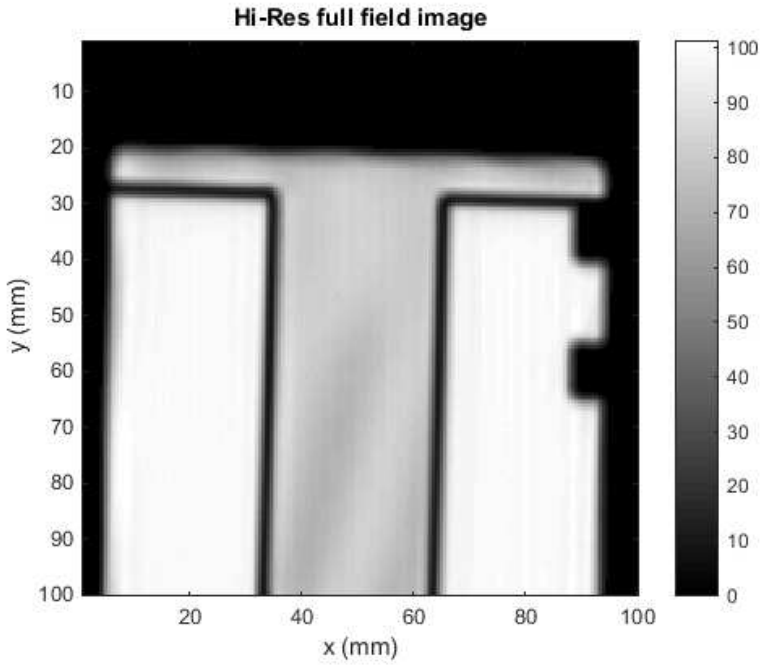

Figure 4.11: High resolution full-field image of a cantilever in its mount.

Figure 4.12a below shows a measured stress distribution for a cantilever stress to just beyond the manufacturer's yield point range by applying 4 mm of displacement at 8 mm from the base. The simulated distribution for the same applied load is shown Figure 4.12b both at the model's high resolution and down-sampled to match the measured image resolution. The measured distribution and the simulated one generally match up reasonably well, with some differences in the peak values measured. It should be noted that the simulations did not plot the results onto a bent shape, but just predicted what the stress at each point in the sample were going to be, not were the points would move to between images. However, since the measurements focussed on the base, the movement was small enough compared to the pixel size that the effect of the movement of the cantilever was safe to disregard. The differences in peak values could be explained by diffraction, which made measurements around the edge unreliable, and as the stress peak is located in the corner at the base, it was extremely unlikely that that would be properly resolved.

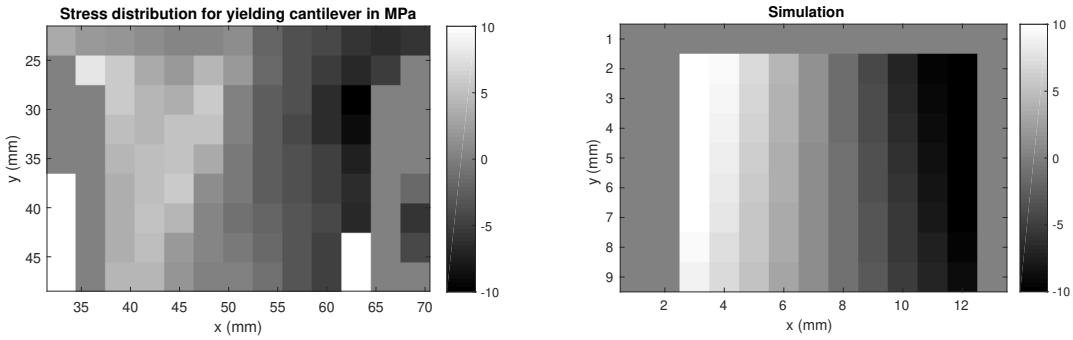

(a) (b)

Figure 4.12: (a)Measured stress distribution and (b) Simulated stress distribution for a cantilever stressed to the yield point.

While there was some occasional samples that were reasonably well behave (like the one shown in Figure 4.12a) most showed much less reliable results. Figure 4.13a shows a much more typical result, with the corresponding simulation in Figure 4.13b. The black lines around 40 and 70 in x are artefacts in the refractive index calculations caused by the sample edge, while a number of points within the sample don't converge to reasonable values during the fitting process. These issues will be laid out and explained further in the discussions following below.

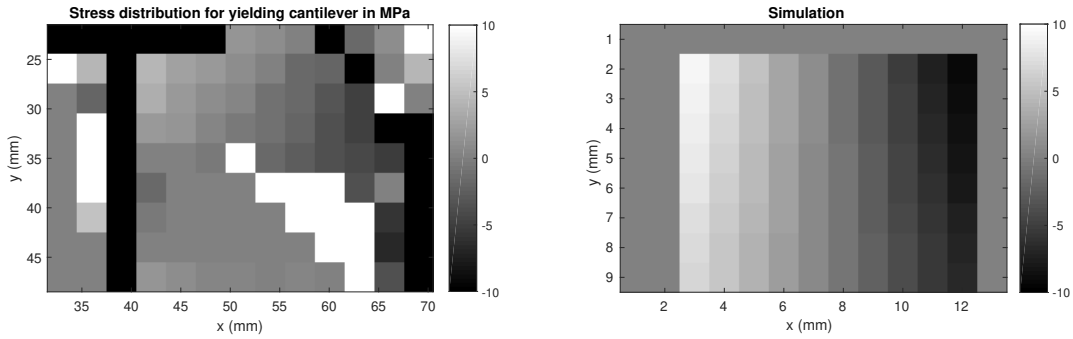

(a) (b)

Figure 4.13: (a)Measured stress distribution and (b) Simulated stress distribution for a cantilever stressed to the yield point.

4.3.4 Discussions

The system showed pretty reasonable imaging quality as seen in Figures 4.6 and 4.11 for imaging with 1 mm wavelength, however this was not an aim, but rather a step in order to try measure stresses in at least 2 dimensions, as the depth resolution is still fairly poor at over 20 mm. The measurements of stress distributions was partially successful, with the approach working well for some samples while failing to provide reasonable results for others.

This Section will focus on the measurements that failed and explore the reasons as to why this happened rather than home in on a minority of measurements that worked well.

First the measured power spectra for a ”good” and a ”bad” measurement are presented. Figure 4.14 shows examples of a ”good” (Figure 4.14a) and a ”bad” trace (Figure 4.14b). The spectrum shows signs of interference between multiple oscillations. Two possible causes for this were either standing waves within the system at particular frequencies, or thickness variations across the sample within the beam volume. The first of those two was checked for by rotating some of the optics by a small angle, while the polarisers were in the system at 45° in order to avoid standing waves. There was no notable difference in the quality of the spectra before and after rotating the lenses.

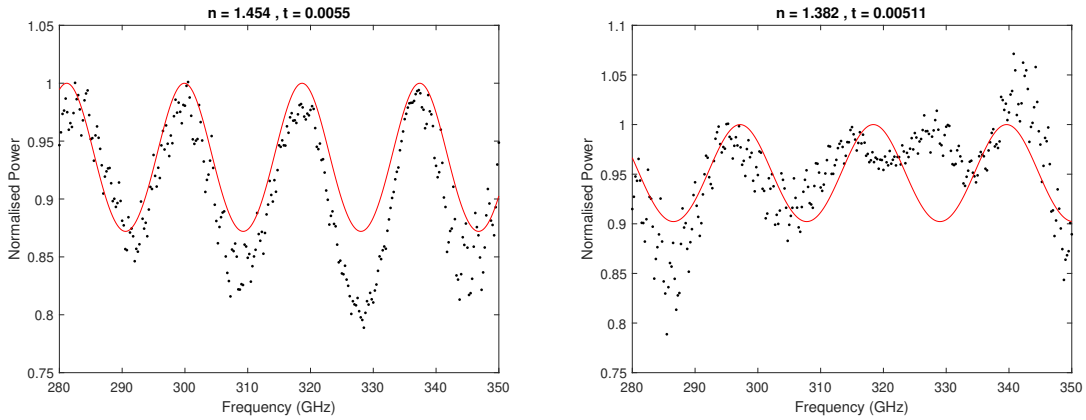

(a) (b)

Figure 4.14: Typical power spectrum for (a) a good measurement (b) a bad one, in both cases the red line is the best fit to the data.

In order to see if the issues were linked to the sheet of PTFE that the cantilevers were

cut from, some samples were cut from a different sheet ($\sim$2 mm thick). That sheet's surface was smoother to the touch than the thicker one, which meant that there should be less local thickness variations. Stress distributions for two samples are shown in Figure 4.15. In both cases, there are clear artefacts in the image, but rather than being linked to a simple variation in sample thickness, the thinner samples were twisting out of plane rather than simply bending downwards, which could explain the shapes seen on Figure 4.15b. Generally speaking, if the value for the stress is at either end of the scale, it means that for that pixel, the Fresnel fit was not converging to any reasonable value.

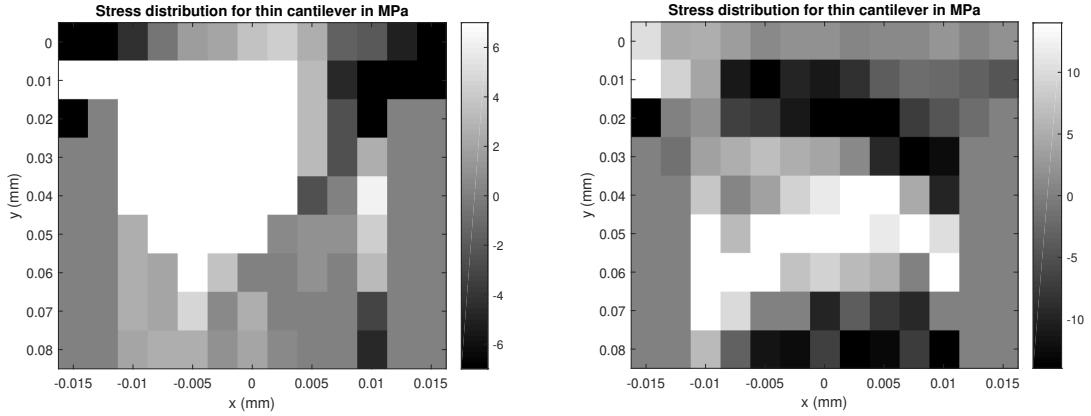

(a) (b)

Figure 4.15: Stress distributions for 2 mm thick samples at (a) 2 mm displacement and (b) 4 mm displacement.

As the thin samples showed a different kind of issue to the thicker ones, those latter ones were imaged under a confocal microscope to measure the surface variation. A line along the width of the cantilever close to its base was imaged with a step size of 2 μm. In order to get an idea of the variation the the signal will realistically be affected by, the measured profile was low-pass filtered using $\frac{\lambda}{3}$ to determine the bandwidth of the filter. Figure 4.16 shows these measurements for a 5.5 mm thick PTFE cantilever. The slope in the data of the front side was not removed as there was a good chance that it was real, but there was no direct way to double check that. The typical variations on the front surface were of the order of 10 μm over a 3 mm spot, and the back surface had variations of 3 μm across a similar spot size. Additionally, there might have be overall thickness variations across the spot of at least 10 μm. This all added together to an uncertainty in thickness over the spot size of the order of 23μm. The presence of a whole range of thicknesses within the spot size would lead to interference between a number of different Fresnel

responses and the occurrence of varying amounts of standing waves within the sample across the scanned frequency range, which in turn could generate a spectrum similar to the one shown in Figure 4.14b.

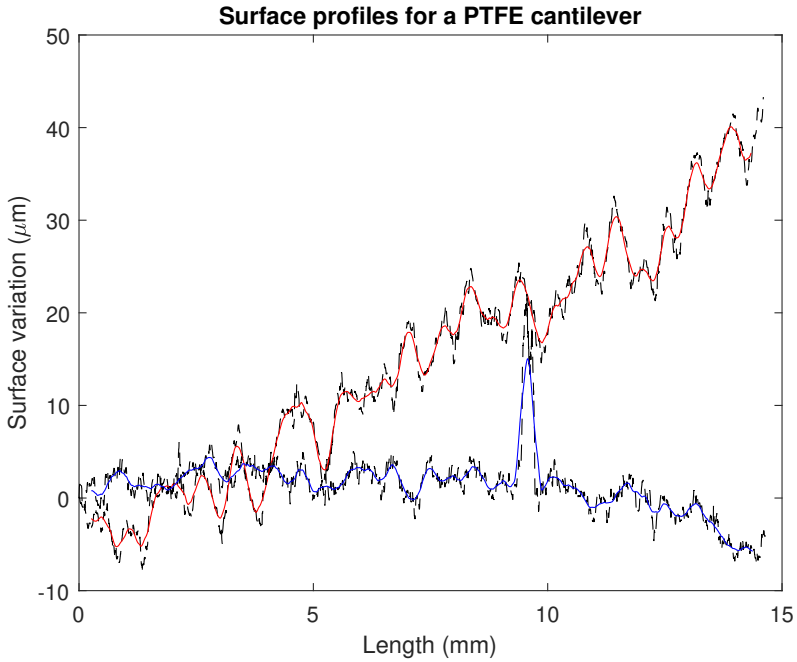

Figure 4.16: Surface profile measurement for a PTFE cantilever. The black lines are the raw data, while the coloured lines are the low-pass filtered profiles. The red line if e measurement of the front surface, while the blue line is a measurement of the back surface.

The confocal system was used to perform stress measurements in 2 dimensions. Generally, the experiments were successful with the given aim of assessing the feasibility of confocal imaging at THz frequencies for strain mapping. On the other hand, most of the issues encountered throughout the measurements were identified and narrowed down to sample properties. Specifically the quality of the sample surfaces, both in terms of roughness and in terms of thickness variations across the sample width over the spot size.

4.4 Conclusions

Within this chapter the use of a Virginia Diodes amplifier/multiplier chain operation in the WD 2.8 band (260-400 GHz) and a pyroelectic detector as source and detector for a confocal imaging system was presented. The lateral resolution of the system was assessed and

found to be at least 0.315 $lp{\cdot}\mathrm{mm}^{-1}$. The assessment was limited by the transmittance of the fused silica substrate that the resolution test chart was deposited onto, which absorbed close to 80% of the incoming signal. In terms of depth resolution, an improvement of 22% was measured, however, this still left the system unsuitable for measurements along the z-axis, as the spot size was still at 32.5 mm. Even if the system was fully diffraction limited, the best resolution along the z-axis would be around 20 mm, which made depth imaging on thermal barrier coatings next to impossible, as their thicknesses are typically only 300 μm. The system was applied to produce stress images on PTFE cantilevers, and while in some instances the results looked promising and matched the theoretical expectations reasonably closely, in general thickness variations across the 3 mm imaging spot size meant that a large part of the recorded Fresnel spectra were unsuitable for fits which did not allow for a combination of several thicknesses. Implementing this in turn would have meant to increase computation times from a few minutes per pixels to a few days per pixels and was deemed an unjustifiable use of time. In other words, the system showed promise for producing stress images but a much more controlled set of samples would be required to get a final verdict on its performance. However, in order to benefit from better spatial and axial resolution, any further experiments on confocal stress imaging should be carried out at higher frequencies.

Chapter 5

TDS measurements

5.1 Introduction

In order to extend the measurements presented throughout this Thesis from the GHz range into the THz range, work with time-domain spectroscopy (TDS) systems was carried out. These systems use ultrafast THz pulses with typical bandwidths of 6 Thz and peak amplitudes around 500 GHz. After investigating some of the noise sources in those systems and how they affect the any strain-optic measurements, the main materials used throughout the project were characterised. Once the base properties of the relevant materials were known, a set of strain-optic measurements was performed on samples which had previously been tested in the GHz range as well as some new samples which had not been investigated up to that point.

This chapter is thus split into 3 main sections, where the first introduces the different TDS systems that were used and shows what the limitations and requirements in terms of noise performance for the strain-optic measurements are, while the following chapter presents the results of the material characterisation experiments. Finally, the third chapter reports the outcomes of the strain-optic tests performed with a TDS spectrometer.

5.2 Experimental Systems

5.2.1 Introduction

This Section will present the 3 different TDS systems that were used throughout the project and provide a comparison of their performance. The first system that will be looked at is one which used ZnTe crystals for both the THz generation and detection and that was based at Heriot-Watt (HW), the second system was the NPL's system, which used a photoconductive antenna for the generation and a ZnTe crystal with balanced photodiodes for detection, while the final system was a commercial system provided by Toptica Photonics and used photoconductive antennas for both generation and detection.

5.2.2 System Specifications

The first and second systems were both using a Ti:sapphire laser to provide fs pulses with around 800 nm central wavelength. Figure 5.1 shows the layout for the NPL's system, which was a typical layout for a TDS system, and was also the layout that was used at Heriot-Watt. The pump laser used at Heriot-Watt was an amplified Ti:sapphire with 100 Hz repetition rate and 110 fs pulse length, while the NPL used a Ti:sapphire laser with 77 MHz repetition rate and 20 fs pulse length. The delay in the path of one of the optical beams was provided by a mechanical translation stage. At Heriot-Watt, a ZnTe crystal was used to generate the THz pulse through optical rectification, while the detection used a second ZnTe crystal combined with a Wollaston prism to separate s and p polarisations of the probe beam, the difference between which was then picked up with a balanced pair of photodiodes. At the NPL the emitter was a GaAs based photoconductive antenna while the detection was performed in the same way as at Heriot-Watt.

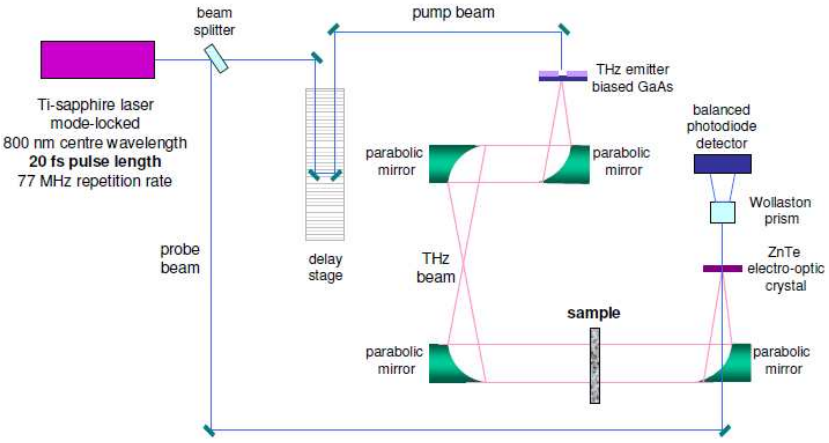

Figure 5.1: TDS setup at the UK National Physics Laboratory [23]

Finally, the commercial system was mostly fibre enclosed with only the THz beam travelling through the air between the emitter and receiver antennas, which were fibre coupled InGaAs based antennas. The delay was provided by a harmonically oscillating voice coil. Finally, the fibre laser produced 45 fs pulses at a repetition rate of 100 MHz. A picture of the system is shown in Figure 5.2.

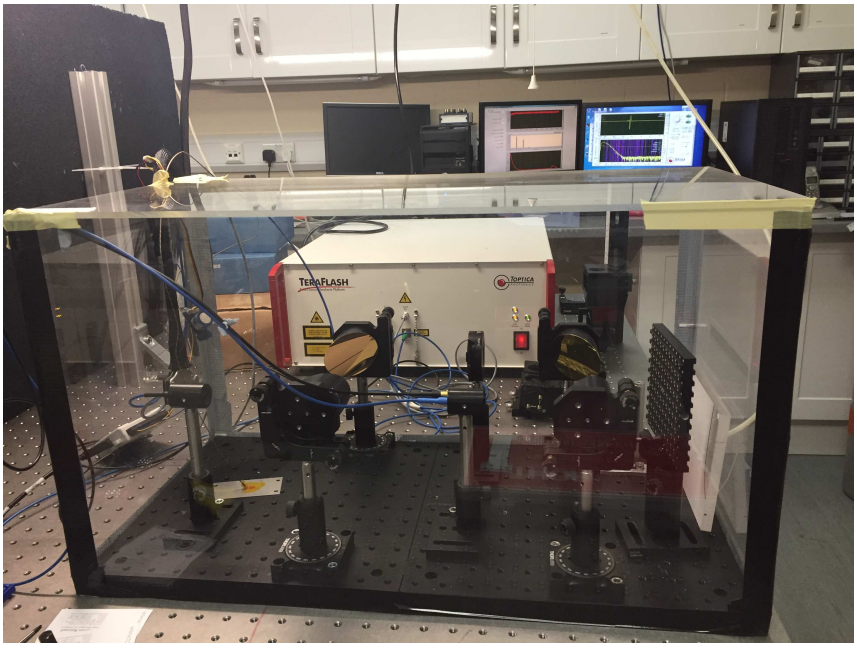

Figure 5.2: TeraFlash system provided by Toptica Photonics.

Since several different system were used throughout the project, a metric was required to compare their performances. In this case the system dynamic range and signal to noise ratio were chosen as a reasonable indicator and calculated as shown in [85], bearing in

mind that the signal to noise ratios of the different systems were biased through the lack of similarly amounts of averaging. For the HW data, an average of 5 traces was taken, while for the NPL data, 10 traces were averaged. While at the NPL, each recorded trace is already an average of several traces, at HW barely any pre-averaging was performed due to the low laser repetition rate. With the TeraFlash, each recorded trace was an average of 1000 traces, and a large number of traces were taken specifically for noise analysis, which leads to a disproportionately high SNR for that system compared to the other two. In numbers in the time domain, at HW, the peak SNR was 164, versus 181 at the NPL and 279 with the TeraFlash. In the frequency domain, the system at HW reached an SNR of 150, the NPL one of 260 and the TeraFlash one of 680. There are significant differences between systems, but while the HW system did suffer from low averaging capability and a very unstable pump laser, at the NPL these numbers could still be improved at the cost of a longer acquisition time both per trace an in terms of the number of traces used for each measurement. The differences in dynamic range, while significant, were somewhat less extreme, as seen in Figure 5.3.

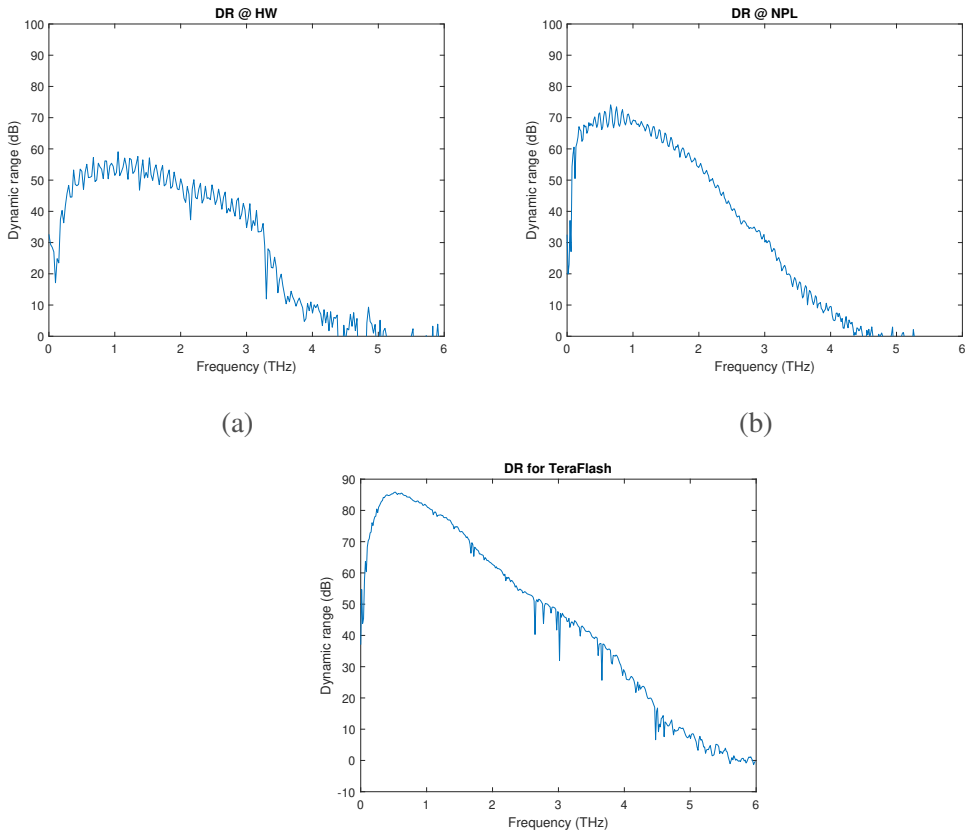

Figure 5.3: Dynamic range in decibel for the (a) the system at Heriot-Watt, (b) the NPL's system and (c) the TeraFlash system provided by Toptica Photonics.

The peak dynamic range at HW was close to 60 dB, one reason for this was that the evacuation chamber wasn't performing too well, leaving a lot of water vapour in the beam path. The shapes for the dynamic range curves plotted against frequency for the other two systems were very similar, though the TeraFlash showed both a better dynamic range (peak at 85 dB vs 72 dB at the NPL) as well as a higher cut-off frequency (it cut off at 6 THz as opposed to 4.5 THz), which is a consequence of the increased dynamic range.

A lot of the measurements performed (and presented later in this chapter) were analysed using time-of-flight calculations rather that using the Fourier analysis. This was due to the nature of the samples and the measurement which led to the inability to properly separate the reference and sample pulses at a sufficiently high time-resolution. However, this meant the errors in peak position had to be considered, as that position was the defining parameter when it came to time-of-flight calculations. A number of traces were taken using the HW system, on which the peaks were then isolated and super-resolved using peak fitting. The typical variation of the peak position from those fits was found to be close to 10 fs. This figure was important for 2 reasons, first of all, the expected peak shifts across a full strain-optic test for our samples were expected to be of the order of 10 fs, shown in Figure 5.4, so if the noise in peak position is at the same level, the experiment couldn't work. This limitation could be overcome though by recording a reference pulse at the same time as a sample trace, an approach which is shown in Section 5.4.2. Additionally, the the accuracy of a typical mechanical translation stage as is used to provide the optical delay is 2 μm, which converted to travel time for an optical pulse (keeping in mind that it travels the distance twice due to how the delay lines are set up) is 13 fs. The stage accuracy affected the measurements in that way since the stages are told to move from a position A to a position B at constant velocity. However, the stage accuracy means that there is a 2 μ uncertainty in the starting position as well as the end position (which is less important in this case, as it won't affect where in the data the peak is positioned). Unless the stage position is monitored by additional high-accuracy measurement approaches, this error will be present in the data.

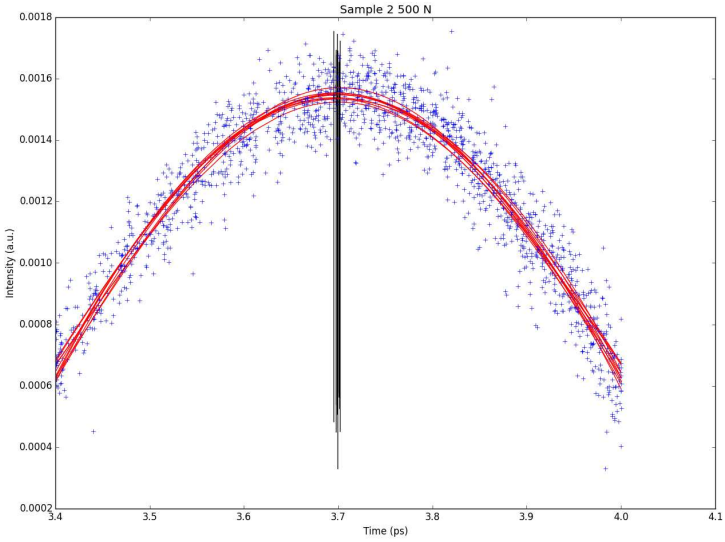

Figure 5.4: Shift in pulse peak position after peak fitting, the plot contains 10 traces that were recorded back to back.

Once the noise affecting our measurements was understood to a reasonable degree, the measurement approach in Section 5.4.2 was developed to overcome them. Before it was applied though, a number of material characterisation experiment were performed and will be reported next.

5.3 Material Characterisation

5.3.1 Introduction

In order to gain further insight into the samples under test, as well as facilitating the design of further samples, the complex refractive index of the sample materials needed to be assessed. Since all of the work was carried out in the THz band, information on material properties was not always readily available, and in the case of some materials, they are highly dependent on manufacturing conditions. In order to measure the complex refractive index for a number of different materials, the THz TDS system of the NPL was used. The setup used at the NPL can be found in Figure 2.3, while the details of the analysis procedure can be found in section 2.2.5. This system was used for almost all characterisation experiments, while the strain-optic experiments presented in Section 5.4 were performed with the TeraFlash as the tensile stage couldn't be fitted suitably into

the NPL's system. Aside from providing information on the noise limitations of TDS systems, the Heriot-Watt system didn't lead to any useful results.

5.3.2 Experimental Procedure

The samples shown in Table 5.1 were all tested with TDS. The coated sapphire samples had a thermal barrier coating based on YSZ deposited on them by electron vapour deposition, the first coating is an older form which was deposited in July 2014, while the second one is the current form, deposited in March 2015, that is used at Cranfield University for tests (and is very close to the coatings used by Rolls Royce on turbine blades).

Material	**Length**	**Width**	**Radius**	**Thickness**
PTFE (Teflon)	100 mm	50 mm	N/A	8.85 mm
YTZP	100 mm	20 mm	N/A	583 μm
YSZ	N/A	N/A	16 mm	0.45 mm
Al_2O_3	N/A	N/A	50 mm	2.7 mm
Sapphire	N/A	N/A	20 mm	3.06 mm
YSZ coated Sapphire 1	N/A	N/A	20 mm	3.23 mm
YSZ coated Sapphire 2	N/A	N/A	20 mm	3.35 mm

Table 5.1: Samples tested with time-domain spectroscopy. All samples except the Al_2O_3 and the uncoated Sapphire were tested at the NPL, while those two samples were tested with the TeraFlash.

All of the rectangular samples were tested in the collimated part of the beam (sample position as shown on Figure 2.3), while the circular samples were placed at the focus. The THz generation and detection takes place in an evacuated chamber, which is filled with nitrogen in order to remove the water vapour out of the beam path and avoid its absorption lines. For each sample, 5 measurements were taken, which were subsequently averaged in order to improve the signal to noise ratio. For the reference signal, 10 measurements

were taken and averaged.

In the following 3 Sections, the measured material properties for the samples in Table 5.1 will be presented. The samples were split into 3 groups, with the first one only containing PTFE, a polycrystalline polymer. The second group contained the two zirconia based materials and the last group was made up of the Al_2o_3 samples, including the ones coated with yttria stabilised zirconia.

5.3.3 PTFE

PTFE was analysed as on one hand it was expected to exhibit very low dispersion and absorption, which was why PTFE lenses are commonly used in the GHz and THz ranges. On the other hand, it was also used as the test material in the initial stress-optic tests (Section 3.3) as well as for the confocal imaging experiments (Section 4.3). Therefore it was deemed useful to take a look at it with a TDS system, which is also seen as the industry standard for material characterisation for frequencies from $\sim$100 Ghz up to 10 THz, although typically systems show bandwidths between 4 and 6 THz.

While PTFE has a reasonably low refractive index in the THz range, the time delay between the reference trace and sample trace in this case was fairly significant due to the sample thickness of 8.85 mm and can be seen in Figure 5.5. The fact that the PTFE pulse had the same shape as the reference one without any easily distinguishable broadening hinted at the lack of dispersion in the sample, while the peak intensities show that there is fairly little loss across a sample of significant thickness.

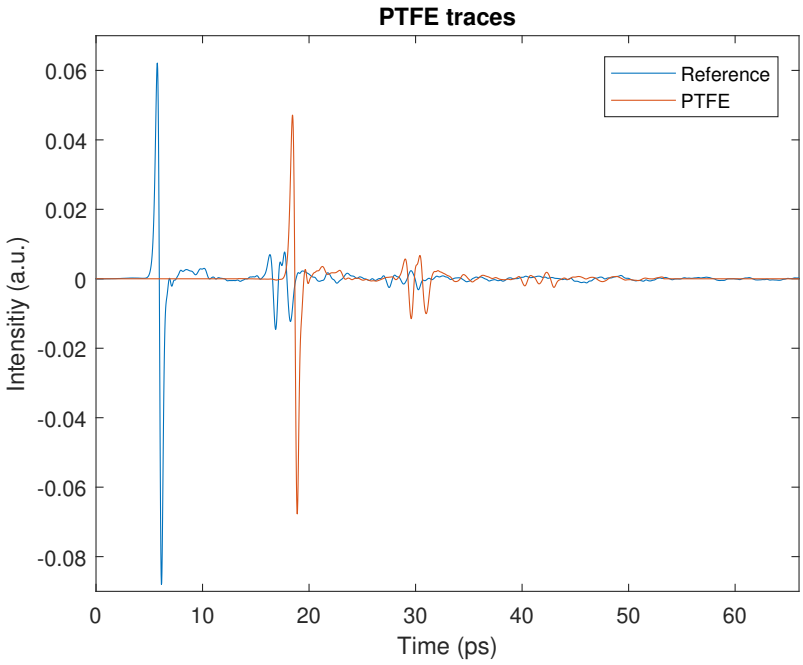

Figure 5.5: Reference (blue) and sample (orange) time domain traces for the PTFE sample.

These expectations on the optical properties for PTFE were confirmed after they were calculated, with their results shown in Figure 5.6. The refractive index was flat at $\sim$ 1.431 up to 2 THz, after which point it started to slowly rise up to 1.435 at 3.5 THz. The absorption coefficient reached 2 cm^{-1} at its highest before the limit in the system bandwidth was reached. It should be noted that the absorption specifically can vary quite a lot with sample purity, the purer the sample. The sample used in this instance was of very high purity, which means that it represented the properties of pure PTFE very well.

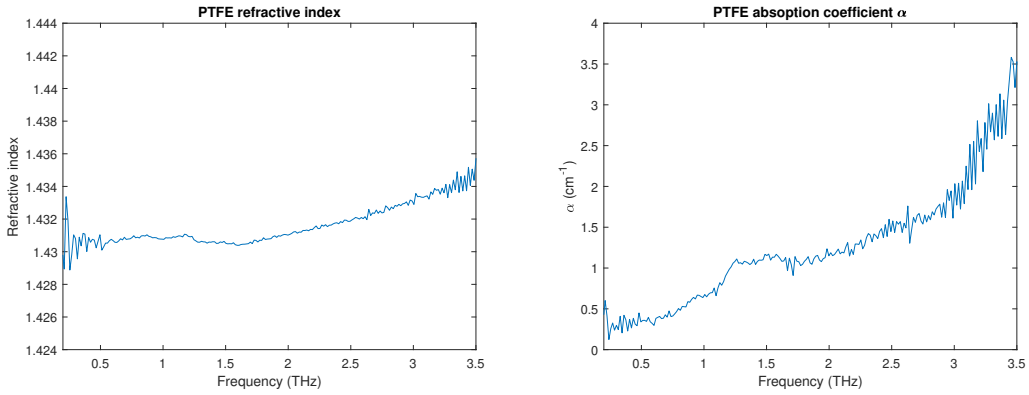

(a) (b)

Figure 5.6: Optical properties of PTFE measured with TDS. (a) Refractive index and (b) absorption coefficient α.

Once the PTFE sample was analysed, the attention was shifted to materials more relevant to measurements on thermal barrier coatings.

5.3.4 Bulk Zirconia Samples

Measurements on a few ziconia based materials were performed to get an idea of how YSZ based thermal barrier coatings will react to GHz and THz radiation. Specifically, sintered yttria partially stabilised zirconia (YTZP, or Y_2o_3 partially stabilised ZrO_2) samples of 600 μm thickness and a disk of 450 μm thick yttria stabilised zirconia (YSZ) were looked at to assess the properties of the material making up most of a thermal barrier coating.

The YTZP samples' thickness was chosen based on the absorption properties of the YSZ sample. While the time delay between the reference and sample pulses in Figure 5.7 was fairly small compared to that seen in Figure 5.5 for PTFE, it should be noted that the YSZ sample is about 20 times thinner than the PTFE one. The absorption though is very notable for that thin a sample and the fact that the pulse also shows clear broadening indicates that there is significant dispersion.

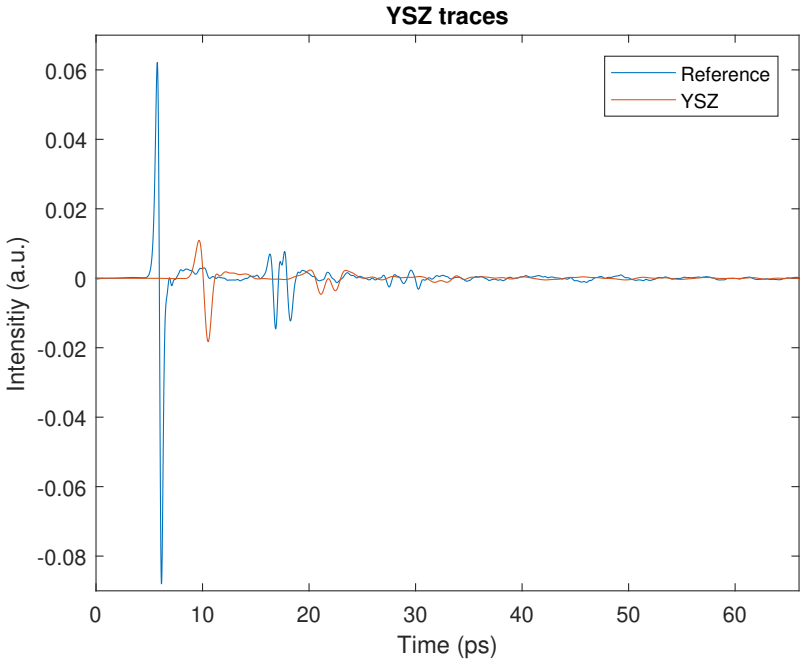

Figure 5.7: Reference (blue) and sample (orange) time domain traces for the YSZ sample.

Figure 5.8 contains the refractive index and absorption coefficient for the YSZ disk.

The refractive index varied from around 3.7 at 100 GHz to 3.9 at 1.5 THz, which was the cut-off in terms of bandwidth for that sample, which is the point at which the limits of the system dynamic range are reached. The absorption on the other hand started around 50 cm^{-1} and rose up to 350 cm^{-1}, which explained the short bandwidth of only 1.5 - 1.6 THz. While this sample provided a good starting point to look att yttria stabilised zirconia ceramics, both it's percentage of yttria as well as its porosity are unknown, as is the way it has been manufactured. However, as there has been evidence in the literature that the refractive index is highly dependent on porosity while the absorption is a lot less affected by it [8], the values for the absorption were used to calculate a maximal thickness for a given SNR over the frequency bandwidth of the measurements.

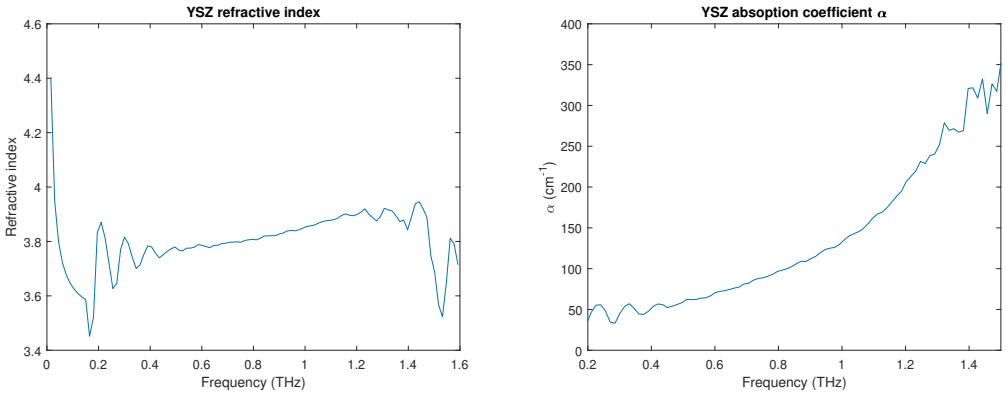

(a) (b)

Figure 5.8: Optical properties of YSZ measured with TDS. (a) Refractive index and (b) absorption coefficient α.

In order to achieve this calculation, the absorption coefficient was used together with the Beer-Lambert law to calculate what thickness of YSZ was required for an SNR of 1, an SNR of 2 and 50% of the power to be transmitted through the sample. The Beer-Lambert law can be written as follows

$$I = T^2 I_0 e^{-\alpha z} \tag{5.1}$$

where I is the leftover intensity after passage through the material, I_0 is the intensity entering the material, α is the absorption coefficient in cm^{-1}, z is the thickness of material the light has travelled through in cm, and T is the Fresnel transmittance. The output power of our source around 330 GHz was 1 mW. For the calculations presented below, the Fresnel reflection off the front surface was subtracted from the incident power, at which point $T^2 = 1$. For ease of calculation, the Fresnel reflection was taken as a constant

34% (from a refractive index of 3.8), thus leaving 660 μW as power entering the material.

Equation 5.1 can be rearranged to yield the thickness for a specific ratio of incident over outgoing power

$$z = \frac{ln(\frac{I_0}{I})}{\alpha}. \tag{5.2}$$

For an SNR of 1, I was set to the noise floor of the detector, which in our case was 1 μW. An SNR of 2 (where there was at least some useful signal, albeit very noisy) was achieved by setting I to 2 μW. These two SNR values showed where the upper thickness limits for YSZ samples were for our system. Lastly, the thickness at which half of the incident power is transmitted was calculated by setting the fraction $\frac{I_0}{I}$ to 2. The outcomes of these calculations are shown in Figure 5.9. It can be seen that for half power transmission, the thickness of the YSZ sample had to be of the order of 200 μm.

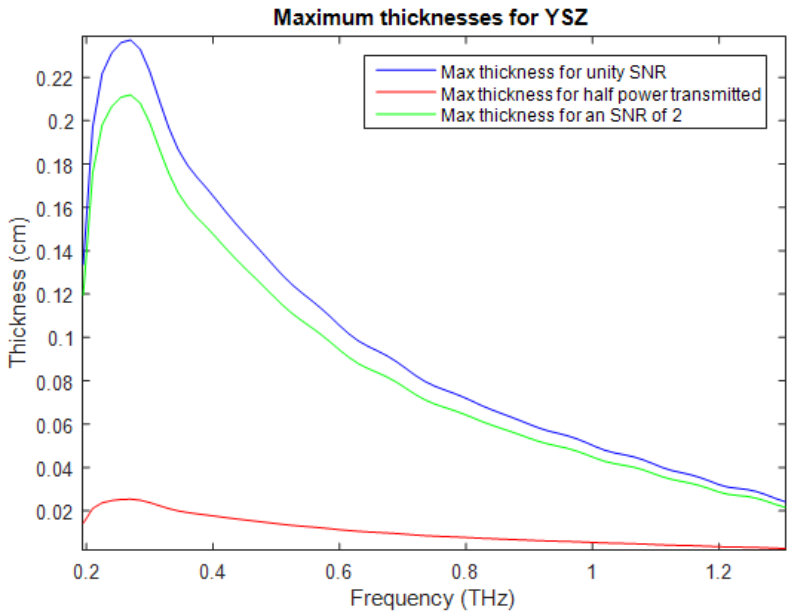

Figure 5.9: Maximal thicknesses for a YSZ sample in order to get measurable amounts of signal with the GHz system.

In the end a sample thickness of 600 μm thickness was chosen as a good compromise thickness for a set of sintered YTZP samples to be made which would be used for stress-optic measurements and which were also tested with TDS. A thickness for optimal tranmission would have been closer to 2 μm, but that would lead to samples which would break the moment any load was applied to them. The time domain traces, seen in Figure 5.10, showed a delay between reference and sample pulses of $\sim$10 ps compared to the

$\sim$5 ps for the YSZ disk, while the thickness was only $\frac{1}{3}$ larger for the YTZP samples. This implied a much higher refractive index, which was also corroborated by the data presented in [8], which showed an index of the order of 5.8 for a sintered bulk YSZ sample, which has minimal porosity. Dispersion was still clearly present and evident in both the broadening of the sample pulse with respect to the reference one and the fact that the second half of the pulse contained proportionally more energy than the first half with the sample in the beampath.

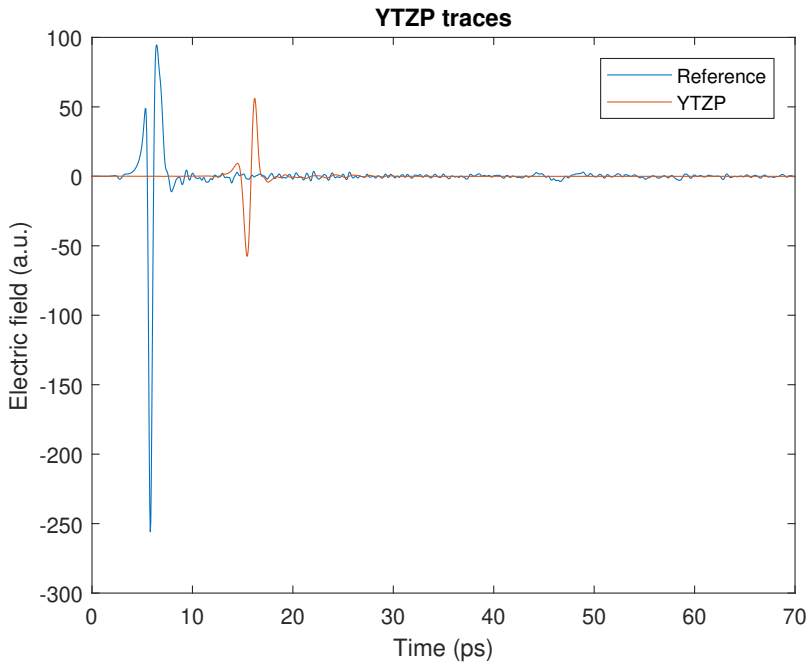

Figure 5.10: Reference (blue) and sample (orange) time domain traces for the YTZP sample.

The refractive index itself varied from close to 5.8 at 200 GHz up to 6.2 at 1.6 THz, which is almost twice as much variation as seen for the YSZ sample. The absorption, on the other hand, was found to be rising slightly less steeply. It still started around 50 cm^{-1}, but only rose to 200 cm^{-1} at 1.5 THz. Both refractive index and absorption are plotted in Figure 5.11. The difference in absorption could be caused by differences in yttria concentration within the YTZP compared to the YSZ sample. The YTZP samples were made with 8% in weight in yttria, while, as mentioned above, the YSZ sample has unknown composition.

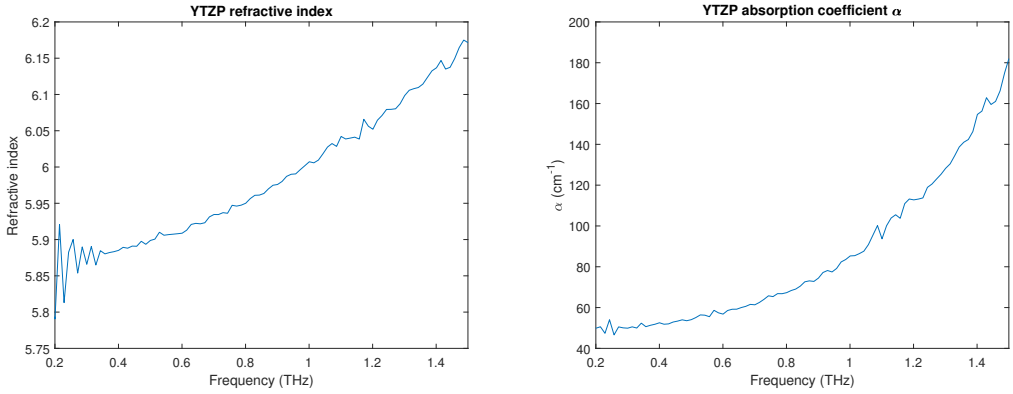

(a) (b)

Figure 5.11: Optical properties of YTZP measured with TDS. (a) Refractive index and (b) absorption coefficient α.

5.3.5 Al_2O_3 samples

Since thermal barrier coatings are attached to metallic substrates in general, they aren't usually suitable for transmission analysis. However, one possible bondcoat that is between the substrate and the YSZ layer is Al_2O_3, which also means that the coatings will bond to sapphire (αAl_2O_3). Sapphire is at least partially transparent at optical frequencies (dependent on purities) and similarly, it is at least partially transparent in the THz region. This was verified by testing a 3 mm thick sapphire disk followed by some measurements on sapphire disks with YSZ coatings deposited on them through electron beam physical vapour deposition (EB-PVD). Additionally, Al_2O_3 ceramic was tested on its own in order to get baseline values for the bondcoat which could be fed into any multilayer models in the future.

First, Al_2O_3 ceramic was be looked at. While the sample was fairly thick (2.7 mm), it exhibited reasonably low absorption and limited dispersion, as the sample trace is fairly close to a merely attenuated version of the reference trace without significant broadening or changes to the field distribution within the pulse.

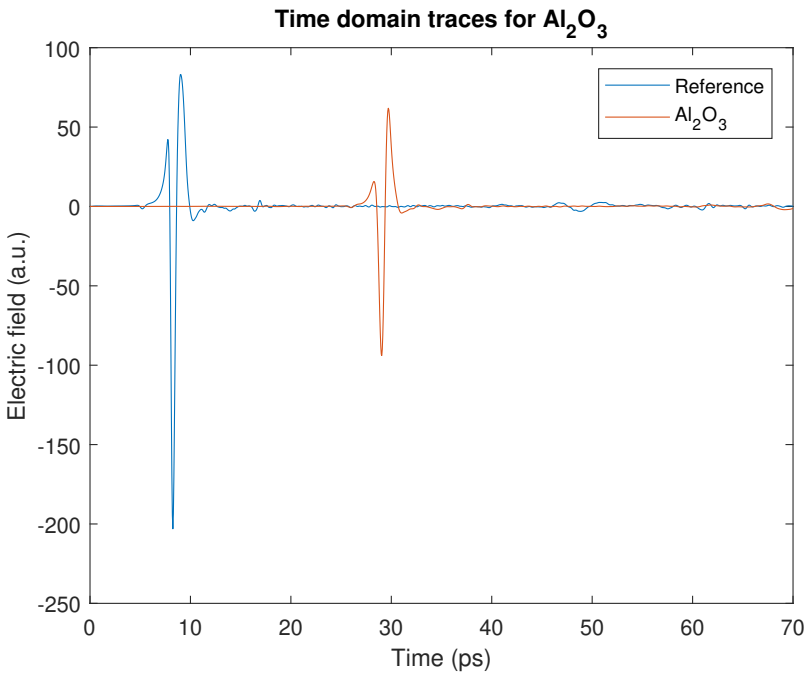

Figure 5.12: Reference (blue) and sample (orange) time domain traces for the Al_2O_3 ceramic sample.

Figure 5.13 below shows the refractive index and absorption for Al_2O_3 ceramic. There were only small variation in refractive index, it stayed between 3.29 and 3.32, which was a tenth of the range of change that could be seen for the YTZP in Figure 5.11a and over a larger bandwidth as well. The absorption coefficient itself was fairly negligible up to 1 THz after which it started to increase linearly by roughly 10 cm^{-1} over 0.5 THz. This explains why the transmitted signal in Figure 5.12 was fairly large, but why the bandwidth at the same time still reaches its limit around 2 THz.

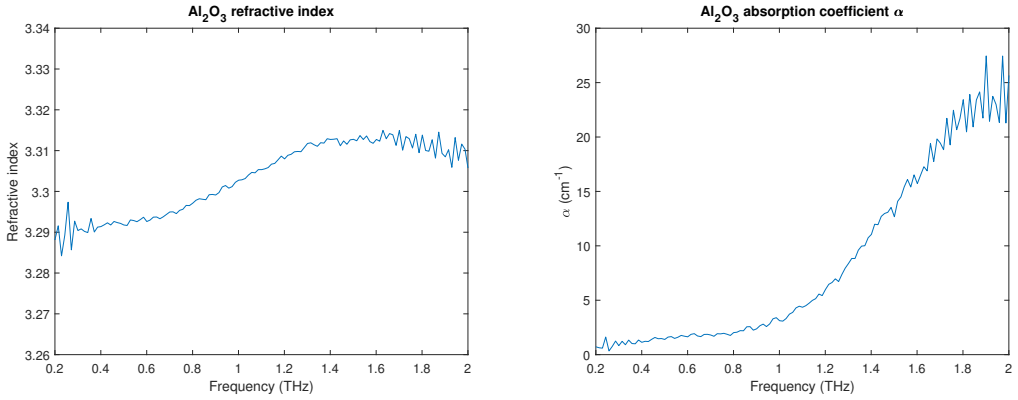

(a) (b)

Figure 5.13: Optical properties of Al_2O_3 ceramic measured with TDS. (a) Refractive index and (b) absorption coefficient α.

In order to assess whether sapphire would make a suitable transmission substrate for GHz and THz measurements, a sample of 3 mm thickness was tested. The cut direction of the samples that were provided for these measurements was not known. The fact that it showed birefringence,as can be seen in Figure 5.14 by the presence of 2 distinct pulses within the sample trace, suggested that the sapphire samples were cut along the R axis. In this case the system polarisation was aligned closer to the slow axis than the fast axis, as there is a small pulse that appears first, which is followed by the main pulse $\sim$3 ps later. While the birefringence of Sapphire is well documented in the literature, it was looked at in detail as practice with TDS before looking at strain-optic measuremnts. The sample was mounted in a rotation mount in order to find the axes and characterise each of them separately.

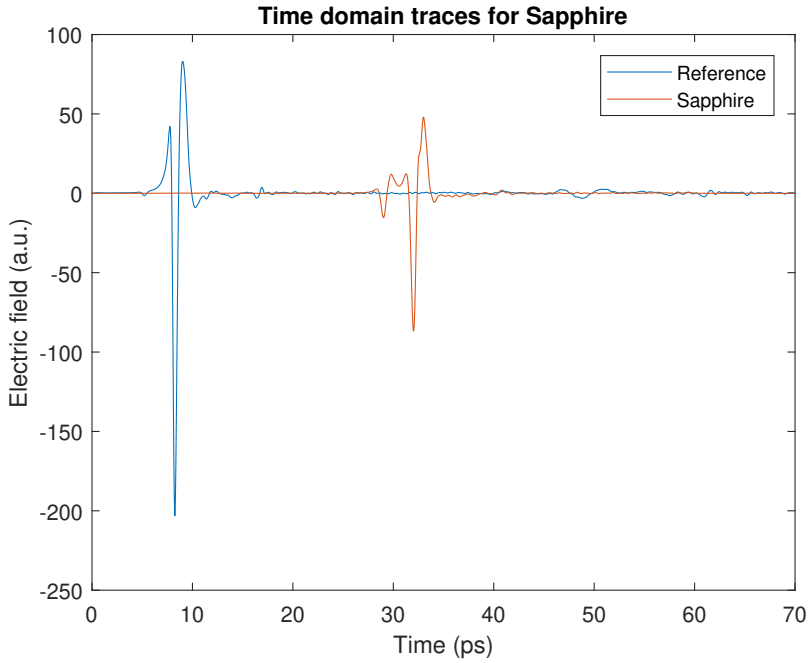

Figure 5.14: Reference (blue) and sample (orange) time domain traces for the sapphire sample.

The traces shown in Figure 5.15 show the polarisation aligned as far as possible with the fast and slow axes respectively. Aside from the lower refractive index, the absorption and dispersion properties between the axes was also different, which was highlighted by the difference in sample pulse shape for the two cases.

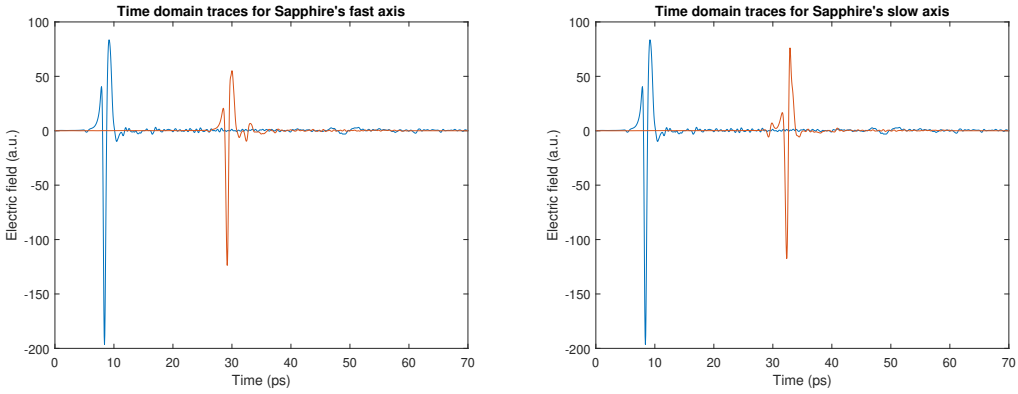

(a) (b)

Figure 5.15: Reference (blue) and sample (orange) time domain traces for the sapphire sample where (a) shows the signal along the fast axis and (b) along the slow axis.

The optical properties for the two axes are presented in Figure 5.16. One important point to note was the presence of discontinuities in the refractive index which was caused by atmospheric absorption lines. Taking aside the discontinuities, the refractive index of the slow axis was fairly close to that of the Al_2O_3 ceramic, and the same applies to the absorption. The main difference to the ceramic sample was that the divergence is stronger as seen by the lack of a plateau for the first THz for the refractive index. The fast axis on the other hand showed lower absorption for most of the bandwidth, with a linear increase only taking place after 2.5 THz. This also explained the difference in measurement bandwidth between the axis, as the slow axis showed its cut-off point around 3.5 THz, while the fast one only reached that point close to 4 THz. In terms of dispersion, it was likely a little less dispersive than the slow axis, but in order to make a firm statement on this, measurements without phase discontinuities due to absorption would be necessary.

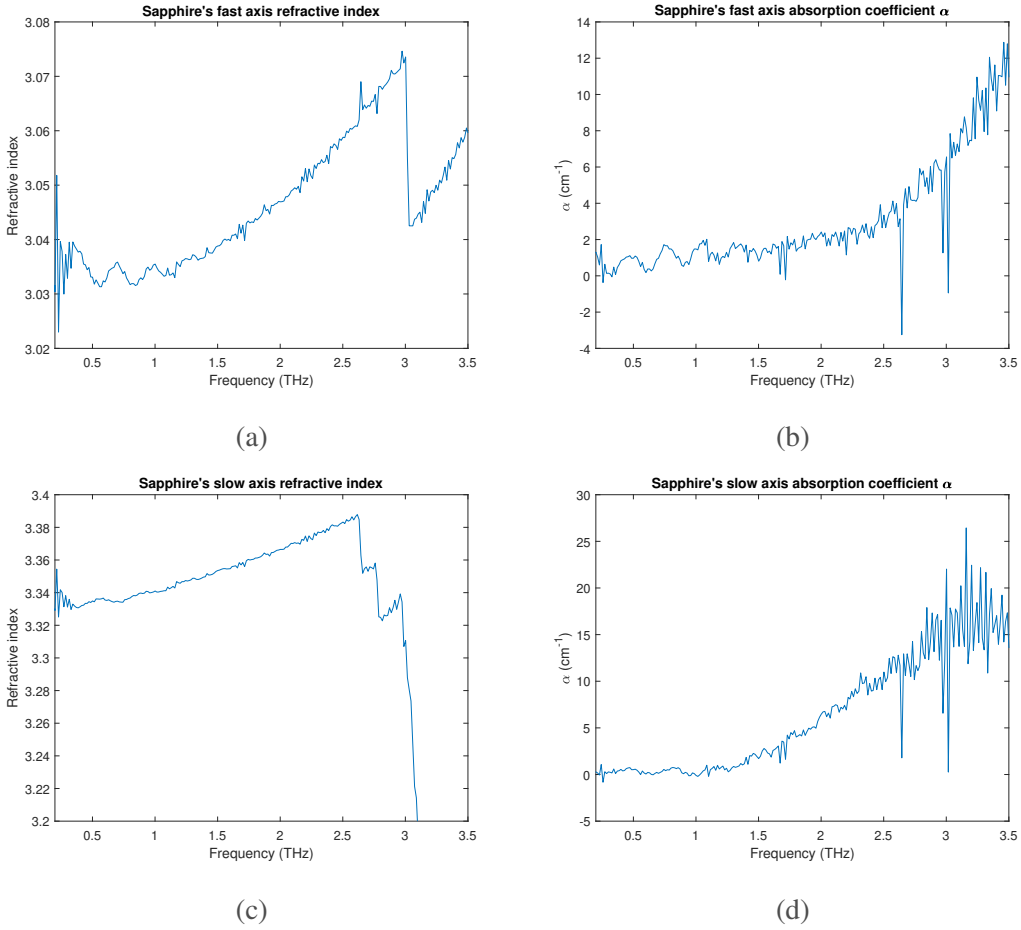

Figure 5.16: Optical properties of sapphire measured with TDS. (a) Refractive index and (b) absorption coefficient α for the fast axis. (c) Refractive index and (d) absorption coefficient α for the slow axis.

Following the initial tests on the sapphire substrate, 2 substrates coated with YSZ were looked at. These samples also showed birefringence, even though it was less obvious for the first sample (Figure 5.17a), where only a small second pulse could be made out within the tail of the first, it was much easier to notice on the second sample (Figure 5.17b), which had a fairly strong second pulse. This implied that the measurements on the first sample were taken close to one of the axes, while in case of the second they were taken somewhere in between them. Unfortunately this was not identified at the time, which meant that no further measurements to find the fast and slow axes were taken.

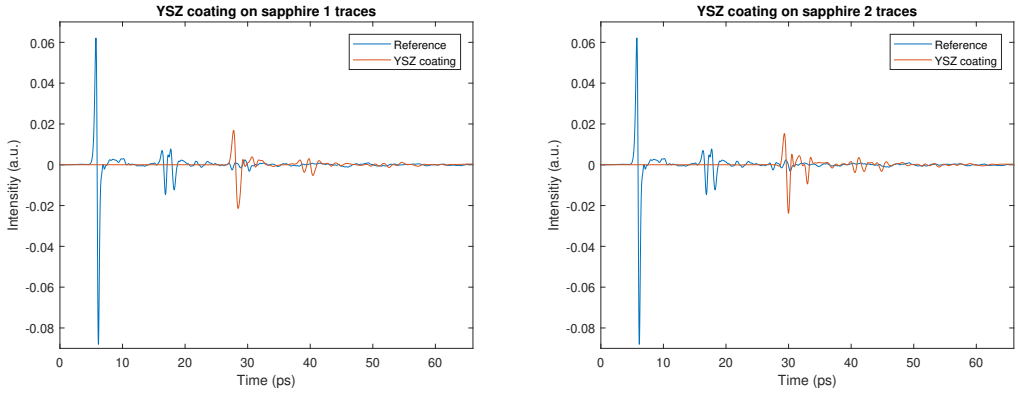

(a) (b)

Figure 5.17: Reference (blue) and sample (orange) time domain traces for the YSZ coated sapphire samples.

The refractive index values for both samples came out as roughly the same as that for the fast axis of the sapphire substrate, however the discontinuities at 1.18 THz for the first coating, Figure 5.18a, and at 1.52 THz for the second coating, Figure 5.18c, are caused by absorption peaks within the material rather than water vapour, as the samples were tested within a nitrogen atmosphere. The peaks are evident in Figures 5.18b and 5.18d respectively. Additionally, for the second coating, there was a regular fringe pattern in the absorption which was caused by the interaction of the slow and fast axes in the material as the measurement was taken between the two. It should be noted though that the material properties in Figure 5.18 were describing the coated sapphire as a whole, the properties of the coating itself could not be separated from the sapphire, merely compared to the sample without the coating present.

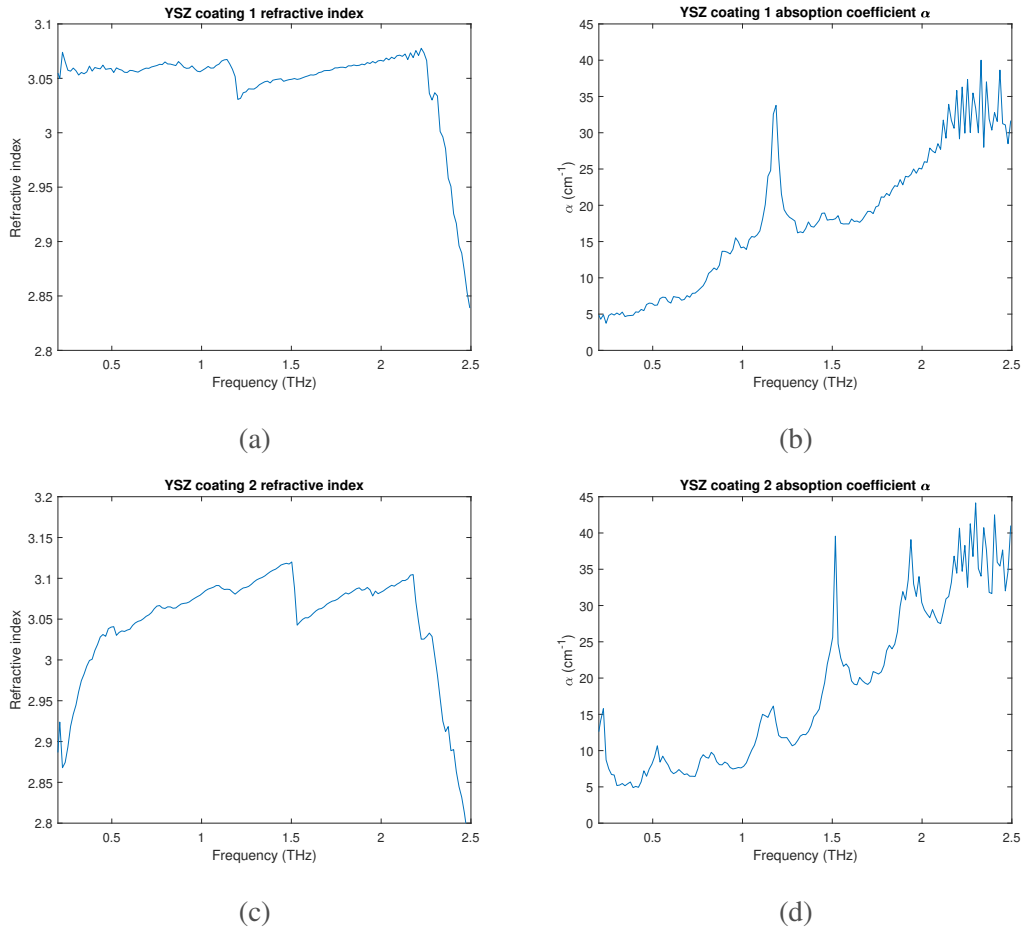

Figure 5.18: Optical properties of the YSZ coated sapphire samples measured with TDS. (a) Refractive index and (b) absorption coefficient α for the first sample. (c) Refractive index and (d) absorption coefficient α for the second sample.

Finally, Figures 5.17a and 5.17b, the ratio between the first peak of the reference signal and sample signal for the YSZ coated sapphire samples was be compared its equivalent for the sapphire substrate in Figure 5.14. The difference was roughly 50% with a thickness close to 200 μm for the YSZ coatings. This level of absorption was expected from the tests of the free standing YSZ sample, as shown by the curve for half power transmission in Figure 5.9, which also confirmed that the absorption properties of the coatings were reasonably in line with those of the samples tested in Section 5.3.4.

Throughout this section, the analysis of the optical parameters of several relevant materials for the work presented within this Thesis has been presented. The absorption of yttria stabilised zirconia (both YSZ and YTZP) was one of the most important results here, as that has been found to be reasonably consistent across samples with different porosities, and could thus be used as a fairly good starting point to model absorption throughout

a thermal barrier coating, while the refractive index values are highly dependent on porosity, making those values less useful for application to thermal barrier coatings, but they are still useful as a sanity check for the material properties obtained during the stress tests of the YTZP samples.

5.4 Tensile Measurements

5.4.1 Introduction

After the material characterisation presented in Section 5.3 was carried out, as well as the GHz tensile tests were finished (Sections 3.3 and 3.4), they were repeated with TDS in order to try corroborate the previous observations. The following Section will present the tensile tests both in transmission and reflection that were carried out using TDS.

5.4.2 Experimental set-up

This section will discuss 2 different set-ups, one for the transmission measurements and one for the reflection ones. In both cases a TeraFlash provided by Toptica Photonics was used and all measurements were taken in a nitrogen atmosphere to remove the water vapour lines as far as possible.

For the transmission measurements, a standard set-up like that shown in Figure 5.1 was used. The main differences were that the pump and probe arms were fiber-couple rather than free standing. Additionally, the sample was only partially covering the beam in order to be able to measure a reference and sample pulse on the same trace. This was necessary as a regular shift of the temporal position of the pulse peak was discovered in the system, where it moved back and forth over a range of 150 fs over a time of 30 minutes. Considering each tensile test took around an hour, it was going to see 2 cycles of peak movement which was an order of magnitude larger than the shifts caused by the stress-optic effects. As there was not enough regularity in the shifts to model and eliminate them, it was decided to take both sample and reference traces simultaneously. The most straightforward way to approach this was to only cover about 80% of the beam with the sample. The disadvantage of this approach was that absorption could not be charac-

terised, nor could frequency resolved information be extracted from the data without a pulse model which included dispersion broadening effects. However, since the parameter of interest for our measurements was the real part of the refractive index, this was deemed acceptable, as time-of-flight calculations could yield the average index for the material.

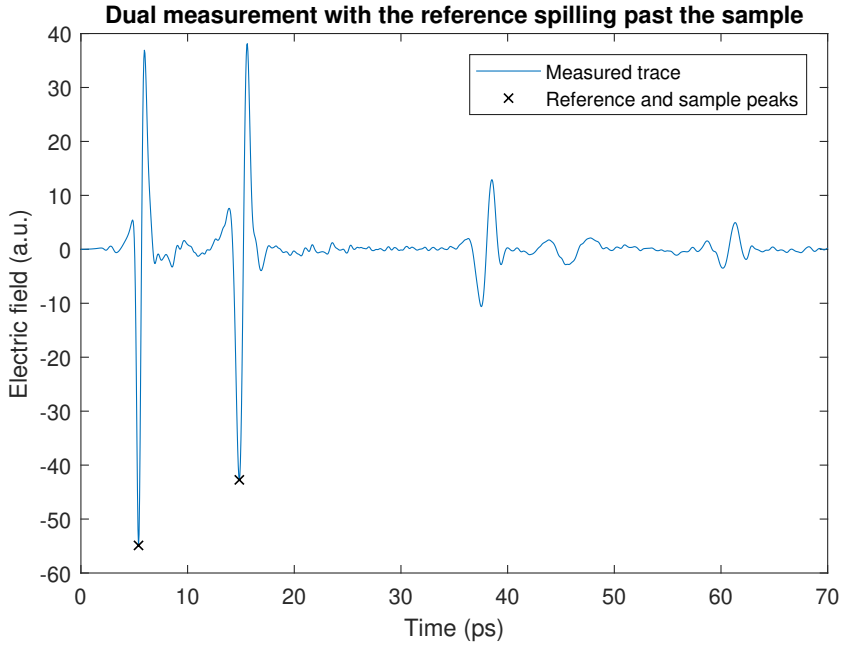

Figure 5.19: Reference and sample trace in one. The first peak is the reference spilling past the sample, which is followed by a second peak which travelled through the sample.

The reflection measurements were carried out with a pre-aligned reflection head into which the emmiter and recveiver antennas were fixed that was mounted on a translation stage. The head was moved in on the sample until the returned intensity from the reflection of the front surface was at its maximum, as at that point the sample surface was at the focus. Figure 5.20 shows a picture of the reflection head in position in front of a sample.

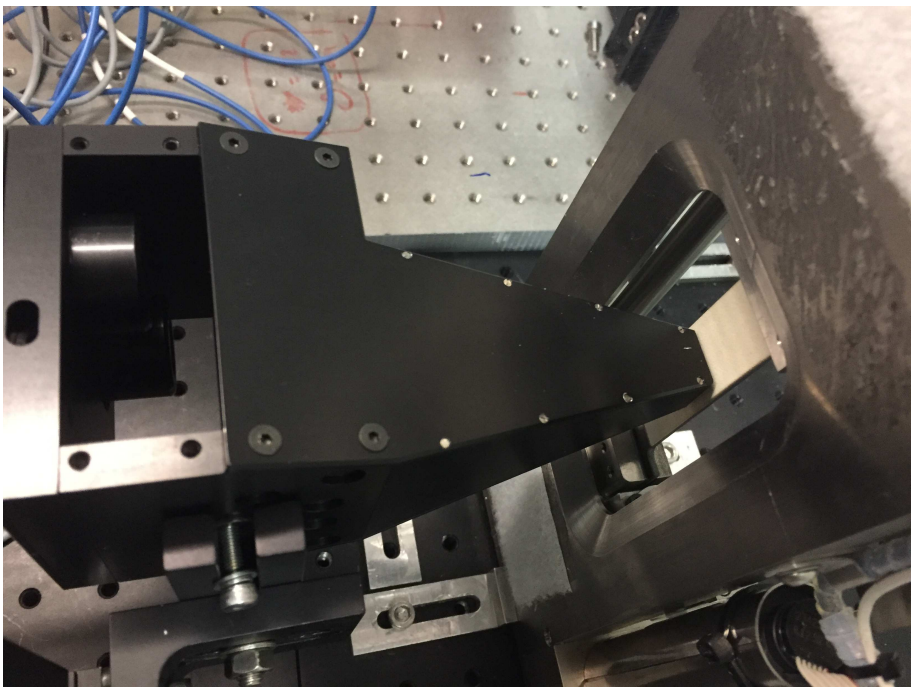

Figure 5.20: Picture of the reflection head in position. The two cylinders on the left are the antennas which are pointing onto a set of 4 off-axis parabolic mirrors focussing the signal on the sample surface.

The samples under test were 3 sintered YTZP samples, with a thickness of 583 μm for the first of them and 730 μm for the other two, as well as 4 samples of plasma sprayed (APS) YSZ coating on mild steel substrates and 3 samples of electron beam physical vapour deposited (EB-PVD) YSZ on FeCrAlloy substrates. The sintered ceramic samples were tested both in transmission and reflection while all the coatings were only tested in reflection due to their metallic substrates. Aside from thicknesses all sample dimensions were the same as they were designed for use with our tensometer (a DeBen 2kN dual leadscrew tensile testing stage).

The YTZP had a density of 6.02 g·cm^{-3}, an average crystal size of less than one micron, a Youngs modulus of 210 GPa and Poissons ratio of 0.3, values supplied by the manufacturer. The APS samples were divided into two sets, one with a 1 mm thick substrate and one with a 2 mm thick substrate. The coating thickness was at 380 μm for the thin substrates and 370 μm for the thick substrates. The EB-PVD samples all had substrates of 1.5 mm with coating thicknesses of 300 μm.

5.4.3 Measurement Procedure

The measurement procedure for both transmission and reflection measurements will be laid out at the same time below, as they are largely the same, while any differences will be pointed out as necessary.

Before any tensile tests were carried out, a reference trace was measured to assess the system alignment, which was followed by a background measurement with the beam fully blocked. This trace was subtracted of any subsequent traces in order to remove systematic errors caused by background signals within the lab. For the reflection measurements, a polished aluminium plate was used as reflector to generate a reference, while the beam was ”blocked” by simply removing the sample, leaving nothing for the beam to reflect off and get picked back up.

Once the background was characterised, the tensile stage’s load cell was balanced so that after clamping in it was at 0 N. The balancing is necessary as clamping the sample into the stage applies a small load (typically of the order of 3 N) to the sample, and by starting the measurements at 0, the absolute applied load during the experiments was measured, with the sample clamped in having been taken as the rest state.

For the transmission samples, the tensile stage was repositioned after each sample to ensure that the reference trace and sample trace had close to the same peak intensity, keeping the reference slightly more intense to simplify the location of the reference during the processing. In order to do that, the stage was fixed to the optical bench such that it could only move at a right angle to the beam, and once a suitable position was found, that axis was fixed as well so that there was no potential of it moving during the experiments.

As the reference pulse for the reflection measurements was the first reflection off the sample’s front surface, the reflection head only needed to be brought in towards the sample until its intensity was at a maximum for it to be properly aligned. Therefore the head was mounted on a translation stage which moved in at a right angle to and in the centre of the sample’s front face. The focus of the head was such that the measurements were non-contact measurements with the focus 2-3 mm from the end of the head to avoid it damaging the samples.

The analysis of the resultant traces was performed with a MATLAB®program that was written specifically for the task. After reading in and averaging the traces for any given load, it located the relevant peaks within the traces, super-resolved them by fitting a second order Gaussian bell to them and using their peak as a refined peak position in the time domain. This position was used to perform a time-of-flight calculation to yield the refractive index of the sample under the given load.

The first peak of the reference pulse as well as the first peak of the sample pulse were the ones used in the analysis. In order to locate the reference peak, the maximum of the trace's absolute value was taken, which is required as rotating the antenna by 180°will yield the same trace as before while inverting the sign. Thus to cover all options and increase the code's flexibility, the absolute value of the trace was used, while the sign of the peak was check by looking at the maximum's position on the raw trace. In order to locate the second pulse's peak, the local extrema within the trace were located.

For the transmission measurements as well as the reflection measurements on the coatings, the reference pulse and sample pulse both had the same sign, as both corresponded to a signal which experienced one reflection of a low-to-high index interface. This means that taking the local maximum (or minimum dependent on the reference pulse's direction) of the trace after the reference pulse yielded the correct peak to consider. In the case of the reflection measurements on the YTZP samples, the reflection off the back surface was inverted compared to the front surface, as the latter was caused by a low-to-high index interface, while the former originated at a high-to-low index interface, which doesn't cause a 180°phase shift in the reflected signal. The code was capable of locating higher order pulses by using the time difference between the reflections off the front surface and back surface and looking for the peaks with corresponding sign around the time where the next reflection was expected to take place. Those higher order reflection were not used in the calculations though as their intensities were generally fairly low and they were highly distored by dispersion, making the fits for the super-resolution less reliable on them. Figure 5.21 shows an example of the peak location and the time differences between the peaks in ps. The sample in that case was one of the EB-PVD coatings.

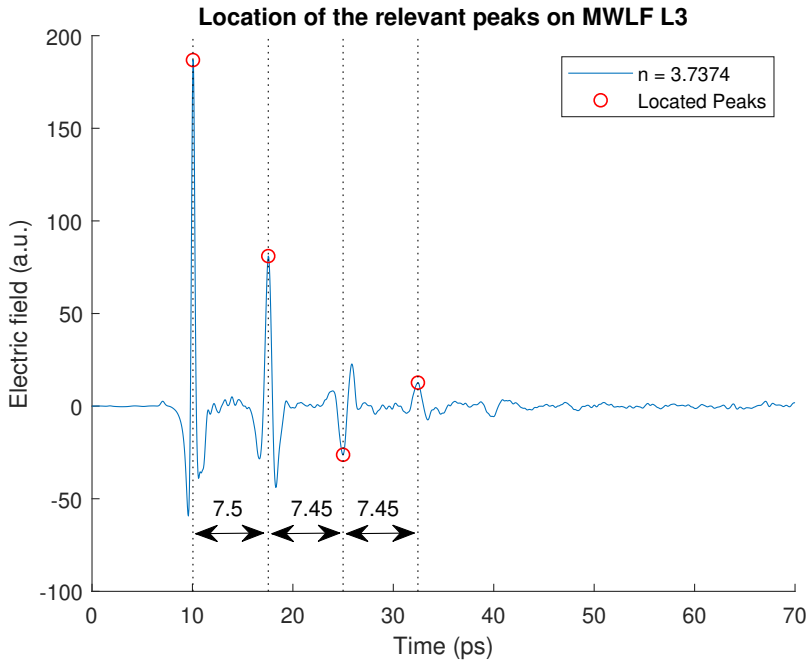

Figure 5.21: Example of the location of the relevant peaks for the analysis.

Once the relevant peaks were located, they were super-resolved in order to overcome the limits imposed by the system's repetition rate coupled with the delay voice coil's movement speed. This limit meant that the sample spacing was at 50 fs, while the measured shifts were up to 10 fs. While the exact shape of the optical pump pulse wasn't known, it is usually safe to try fit a Gaussian or Lorentzian to fs pulses and expect a reasonably close fit. The THz pulse generated from the pump pulse on the other hand can usually be modeled reasonably well by taking the first derivative of the input shape. This is due to the fact that the generated pulse depends on the rate of change of the induced electric field within the antenna, which in turn depends on the rate of change of the pump pulse's intensity. In this instance, both a second order Gaussian and Lorentzian were tested as fitting curves, and the fits were restricted to area around the peak only, with the Gaussian having been kept in the code as it was the better fit of the two. The fitted second order Gaussian can be written as

$$f(x) = a\,\frac{1\ -\ 2\,log2(x-b)^2}{c^2}\ \cdot\ e^{\frac{-2\,log2(x-b)^2}{c^2}}\ -\ d \tag{5.3}$$

where a, b, c and d are fitting parameters. a is a scaling factor, d is an offset in y, b is an offset in x and c is the pulse width. a and b were essentially free parameters, allowed

to vary from the trace minimum to its maximum for the former and from 0 to the length of the trace in ps for the latter.c was allowed to vary from 0.1 to 2 ps, which covered the range of widths seen for the first two pulses and d was fixed to zero as there was no DC offset in the data, so it wasn't allowed in the fits either.

Equation 5.3 was used to generate a fit to the data around the peaks of relevance on a time scale with $\sim$ 0.1 fs resolution, and the fitted value for b was used as the final peak location. With the peak positions known to a sufficient degree of accuracy, the refractive index was calculated from

$$n = \frac{c_0 \cdot \Delta t}{2d} \tag{5.4}$$

where c_0 is the speed of light, Δt is the time difference between reference and sample peaks and d is the sample thickness. At each load, 3 traces were recorded, where each recorded trace extracted from the measurement software of the TeraFlash was an average of 1000 traces recorded by the system. The resulting refractive index values were plotted against the applied strain, which, for the coatings, was calculated using the substrate cross-section and Young's modulus (210 GPa for mild steel and 198 GPa for FeCrAlloy), while the effect of the coating was assumed negligible. The slope of the resultant plot yielded the strain-optic coefficient for the given measurement. The thicknesses for the samples were obtained through micrometer measurements by taking the difference of the substrate thickness, which was exposed at the edge, and the coated sample's thickness measured at the centre where the beam was aimed to.

The following three Sections present the results for the YTZP samples in both transmission and reflection as well as the results of the 2 sets of coated samples.

5.4.4 YTZP Ceramic

In order to be able to compare the TDS results to the GHz measurements, the samples were loaded over the same ranges of values as the corresponding GHz measurements presented in Sections 3.3.4 and 3.4.4. In each case, each sample was tested 3 times. For the transmission measurements, that meant that the samples were loaded from 0 N to

350 N in steps of 25 N, while for the reflection measurements the loads ranged from 0 N to 650 N with a spacing of 50 N. Figure 5.22 shows the results for the YTZP samples in transmission (Figures 5.22a and 5.22c) and reflection (Figures 5.22b and 5.22d). While the scale on Figures 5.22a does wash it out a bit, the transmission results are noisier than the reflection ones, which is in large parts caused by the measurement approach. It should also be noted that the refractive index for the transmission case was significantly lower as for the reflection case. The index in the reflection measurements matches up with the expected values from the measurements presented in Section 5.3. This difference can be explained by a combination of diffraction effects and interference effects with the sample edge in the form of plasmonic interactions, which will slow down the part of the beam spilling past the sample.

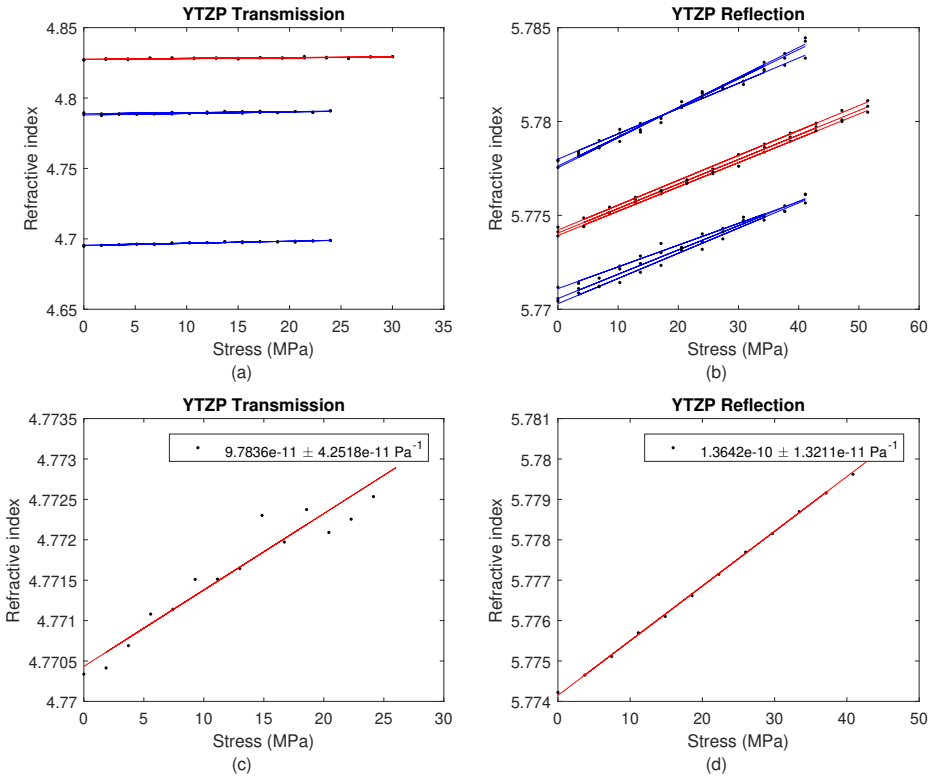

Figure 5.22: Results for the YTZP sample measurements. (a) and (b) contain the results for every run of all 3 samples for transmission and reflection respectively, while (c) and (d) contain an averaged trace and the corresponding strain-optic coefficient for transmission and reflection respectively. For the plots in (a) and (b), the red lines correspond to the thinner sample and the blue lines are the measurements for the thicker samples.

The results in Figure 5.22 were plotted against stress in order to be able to compare

them to the GHz ones, with stress-optic coefficients measured as $9.8\times10^{-2} \pm 4.3\times10^{-2}$ GPa^{-1} and $1.4\times10^{-1} \pm 1.3\times10^{-2}$ GPa^{-1} for the transmission and reflection cases respectively. Since the coatings were assessed in terms of strain rather than stress though, the strain-optic coefficients were calculated as well for these measurements and found to be 2.1×10^{-5} $\pm$ 9.0×10^{-6} and $2.9\times10^{-5} \pm 2.8\times10^{-6}$ respectively. Comparing the TDS values to the GHz ones, it was found that for the transmission case, the value was clearly lower for the TDS case, but the GHz value was within the error, which was about 43%. The reflection value matched up a lot better, with a difference of about 8×10^{-3} GPa^{-1} and errors of 1.3×10^{-2} GPa^{-1} and 1.6×10^{-2} GPa^{-1} for the TDS and GHz values respectively.

Since good agreement between the YTZP measurements for the GHz and TDS measurements was observed, the measurement procedure and analysis approaches were accepted as working as intended, allowing the coatings to be measured next.

APS Coatings on Mild Steel Substrate

The APS coatings shown in Figure 3.29 and with GHz results presented in Section 3.4.4 were tested again with the TDS system. All measurements were taken in the centre of the sample in order to avoid any potential edge effects. While a *x*,*y* surface scan of the sample was considered as a possibility, the idea was left for the future as we were more interested in doing an assessment of the material/coating system parameters. The following Figure 5.23 shows the results for the APS samples on 2 mm thick substrate (Figures 5.23a and 5.23c) and the results for the APS samples on 1 mm thick substrate (Figures 5.23b and 5.23d).

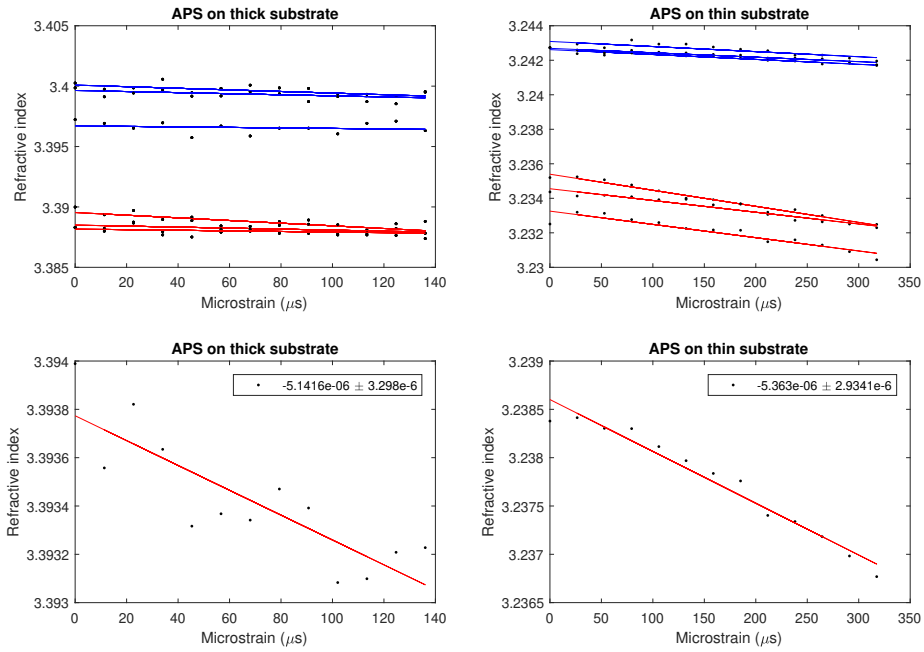

Figure 5.23: Results for the APS samples on mild steel substrates measurements. (a) and (b) contain the results for the different runs for the thick and thin substrates respectively, while (c) and (d) contain an averaged trace and the corresponding strain-optic coefficient for the thick and thin substrates respectively. For the plots in (a) and (b), the red lines correspond to one sample and the blue lines are the measurements for the other samples.

The APS samples showed significant amounts of noise compared the the YTZP samples, with the values reaching 64% for the thick samples and 55% for the thin samples. The strain-optic coefficients themselves were found to be very low when compared to the refitted GHz values with -5.1$\times10^{-6}$ $\pm$ 3.3$\times10^{-6}$ and -5.4$\times10^{-6}$ $\pm$ 2.9$\times10^{-6}$ for the thick and thin samples respectively. In comparison, the GHz values were of the order of 2.5$\times10^{-5}$, which is 5 times larger. This difference was partially attributed to the difference in frequency range and also tied to the fact that the samples in questions had been stressed quite a few times followed by about 2 years of lying in storage in the lab, which may have affected the internal structure to the point of changing the reactions to being pulled again. It was noted though that the slopes were still negative, which means that there is a strain related change within the material which can't be attributed to a change in cross-section with strain. The reason the thickness change couldn't cause a negative slope is that refractive index measurements actually measure the product of the index and the thickness, with the two being separated afterwards based on additional measurements

or by solving with known thickness. If the thickness decreases (as it does if a sample is pulled), the refractive index has to increase to keep the product constant, thus if the thickness is kept constant in the analysis, the refractive index will show a small positive slope. The negative slope for these samples was attributed to changes in sample porosity as they were pulled, as the material making up most of the coating has a clearly positive strain-optic coefficient.

5.4.5 EB-PVD Coatings on FeCrAlloy Substrate

In order to expand on what was done with the GHz system rather than merely repeat the same measurements on the same samples, 3 EB-PVD YSZ coatings on FeCrAlloy substrates manufactured at Cranfield University were pulled. These measurements were the first quantitative measurements performed on EB-PVD coatings, which up to this point had only been assessed qualitatively in our lab. The substrates were cut to the same dogbone shape as all other tensile samples used throughout the project and coated with a 300 μm layer of YZS. They were loaded from 0 N up to 1200 N in 150 N steps, and following the TDS measurements, the curvature on the back of the samples was measured with a confocal microscope and combined with digital image correlation to estimate the amount of straightening for each load. This approach to correct for bending strains is explained in Section 3.4.5. The results for the sample measurements are shown in Figure 5.24.

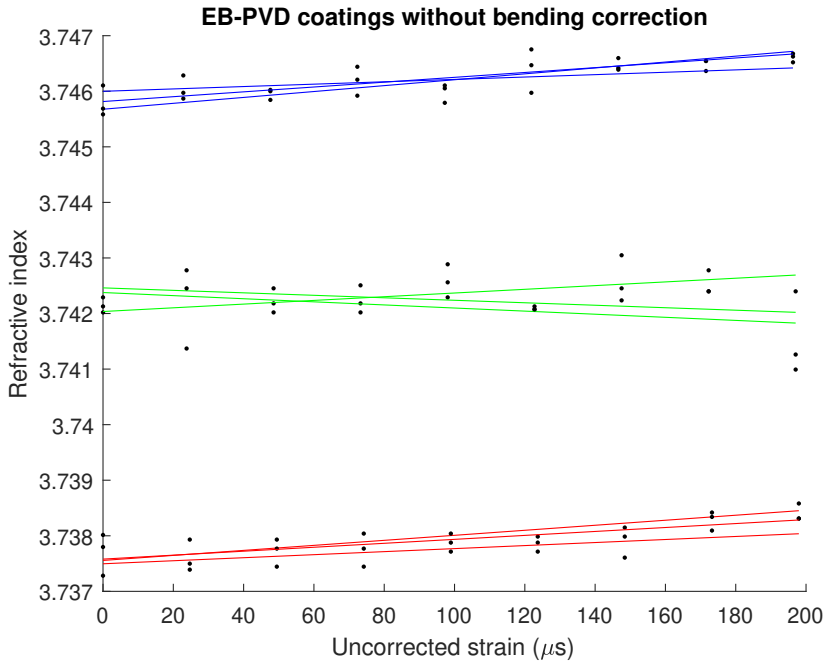

Figure 5.24: Results for the EB-PVD samples on mild steel substrates measurements. (a) shows the measured refractive indexes without bending correction while (b) includes a bending correction based on the initial curvature and DIC measurements. It is important to note that the data with the green fits has had an offset of -0.24 in refractive index applied to it in order to be able to make out detail on the figure, as otherwise the large scale would have washed out any the variations in slopes and the data.

The results for the EB-PVD samples were a lot noisier still than those for the APS coatings, with average slopes of $0.5\times10^{-6} \pm 1.3\times10^{-6}$. The noise levels here are at least twice the mean value, compared to $\sim$60% for the APS coatings. Part of the reason for the large noise level is that the 2 of the runs for one of the samples came out with negative slopes, while all other runs had positive slopes. The noise on it could be improved by only looking at the 2 samples that had positive slopes, leading to a slope of $3.7\times10^{-6} \pm 1.2\times10^{-6}$, which is a 31.5% error, and thus a lot more acceptable, but it would also simply disregard one whole set of measurements. Additionally, if assuming that the effects of thickness changes was similar to that of YTZP (shown on Figure 3.26), the thickness variation expected from the applied strain was of the same order of magnitude than that expected from the typical total change in refractive index measured for the different runs, which suggested that in fact the measurements were all within the noise of the thickness measurements and variations. Thus it couldn't be concluded that there was a clearly defined strain-optic reaction within these coatings.

Additionally, the effects of the bending correction for these samples were found to be erratic on one hand and fairly negligible on the other. The difference between corrected and uncorrected strain-optic coefficients was of the order of 1×10^{-7}, which was negligible in comparison to the noise. Furthermore, for the EB-PVD samples, the calculated strains without any corrections added were a much better match to the measured strains than those with corrections. One possible explanation for this, as well as the lack of a clear response to applied strain for the coating system, was the coating structure. Figure 5.25 shows a scanning electron microscope (SEM) image of the cross section of an EB-PVD sample taken at Cranfield University. That image highlights the columnar structure of those coatings, which weren't bonded together, but merely sitting next to each other (albeit with some degree of compression). What that meant was that the columns could move around, pushing past one another, which was a mechanism through which it might have been able to dissipate both bending and tensile strains, so that the net measurable effects ended up minimal and hardly distinguishable from noise.

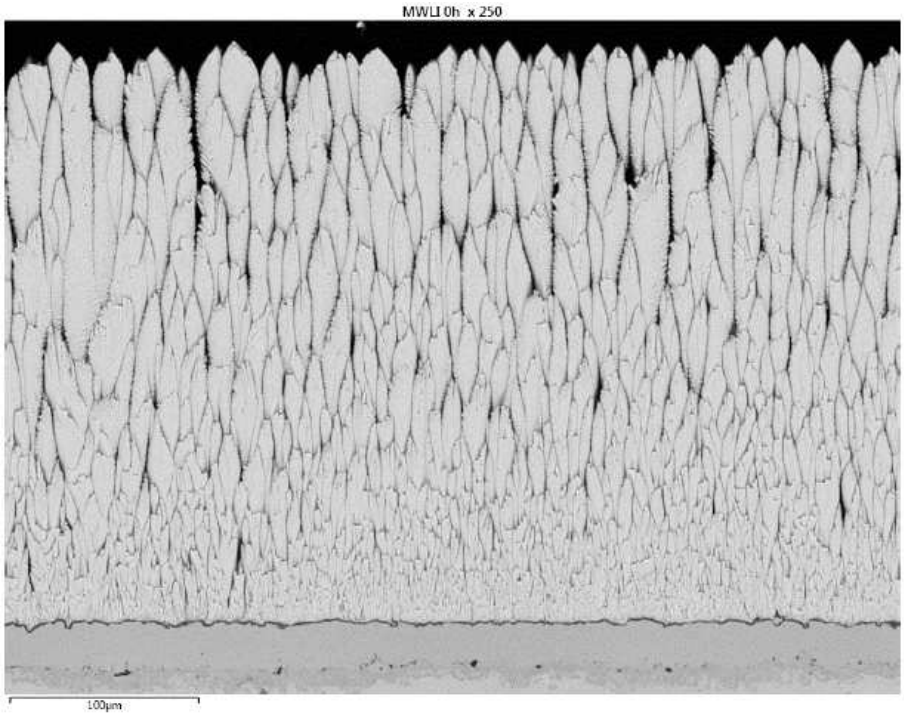

Figure 5.25: Cross-section of EB-PVD coating taken with an SEM by C.Chalk at Cranfield University.

In this section, the application of time-domain spectroscopy to measure the strain-optic response of sintered YTZP as well as YSZ coatings on mild steel and FeCrAlloy coatings were presented. The experiments on the YTZP samples were used corroborate

previous strain-optic measurements performed within the GHz range. The results for the TDS were a good match to the GHz values for the bulk specimens, which implied that in both cases the technique is appropriate. The measurements for the coatings on mild steel were again compared to previous data in the GHz range. In this instance, there were significant discrepancies in terms of refractive index and thickness values between the two, which led to a re-evaluation of the GHz fitting process for coatings on metal substrates. The strain-optic coefficients between the methods differed significantly, however, it there was a good chance that that was caused by plastic changes within the samples from their continuous pulling combined with a year spent lying in storage before the TDS measurements were carried out.

Finally, first measurements on EB-PVD samples were carried out. The measurements did not suggest any clearly defined strain-optic response for those samples, as the measured changes were fairly low and could be almost entirely attributed to reductions in thickness with applied load. This was reinforced by the fact that there was significant variations between the results for different runs of the same sample. Additionally, the coating structure facilitated stress relief for the coating, making strain measurements inaccurate if not even very hard to feasibly pull off. It should be kept in mind though that this was a first and fairly small set of samples that were tested, so that they might not adequately represent YSZ EB-PVD coatings on FeCrAlloy substrates as a whole, especially since the specifics of the manufacturing process, the thermal history and inter-columnar space will have a significant impact on any strain-optic measurements.

5.5 Conclusions

In this chapter, measurements using time-domain spectroscopy (TDS) have been presented. A set of initial experiments was used both for material characterisation purposes, checking that our samples' properties matched up with those reported in the literature, and to get get familiarised with the technique and the corresponding data analysis. PTFE was a good candidate for the second as it has an extremely flat frequency response and is routinely used for THz optics, thus is quite well characterised over the typical frequency ranges of a TDS system. YTZP samples were compared to published work and the measured complex refractive was a close match to the published values and could be used as

a standard for a coating with no porosity (which is unrealistic, as the porosity is necessary for the relief of thermal stresses caused by the mismatches of the thermal expansion coefficients of the YSZ topcoat and the nickel superalloy that forms the substrate).

Following these experiments, the strain-optic coefficient measurements performed in Chapter 3 with GHz radiation were repeated. Good agreement between the reflection measurements for both techniques on the YTZP samples was observed, while the transmission results with TDS were somewhat more erratic due to the way they needed to be performed. However, the GHz values for transmission were still within the error margin of the TDS values (but not vice versa). It was deemed unnecessary to dwell on the transmission results too much as they were originally a means to get to the reflection measurements as they were easier to implement in the GHz system. As the aims of the project are the measurement of coatings on metallic substrates, only reflection measurements will be possible anyways.

The air-plasma sprayed samples presented in Chapter 3 as well as in [70] were tested again using TDS, which led to a much better understanding of the coating's response to applied strains. A few points about those measurements and their implications should be noted here. First, the TDS results for refractive index and thickness (which was based on a micrometer measurement of the thickness) were very different to those in the publication. This observation led to the Fresnel fitting to be revisited and refined, as previously the fits yielded unnaturally large values for the thickness and correspondingly low values for the refractive index. Secondly, the fact that the refractive index response to applied strain was negative, as opposed to the positive response of the bulk material, was explained through the presence of the porosity. This argument was based on the knowledge that thermal barrier coatings are porous coatings by design, which also explained why the refractive index of any tested coating was always significantly lower than that of the bulk YTZP. If the porous coating had a strain applied to it, then around the pores, which are mechanical weak points, that strain would lead to an expansion of the pore through an elastic or plastic (e.g. microcracking) deformation. As the pores expand, the air/coating ratio would increase leading to a decreased refractive index. This strongly reinforced the previous opinion that the strain response was dependent on manufacture and thermal history by attaching a mechanism for the coating response to it. Furthermore, the strain-optic coefficient measured with TDS was found to be 5 times smaller than that measured in

the GHz experiments. While there could be differences caused by the differing frequency content, they shouldn't be that large. It was more likely that this difference was caused by plastic deformations within the samples caused during the GHz experiments followed by ageing effects as the coatings spent over a year in storage before the TDS experiments were carried out.

Finally, first strain-optic measurements for EB-PVD coatings were presented within this chapter. These measurements showed that for this coating structure the actual strain response was very hard to characterise. This was assumed to be a by-product of the structure as the coatings consist of columns of YSZ which are fixed at the bottom to the bondcoat, but otherwise free-standing, even though the tops are in compression due to the columns around them. There is however a lot of room for their upper parts to shift around which gives them a way of strain relief. The fact that the strain-optic coefficient values obtained for these samples were an order of magnitude smaller than those for the APS coatings, and their sign wasn't consistent reinforced the idea that the coating was relieving applied strains within its structure, while the measured changes were of a size where they could be attributed to noise caused by small thickness variations. Another factor reinforcing this idea was that that the strains released by changes in curvature seemed to be absorbed within the coating and weren't measureable on the back of the substrate, where the strains measured with digital image correlation corresponded to those calculated by dividing the applied load by substrate's cross-sectional area, even though clear levels of straightening, which should add to the strain from the applied load, were measured.

Chapter 6

Conclusions

Following a clear lack of quantitative non-destructive testing methods using the high level of transmission of thermal barrier coatings at THz frequencies, a number of experiments moving towards such a technique were presented in this thesis. These included the first measure of the direct stress-optic coefficient for YTZP samples both in transmission and reflection at GHz frequencies, with values of $1.3\times10^{-1} \pm 0.8\times10^{-2}$ GPa^{-1} and $1.3\times10^{-1} \pm 1.6\times10^{-2}$ GPa^{-1} for transmission and reflection respectively. Additionally these measurements were also performed with time-domain spectroscopy, which for YSZ samples typically had bandwidths up to 2 THz, though the nature of the coatings meant that analysis was performed in the time-domain, foregoing frequency resolved results for the time being. The transmission results are seen as inaccurate due to the requirement to have the sample and reference in the same trace, which was fulfilled by having parts of the beam spill past the sample. The values obtained with TDS were 9.8×10^{-2} $\pm 4.3\times10^{-2}$ GPa^{-1} and $1.4\times10^{-1} \pm 1.3\times10^{-2}$ GPa^{-1} for the transmission and reflection cases respectively.

The transmission measurements were extended to 2D stress imaging with a confocal set-up with the GHz system with limited success. The system performance in terms of resolution was adequate for the long wavelength and optics that were designed for 500 GHz radiation rather than the used 330 GHz, with a lateral resolution of 0.315 $lp\cdot$ mm^{-1}, and a axial resolution close to 32.5 mm. The axial resolution was at a level where 3D imaging was not feasibile, however with higher frequency systems this may become possible for the thermal barrier coatings with typical thicknesses around 300 μm. The reason for the limited success of the stress imaging experiments could in large part be explained by insufficiently controlled sample thickness. The variations across the spot

size of $\sim$3 mm were enough to cause the Fresnel response over the scanned frequency range to contain superposition of a range of thicknesses, which made a fit based on a single thickness tenous at best, and more likely simply unsuitable. The technique itself shows promise though for the measurements with well behaved samples, and an increase in spatial resolution and the linked reduction in spot size should drastically improve the performance.

Since results for the bulk ceramic sample showed a clear stress-optic response, the measurement technique was applied to YSZ coatings on metal substrates. The first set of such samples were ones where the coating was applied through APS. Two different substrate thicknesses with the same coating thickness for each were tested, and their responses were found to be slightly different in the GHz measurements. The thin samples had a linear response across the whole range of applied strains with a strain-optic coefficient of (-2.5 $\pm$ 0.7) $\times$ $10^{-5}\mu s^{-1}$, while the thick samples had an initial linear region with a very comparable value of (-2.5 $\pm$ 1.0) $\times$ $10^{-5}\mu s^{-1}$, which then transitioned into a second region where the noise in the data was at almost 200%. The negative refractive index was explained through changes in porosity due to the applied load, where the pores opened up due to elastic or plastic (e.g. microcracking) deformation. The second region could be a point where either the pores stopped expanding much and the ceramic itself started bearing larger and larger fractions of the strains, or more significant cracking happened across the coating outwidth the measurement spot in the centre, leading to stress relieve and reductions in strain at the centre. It is also worth noting here that the values for the strain-optic coefficient quoted here were obtained after the fitting model for the coated samples was refined to model the metallic substrate and bring the refracrtive index and thickness values in line with those expected from alternative measurements.

The TDS measurements on the APS coatings yielded much lower values for the strain-optic coefficient, and the clear split into 2 distinct regions for the thicker samples was found to be absent. These differences were attributed to plastic changes in the coatings caused by the previous experiments with the GHz system followed by over a year in storage. This also highlighted how dynamic the coating systems are, casting serious doubt on the suitability and feasibility of a fully quantitative analysis approach.

This sentiment was reinforced by measurements on EB-PVD coatings, where the apparent lack of a quantifiable strain-optic response was seen. The coating structure itself

gave some insight as to why that was the case, as the YSZ columns grown on the bondcoat are only fixed at the bondcoat interface and otherwise can move around provided the externally applied strains overcome the compression caused by adjacent columns. Thus measuring a strain-optic response for these coatings may not be possible from the start as the structure allows the coating to relieve transverse strains across the coating by having the YSZ columns shift around.

This suggested that absolute strain measurements are unliekly to be fruitful, and the emphasis should rahter be put on local changes within a coated system which could identify a high-strain region caused by a defect.

6.1 Future Work

There are a few areas where there was clear scope for future work and improvement. The first of these was the confocal imaging system. The system should be revisited with a fresh set of samples with polished sufraces to remove local thickness variations. Additionally, the illumination should be provided by a higher frequency source (moving up to 1 THz would already bring a $3\times$ improvement in resolution limit) with optics optimised for the chosen frequency. This would allows performance to be pushed closed to the diffraction limit for the input wavelength. Finally, it would likely be worthwhile for it to be suitable for reflection measurements if it is to be used as part of the Manufacturing with Light project (or any follow-up from it), since all the measurements are based around coatings on metallic substrates. The measurement speeds, which are an issue with the frequency scanning approach, can be increased by shifting from single pixel detectors to line or array detectors as they become available with suitable pixel sizes and sensitivities.

The second area of future work is within the TDS measurements. The time-of-flight measurements as they were applied yield the group index for the material for the bandwidth of the THz pulse. There is clear value in obtaining frequency resolved information on the coating systems for better characterisation of their responses and potential improvement of the measurement noise on the phase measruements. This does require the separation of the sample and reference signals, which is not currently done as there was partial pulse overlap which caused issues with simple windowing. The way forward here is a pulse model which can be used to fit the reference and sample traces and which

accounts for dispersion in the tested sample. Alternatively (or additionally), further improvements to the current peak fitting can also be made by measuring the shape of the optical input pulse and applying a double differential to it to obtain an even closer match to the THz pulse, as the current model fits the peak closely, but doesn't follow the whole pulse shape too well. This second issue is related to dispersion in the generation medium (the GaAs antenna or the ZnTe crystal) which would have to be accounted after the double differential of the input pulse to fully model the generated THz pulse.

Finally, in order to achieve the Manufacturing with Light project's overall goal of assessing thermal barrier coating lifetimes from a post-manufacture measurement of the coating system, it will likely be necessary to step back from a fully quantitative measurement to a qualitative assessment of local variations across a coated specimen. In first instance the mechanisms by which the different coating types respond to strains need to be investigated further and their impact on optically measurable parameters of the coating assessed. Especially the effect of the columnar structure of EB-PVD coatings needs to be understood in order to extract meaningful measurements from those coating systems. Futhermore, the dielectric models for the coatings should be refined by characterising the complex reftactive index of the substrates used throughout the project. The inclusion of surface roughness at each interface as well as the bond coat and thermally grown oxyde layers are further improvements that can be made to the models, but that were considered beyond the scope of the work performed within this thesis.

Bibliography

[1] N. P. Padture, "Thermal barrier coatings for gas-turbine engine applications," *Science*, vol. 296, no. 5566, pp. 280–284, 2002.

[2] D. R. Clarke, M. Oechsner, and N. P. Padture, "Thermal-barrier coatings for more efficient gas-turbine engines," *MRS Bulletin*, vol. 37, no. 10, pp. 891–898, 2012.

[3] R. Darolia, "Thermal barrier coatings technology: critical review, progress update, remaining challenges and prospects," *International Materials Reviews*, vol. 58, no. 6, pp. 315–348, 2013.

[4] C. G. Levi, J. W. Hutchinson, M.-H. Vidal-Stif, and C. A. Johnson, "Environmental degradation of thermal-barrier coatings by molten deposits," *MRS Bulletin*, vol. 37, no. 10, pp. 932–941, 2012.

[5] K. Schlichting, N. Padture, E. Jordan, and M. Gell, "Failure modes in plasma-sprayed thermal barrier coatings," *Materials Science and Engineering: A*, vol. 342, no. 1, pp. 120–130, 2003.

[6] A. Rabiei, "Failure mechanisms associated with the thermally grown oxide in plasma-sprayed thermal barrier coatings," *Acta Materialia*, vol. 48, no. 15, pp. 3963–3976, 2000.

[7] A. N. Khan, J. Lu, and H. Liao, "Effect of residual stresses on air plasma sprayed thermal barrier coatings," *Surface and Coatings Technology*, vol. 168, no. 2, pp. 291 – 299, 2003.

[8] M. Watanabe, S. Kuroda, H. Yamawaki, and M. Shiwa, "Terahertz dielectric properties of plasma-sprayed thermal-barrier coatings," *Surface and Coatings Technology*, vol. 205, no. 19, pp. 4620–4626, 2011.

[9] L. Li, W. Song, Z. Wang, S. Wang, M. He, J. Han, and L. Cong, "Active modulation of refractive index by stress in the terahertz frequency range," *Applied Optics*, vol. 52, no. 25, p. 6364, 2013.

[10] W. Song, L. Li, Z. Wang, S. Wang, M. He, J. Han, L. Cong, and Y. Deng, "Experimental verification of the uniaxial stress-optic law in the terahertz frequency regime," *Optics and Lasers in Engineering*, vol. 52, pp. 174–177, 2014.

[11] I. Mehdi, "THz local oscillator technology," *Proc.SPIE*, vol. 5498, 2004.

[12] J. Ward, E. Schlecht, G. Chattopadhyay, A. Maestrini, J. Gill, F. Maiwald, H. Javadi, and I. Mehdi, "Capability of THz sources based on schottky diode frequency multiplier chains," pp. 1587–1590, IEEE, 2004.

[13] H. Liu, C. Viegas, J. Powell, H. Sanghera, A. Whimster, H. Wang, W. He, C. Donaldson, P. G. Huggard, and B. Alderman, "A high-power schottky diode frequency multiplier chain at 360 GHz for gyro-TWA applications," pp. 1–2, IEEE, 2017.

[14] R. M. Cerda, "Frequency multiplication techniques." http://www.crystek.com/documents/appnotes/Frequency_Multiplication_Techniques.pdf, 2013. Accessed: 2018-06-12.

[15] T. W. Crowe, R. Zimmermann, and R. Zimmermann, "Consideration of velocity saturation in the design of GaAs varactor diodes," *IEEE Microwave and Guided Wave Letters*, vol. 3, no. 6, p. 3, 1993.

[16] E. Kolberg, T. Tolmunen, M. Frerking, and J. East, "Current saturation in submillimeter-wave varactors," *IEEE Transactions on Microwave Theory and Techniques*, vol. 40, no. 5, pp. 831–838, 1995.

[17] J. Louhi and A. Raisanen, "On the modeling and optimization of schottky varactor frequency multipliers at submillimeter wavelengths," *IEEE Transactions on Microwave Theory and Techniques*, vol. 43, no. 4, pp. 922–926, 1995.

[18] A. Maestrini, B. Thomas, H. Wang, C. Jung, J. Treuttel, Y. Jin, G. Chattopadhyay, I. Mehdi, and G. Beaudin, "Schottky diode-based terahertz frequency multipliers and mixers," *Comptes Rendus Physique*, vol. 11, no. 7, pp. 480–495, 2010.

[19] P. Antognetti and G. Massobrio, *Semiconductor Device Modeling with Spice*. New York, NY, USA: McGraw-Hill, Inc., 2nd ed., 1993.

[20] Hamamatsu Solid State Division, "Characteristics and use of infrared detectors." https://www.hamamatsu.com/resources/pdf/ssd/infrared_techinfo_e.pdf, 2011. Accessed: 2014-10-28.

[21] D. Dooley, "Sensitivity of broadband pyroelectric terahertz detectors continues to improve," *Laser Focus World*, vol. 46, no. 5, p. 49, 2010.

[22] A. Odon, "Modelling and simulation of the pyroelectric detector using MATLAB/simulink," *Measurement Science Review*, vol. 10, no. 6, 2010.

[23] M. Naftaly and R. A. Dudley, "Calibration of terahertz spectrometers," in *The International Society for Optical Engineering*, vol. 8195, p. 8195N, 2010.

[24] V. Stenger, M. Shnider, S. Sriram, D. Dooley, and M. Stout, "Thin film lithium tantalate (tflt) pyroelectric detectors," vol. 8261, pp. 8261 – 8261 – 9, 2012.

[25] W. Li, J. Wang, J. Gou, Z. Huang, and Y. Jiang, "Fabrication and characterization of linear terahertz detector arrays based on lithium tantalate crystal," *Journal of Infrared, Millimeter, and Terahertz Waves*, vol. 36, no. 1, pp. 42–48, 2015.

[26] Ophir Photonics, "Pyroelectric array camera." http://www.ophiropt.com/laser-measurement-instruments/beam-profilers/products/industrial-applications/the-cameras/pyrocam, 2015. Accessed: 2015-05-04.

[27] D. H. Auston and K. P. Cheung, "Coherent time-domain far-infrared spectroscopy," *JOSA B*, vol. 2, no. 4, pp. 606–612, 1985.

[28] M. van Exter, C. Fattinger, and D. Grischkowsky, "Highbrightness terahertz beams characterized with an ultrafast detector," *Applied Physics Letters*, vol. 55, no. 4, pp. 337–339, 1989.

[29] D. Grischkowsky, S. Keiding, M. Van Exter, and C. Fattinger, "Far-infrared time-domain spectroscopy with terahertz beams of dielectrics and semiconductors," *Journal of the Optical Society of America B*, vol. 7, no. 10, pp. 2006–2015, 1990.

[30] A. Y. Pawar, D. D. Sonawane, K. B. Erande, and D. V. Derle, "Terahertz technology and its applications," *Drug Invention Today*, vol. 5, no. 2, pp. 157–163, 2013.

[31] W. Withayachumnankul and M. Naftaly, "Fundamentals of measurement in terahertz time-domain spectroscopy," *Journal of Infrared, Millimeter, and Terahertz Waves*, vol. 35, no. 8, pp. 610–637, 2014.

[32] M. Tani, S. Matsuura, K. Sakai, and S.-i. Nakashima, "Emission characteristics of photoconductive antennas based on low-temperature-grown GaAs and semi-insulating GaAs," *Applied Optics*, vol. 36, no. 30, pp. 7853–7859, 1997.

[33] Q. Chang and D. Yang, "Broadband THz generation from photoconductive antenna," *PIERS Online*, vol. 1, no. 3, pp. 331–335, 2005.

[34] J. Zhang, Y. Hong, S. Braunstein, and K. Shore, "Terahertz pulse generation and detection with LT-GaAs photoconductive antenna," *IEE Proceedings - Optoelectronics*, vol. 151, no. 2, p. 98, 2004.

[35] N. Katzenellenbogen and D. Grischkowsky, "Efficient generation of 380 fs pulses of THz radiation by ultrafast laser pulse excitation of a biased metalsemiconductor interface," *Applied Physics Letters*, vol. 58, no. 3, pp. 222–224, 1991.

[36] H. Harde and D. Grischkowsky, "Coherent transients excited by subpicosecond pulses of terahertz radiation," *Journal of the Optical Society of America B*, vol. 8, no. 8, p. 1642, 1991.

[37] A. C. Warren, N. Katzenellenbogen, D. Grischkowsky, J. M. Woodall, M. R. Melloch, and N. Otsuka, "Subpicosecond, freely propagating electromagnetic pulse generation and detection using GaAs:as epilayers," *Applied Physics Letters*, vol. 58, no. 14, pp. 1512–1514, 1991.

[38] L. Hou and W. Shi, "Intense terahertz radiation from μm-gap GaAs photoconductive antenna," *Journal of Physics: Conference Series*, vol. 276, p. 012208, 2011.

[39] W. Shi, H. Xue, X. Ma, and Z. Zhang, "Intense terahertz radiation from GaAs photoconductive antenna array," *Session 5A1 Optics and Photonics 2*, p. 797, 2009.

[40] M. Suzuki and M. Tonouchi, "Fe-implanted InGaAs terahertz emitters for 1.56μm wavelength excitation," *Applied Physics Letters*, vol. 86, no. 5, p. 051104, 2005.

[41] B. Sartorius, H. Roehle, H. Knzel, J. Bttcher, M. Schlak, D. Stanze, H. Venghaus, and M. Schell, "All-fiber terahertz time-domain spectrometer operating at 1.5 μm telecom wavelengths," *Optics Express*, vol. 16, no. 13, p. 9565, 2008.

[42] C. D. Wood, O. Hatem, J. E. Cunningham, E. H. Linfield, A. G. Davies, P. J. Cannard, M. J. Robertson, and D. G. Moodie, "Terahertz emission from metal-organic

chemical vapor deposition grown fe:InGaAs using 830 nm to 1.55 μm excitation," *Applied Physics Letters*, vol. 96, no. 19, p. 194104, 2010.

[43] H. Roehle, R. J. B. Dietz, H. J. Hensel, J. Bttcher, H. Knzel, D. Stanze, M. Schell, and B. Sartorius, "Next generation 15 μm terahertz antennas: mesa-structuring of InGaAs/InAlAs photoconductive layers," *Optics Express*, vol. 18, no. 3, p. 2296, 2010.

[44] R. J. B. Dietz, M. Gerhard, D. Stanze, M. Koch, B. Sartorius, and M. Schell, "THz generation at 155 μm excitation: six-fold increase in THz conversion efficiency by separated photoconductive and trapping regions," *Optics Express*, vol. 19, no. 27, p. 25911, 2011.

[45] A. Schwagmann, Z.-Y. Zhao, F. Ospald, H. Lu, D. C. Driscoll, M. P. Hanson, A. C. Gossard, and J. H. Smet, "Terahertz emission characteristics of ErAs:InGaAs-based photoconductive antennas excited at 1.55 μm," *Applied Physics Letters*, vol. 96, no. 14, p. 141108, 2010.

[46] X. Mu, Y. J. Ding, and I. B. Zotova, "Exploring fundamental limits to terahertz generation in electrooptic materials: From bulk to nanolayers," *Laser Physics*, vol. 18, no. 5, pp. 530–546, 2008.

[47] G. Gallot and D. Grischkowsky, "Electro-optic detection of terahertz radiation," *Journal of the Optical Society of America B*, vol. 16, no. 8, p. 1204, 1999.

[48] M. Naftaly, "Metrology issues and solutions in THz time-domain spectroscopy: Noise, errors, calibration," *IEEE Sensors Journal*, vol. 13, no. 1, pp. 8–17, 2013.

[49] M. Scheller, "Data extraction from terahertz time domain spectroscopy measurements," *Journal of Infrared, Millimeter, and Terahertz Waves*, vol. 35, no. 8, pp. 638–648, 2012.

[50] T. D. Dorney, R. G. Baraniuk, and D. M. Mittleman, "Material parameter estimation with terahertz time-domain spectroscopy," *Journal of the Optical Society of America A*, vol. 18, no. 7, p. 1562, 2001.

[51] O. Sushko, R. Dubrovka, and R. S. Donnan, "Analysis of optical thickness determination of materials by THz-TDS," *Journal of Physics: Conference Series*, vol. 472, p. 012005, 2013.

[52] M. Naftaly, "An international intercomparison of THz time-domain spectrometers," pp. 1–2, IEEE, 2016.

[53] W. Withayachumnankul, B. M. Fischer, H. Lin, and D. Abbott, "Uncertainty in terahertz time-domain spectroscopy measurement," *Journal of the Optical Society of America B*, vol. 25, no. 6, p. 1059, 2008.

[54] L. Fu, K. A. Khor, H. W. Ng, and T. N. Teo, "Non-destructive evaluation of plasma sprayed functionally graded thermal barrier coatings," *Surface and Coatings Technology*, vol. 130, no. 2, pp. 233 – 239, 2000.

[55] X. Q. Ma, S. Cho, and M. Takemoto, "Acoustic emission source analysis of plasma sprayed thermal barrier coatings during four-point bend tests," *Surface and Coatings Technology*, vol. 139, no. 1, pp. 55 – 62, 2001.

[56] L. Yang, Y. C. Zhou, W. G. Mao, and C. Lu, "Real-time acoustic emission testing based on wavelet transform for the failure process of thermal barrier coatings," *Applied Physics Letters*, vol. 93, no. 23, p. 231906, 2008.

[57] R. Vaen, Y. Kagawa, R. Subramanian, P. Zombo, and D. Zhu, "Testing and evaluation of thermal-barrier coatings," *MRS Bulletin*, vol. 37, no. 10, pp. 911–916, 2012.

[58] R. J. L. Steenbakker, J. P. Feist, R. G. Wellman, and J. R. Nicholls, "Sensor thermal barrier coatings: Remote in situ condition monitoring of EB-PVD coatings at elevated temperatures," *Journal of Engineering for Gas Turbines and Power*, vol. 131, no. 4, pp. 041301–041301–9, 2009.

[59] X. Wang, A. Atkinson, L. Chiriv, and J. R. Nicholls, "Evolution of stress and morphology in thermal barrier coatings," *Surface and Coatings Technology*, vol. 204, no. 23, pp. 3851 – 3857, 2010.

[60] W. A. Ellingson, C. M. Deemer, J. Sun, and E. R. Koehl, "NDE technology for ceramic composites," no. 42371, pp. 285–293, 2006.

[61] D. Zhu and R. A. Miller, "Sintering and creep behavior of plasma-sprayed zirconia- and hafnia-based thermal barrier coatings," *Surface and Coatings Technology*, vol. 108-109, pp. 114 – 120, 1998.

[62] V. Teixeira, M. Andritschky, W. Fischer, H. P. Buchkremer, and D. Stver, "Analysis of residual stresses in thermal barrier coatings," *Journal of Materials Processing Technology*, vol. 92-93, pp. 209 – 216, 1999.

[63] B. Rog, A. Fahr, J. S. R. Gigure, and K. I. McRae, "Nondestructive measurement of porosity in thermal barrier coatings," *Journal of Thermal Spray Technology*, vol. 12, no. 4, pp. 530–535, 2003.

[64] K. Ogawa, D. Minkov, T. Shoji, M. Sato, and H. Hashimoto, "NDE of degradation of thermal barrier coating by means of impedance spectroscopy," *NDT & E International*, vol. 32, no. 3, pp. 177 – 185, 1999.

[65] T. Fukuchi, N. Fuse, T. Fujii, M. Okada, K. Fukunaga, and M. Mizuno, "Measurement of topcoat thickness of thermal barrier coating for gas turbines using terahertz waves," *Electrical Engineering in Japan*, vol. 183, no. 4, pp. 1–9, 2013.

[66] J. White, G. Fichter, A. Chernovsky, J. F. Whitaker, D. Das, T. M. Pollock, D. Zimdars, D. O. Thompson, and D. E. Chimenti, "Time domain terahertz non-destructive evaluation of aeroturbine blade thermal barrier coatings," pp. 434–439, AIP, 2009.

[67] C.-C. Chen, D.-J. Lee, T. Pollock, and J. F. Whitaker, "Pulsed-terahertz reflectometry for health monitoring of ceramic thermal barrier coatings," *Optics Express*, vol. 18, no. 4, p. 3477, 2010.

[68] K. Ramesh, *Digital Photoelasticity: Advanced Techniques and Applications*. Springer Publishing Company, Incorporated, 1st ed., 2000.

[69] P. Schemmel, G. Diederich, and A. J. Moore, "Direct stress optic coefficients for YTZP ceramic and PTFE at GHz frequencies," *Optics Express*, vol. 24, no. 8, pp. 8110–8119, 2016.

[70] P. Schemmel, G. Diederich, and A. J. Moore, "Measurement of direct strain optic coefficient of YSZ thermal barrier coatings at GHz frequencies," *Optics Express*, vol. 25, no. 17, pp. 19968–19980, 2017.

[71] J. Lodenquai, "Determination of absorption coefficients of thin films," *Solar Energy*, vol. 53, no. 2, pp. 209 – 210, 1994.

[72] E. Hecht, *Optics (4th Edition)*. Addison Wesley, 4 ed., 2001.

[73] L. S., "Confocal laser scanning photoelasticity: Improvement of precision for quantitative photoelastic studies on model composite materials," *Scanning*, vol. 23, no. 4, pp. 273–278, 2001.

[74] M. Wijerathne, K. Oguni, and M. Hori, "Tensor field tomography based on 3d photoelasticity," *Mechanics of Materials*, vol. 34, no. 9, pp. 533 – 545, 2002.

[75] M. Wijerathne, K. Oguni, and M. Hori, "Stress field tomography based on 3d photoelasticity," *Journal of the Mechanics and Physics of Solids*, vol. 56, no. 3, pp. 1065 – 1085, 2008.

[76] R. D. Mindlin, "A mathematical theory of photoviscoelasticity," *Journal of Applied Physics*, vol. 20, no. 2, pp. 206–216, 1949.

[77] T. Hirano, Y. Imai, and Y. Hayashi, "Photovisco-elasto-plastic analysis tested on polyester by the scattered-light method," *Experimental Mechanics*, vol. 37, no. 2, pp. 159–164, 1997.

[78] R. B. Pipes and J. L. Rose, "Strain-optic law for a certain class of birefringent composites," *Experimental Mechanics*, vol. 14, no. 9, pp. 355–360, 1974.

[79] N. F. Borrelli and R. A. Miller, "Determination of the individual strain-optic coefficients of glass by an ultrasonic technique," *Appl. Opt.*, vol. 7, no. 5, pp. 745–750, 1968.

[80] L. Hua, Y. Song, J. Huang, X. Lan, Y. Li, and H. Xiao, "Microwave interrogated large core fused silica fiber michelson interferometer for strain sensing," *Appl. Opt.*, vol. 54, no. 24, pp. 7181–7187, 2015.

[81] S. E. A. Bayoumi and E. K. Frankl, "Fundamental relations in photoplasticity," *British Journal of Applied Physics*, vol. 4, no. 10, p. 306, 1953.

[82] A. P. Boresi and R. J. Schmidt, *Advanced Mechanics of Materials, 6th Edition*. Wiley, 6 ed., 2002.

[83] A. A. Mudassar and S. Butt, "Improved digital image correlation method," *Optics and Lasers in Engineering*, vol. 87, pp. 156–167, 2016.

[84] R. H. Webb, "Confocal optical microscopy," *Reports on Progess in Physics*, vol. 59, pp. 427–471, 1996.

[85] M. Naftaly and R. Dudley, “Orientational dependence of THz optical constants, birefrigence and dichroism of liquid crystals BL037 and GT3-23001,” *Optical Materials Express*, vol. 3, no. 4, pp. 459–465, 2013.